

Three-Dimensional Eddy Current Pulsed Thermography and Its Applications

A doctoral thesis submitted for the degree of Doctor of Philosophy

Xiaotian Chen, BSc



Intelligent, Sensing and Communications Research Group (ISC)

School of Engineering, Newcastle University

November 2021

CERTIFICATE OF ORIGINALITY

This is to certify that all the works submitted in this thesis are my own works except as specified in acknowledgments. Neither the work nor the thesis has been submitted to any other institution for another degree. I am responsible for all the works in this thesis.

..... (Signed)

..... (Candidate)

ABSTRACT

The measurement and quantification of defects is a challenge for Non-Destructive-Testing and Evaluation (NDT&E). Such challenges include the precise localisation and detection of surface and sub-surface defects, as well as the quantification of such defects. This work first reports a three-dimensional (3D) Eddy Current Pulsed Thermography (ECPT) system via integration with an RGB-D camera. Then, various quantitative measurements and analyses of defects are carried out based on the 3D ECPT system.

The ECPT system at Newcastle University has been proven to be an effective non-destructive testing (NDT) method in surface and sub-surface detection over the past few years. Based on the different numerical or analytical models, it has achieved precise defect detection on the rail tracks, wind turbines, carbon fibre reinforced plastic (CFRP) and so on. The ECPT system has the advantage of fast inspection and a large lift-off range. However, it involves a trade-off between detectable defect size and inspection area compared with other NDT methods. In addition, there are challenges of defect detection in a complex structure. Thus, the quantification of defects gives a higher requirement of the measurement the object geometry information. Furthermore, the analysis of thermal diffusion requires a precise 3D model. For this reason, a 3D ECPT system is proposed that adds each heat pixel with an exact X-Y-Z coordinate.

In this work, first, the 3D ECPT system is built. A feature-based automatic calibration of the infrared camera and the RGB-D camera is proposed. Second, the software platform is built. A fast 3D visualization is completed with multi-threading technology and the Point Cloud Library. Lastly, various studies of defect localization, quantification and thermal tomography reconstruction are carried out

Acknowledgment

First, I must thank my supervisor, Prof. Guiyun Tian, for taking me on as a PhD student in engineering after my undergraduate study. His vast experience in the area and his willingness to impart his knowledge have helped me greatly during my three years of research.

I would also like to thank my colleagues Dr. Kongjing Li, Dr. Chaoqing Tang, Dr. Aobo Zhao, Dr. Junzhen Zhu, Dr. Qiuji Yi and all other group members who helped me with discussions and supports. It would have been impossible to conduct this research without their help.

Finally, I would like to thank my family, my father who gave me encouragement and discussions and my mum who gave me support and accompanied with me during the writing stage of the PhD study.

Contents

ABSTRACT.....	I
List of publications:	X
1 INTRODUCTION.....	1
1.1 Background	1
1.2 Motivations.....	2
1.3 Aim and objectives.....	3
1.3.1 First theme: building the 3D ECPT system	3
1.3.2 Three dimensional visualization, multi-modality imaging fusion and defect detection5	
1.3.3 Three dimensional thermal imaging and analysis: 3D defect localization and quantification and thermal point cloud defect enhancement.	6
1.3.4 Tomographic reconstruction of the 3D ECPT.	7
1.4 Novelties and contributions of the work	8
2 LITERATURE REVIEW	9
2.1 Thermography and application of NDE	9
2.1.1 State of the art of thermography	9
2.1.2 Heat transfer.....	10
2.1.3 Thermography of NDE	11
2.2 3D reconstruction and image registration	17
2.2.1 Review of 3D scanning techniques.....	17
2.2.2 Kinect and David 3D scanners.....	18
2.3 Feature extraction and quantification of ECPT	21
2.3.1 Analytical study and physical comprehension for ECPT	23

2.3.2	Numerical study of ECPT	24
2.3.3	Relevant work on IR thermography-based NDT and challenges	25
2.4	Three dimensional capture and 3D temperature mapping	27
2.5	Summary and problems identified	28
3	DESIGN AND DEVELOPMENT OF 3D ECPT.....	30
3.1	Design and development of 3D ECPT system and camera registration	31
3.1.1	State-of-the-art of camera registration algorithms	34
3.1.2	Proposed feature-based IR-RGB-D camera registration algorithm	36
3.2	Kinect fusion and David 3D scanning.....	49
3.2.1	Kinect SL ranger and its features for fusion	49
3.2.2	David 3D systems and their features for fusion.....	53
3.2.3	Experimental set-up and samples.....	54
3.3	3D Visualization of thermal point cloud flow and fusion.....	55
3.3.1	The three-dimensional visualization software platform	55
3.3.2	Crack localization, sizing and thermal visible fusion	58
3.4	Summary	61
4	DEFECT DETECTION AND VALIDATION USING THE 3D ECPT SYSTEM AND VALIDATION.....	62
4.1	Segmentation of thermal point cloud data of rail track using PCA	62
4.2	Skewness features	66
4.2.1	Thermal transient response in ECPT	66
4.2.2	Skewness features for the characterization of defect depths and validation.....	70
4.2.3	Statistical analysis of the transient thermal response.....	72
4.2.4	Skewness feature versus depth.....	76
4.2.5	Skewness feature with different stages of ECPT (heating and cooling stage) .	82

4.2.6	Skewness feature on nature cracks	87
4.3	Thermal 3D gradient features and augmented reality for 3D visualization	91
4.3.1	The 3D thermal gradient feature	91
4.3.2	Magnetic field and thermal point cloud fusion	93
4.4	Summary	95
5	THERMAL TOMOGRAPHIC RECONSTRUCTION FOR 3D EDDY CURRENT PULSED THERMOGRAPHY	97
5.1	Introduction	97
5.2	Thermal behaviours of 3D ECPT, time-spatial image and DTSTD signal	99
5.3	Thermographic signal reconstruction on ECPT's thermal tomography	112
5.4	Comparison and summary	118
6	CONCLUSION AND FUTURE WORK	122
6.1	Conclusion and major contributions	122
6.1.1	Three-dimensional ECPT system set-up and camera registration	122
6.1.2	Three-dimensional scanning and visualization	123
6.1.3	Defect detection and validation using 3D ECPT system	124
6.1.4	Thermal tomography reconstruction of natural and artificial cracks using 3D ECPT	124
6.2	Future work	125
6.2.1	Directional emissivity correction	125
6.2.2	Defect depth estimation based on the analysis of 3D heat flow	125
6.2.3	Thermal tomographic reconstruction	126
Reference:	127
Appendix	143
A1.	The binary file format of temperature profile.	143

List of figures

Figure 1-1	Procedure of registering the 3D scanner for the ECPT system and 3D thermal point cloud mapping	4
Figure 2-1	Timeline and breakthroughs of the infrared thermography technique.....	10
Figure 2-2	Schematic diagram of ECPT.....	14
Figure 3-1	Three-dimensional eddy current pulsed thermography system	31
Figure 3-2	Three-dimensional scanners Kinect and David 3D	32
Figure 3-3	Camera calibration using checker board.....	36
Figure 3-4	The system diagram of 3D ECPT	38
Figure 3-5	Overview of the proposed feature matching algorithm	39
Figure 3-6	Edge extraction of thermal image and visible image.....	40
Figure 3-7	Construction of the shape descriptor.....	40
Figure 3-8	Weight for different distance	44
Figure 3-9	Rail track feature matching and fusion	47
Figure 3-10	Feature matching and fusion of man-made sample.....	48
Figure 3-11	Structure of Kinect 3D scanner	50
Figure 3-12	Kinect infrared patterns.....	51
Figure 3-13	Iterative closest points algorithm	52
Figure 3-14	Kinect visible-thermal fusion.....	53
Figure 3-15	David 3D scanning system.....	54
Figure 3-16	3D visualization platform.....	56
Figure 3-17	Program structure of 3D visualization platform.....	57
Figure 3-18	Three-dimensional reconstruction, visible and thermal fusion and simulation 59	
Figure 3-19	Defect sizing and localization	60
Figure 4-1	Point cloud command window.....	63
Figure 4-2	The normal vector of rail track head.....	64
Figure 4-3	Defect enhancement, localization and visualization.....	65

Figure 4-4	Selected points locations.....	67
Figure 4-5	Thermal transient response on selected points.....	68
Figure 4-6	Photo and sketch diagram of artificial angular crack sample	71
Figure 4-7	Measured parameters on skewness distributions	72
Figure 4-8	Maximum temperature, $E(x - \text{mean})^3$, <i>standard deviation</i> ³ and skewness 74	
Figure 4-9	Skewness feature on different depth.....	79
Figure 4-10	Histogram of 3mm crack and 0.5mm crack at peak (valley point) and temperature curve.....	80
Figure 4-11	Mean skewness plot of different crack depth.....	81
Figure 4-12	Skewness in different stages of the ECPT experiment	83
Figure 4-13	Design and computation of skewness features.....	85
Figure 4-14	Skewness and crack depth; (a) original temperature response, (b) transformed temperature response with inversion of the heating stage.	86
Figure 4-15	Skewness feature on rolling contact fatigue.....	88
Figure 4-16	Snare, B. (1970), “How Reliable Are Bearings?” The Ball Bearing Journal, 162, pp 3–7. 89	
Figure 4-17	Skewness of RCF slides and X-ray 3D tomography.....	90
Figure 4-18	Three-dimensional gradient and defects	93
Figure 4-19	Defect location and enhancement using fusion with magnetic field.....	95
Figure 5-1	Procedures for the reconstruction and validation of the DTSTD based thermal tomography for artificial and natural defects.....	100
Figure 5-2	Sketch diagram of tomography study on 3D ECPT.....	101
Figure 5-3	Visualization of the 3D heat flow. (a) Single 3D thermal image; (b) 3D Heat flow; (c) 3D sqrt time of temperature drop image (top view); (d) 3D sqrt time of temperature drop image (bottom view).....	105
Figure 5-4	Proposed DTSTD algorithm	106
Figure 5-5	Sectional images and the reconstructed 3D thermal tomographic image (top view).	108
Figure 5-6	Reconstructed 3D thermal tomographic image (color map in jet).....	108
Figure 5-7	Reconstructed artificial angular crack slots under different methods.....	109

Figure 5-8 X-ray CT image and the proposed thermal tomography image (160 kV microfocus) 111

Figure 5-9 X-ray CT image and the proposed thermal tomography image (160 kV microfocus industrial CT)..... 112

Figure 5-10 TSR based thermal tomographic reconstruction on artificial angular crack 115

Figure 5-11 TSR based thermal tomography of angular cracks with different depths. .. 116

Figure 5-12 TSR based thermal tomography of rail track head with RCF crack (defect in left side) 117

Figure 5-13 TSR based thermal tomography of rail track head with RCF crack (defect in left side) (a) DTSTD thermal tomographic reconstruction on 3.5 mm angular crack; (b) TSR thermal tomographic reconstruction on 3.5 mm angular crack; (c) Mesh plot of the skewness feature on 3.5 mm angular crack..... 119

List of publications:

1. **Chen X.**, Tian, G., Wu, J., Tang, C., & Li, K. "Feature-based registration for 3D eddy current pulsed thermography." *IEEE Sensors Journal* 19.16 (2019): 6998-7004.
2. **Chen X.**, Tian G., Ding S., et al. "Investigation of skewness feature for evaluation of defects using eddy current pulsed thermography." *IEEE Sensors Journal* 19.24 (2019): 12118-12125.
3. **Chen, X.**, Tian G., Ding, S., Ahmed, J., & Woo, W. L., "Tomographic Reconstruction of Rolling Contact Fatigues in Rails using 3D Eddy Current Pulsed Thermography," in *IEEE Sensors Journal*, doi: 10.1109/JSEN.2021.3086307.
4. Li, K., Tian G., **Chen, X.**, Tang, C., Luo, H., Li, W., Gao, B., He, X. and Wright, N. "AR-aided smart sensing for in-line condition monitoring of IGBT wafer." *IEEE Transactions on Industrial Electronics*, 66(10) (2019), pp.8197-8204
5. Wu, J., Li, K., Tian, G., Zhu, J., Gao, Y., Tang, C. and **Chen, X.** "Motion-induced eddy current thermography for high-speed inspection." *AIP Advances*, 7(8) (2017), p.085105.
6. Tang, C., Tian G., **Chen, X.**, Wu, J., Li, K. and Meng, H. "Infrared and visible images registration with adaptable local-global feature integration for rail inspection." *Infrared Physics & Technology*, 87 (2017) pp.31-39.
7. Huang, D., Li, K., Tian, G.Y., Sunny, A.I., **Chen, X.**, Tang, C., Wu, J., Zhang, H. and Zhao, A. Thermal pattern reconstruction of surface condition on freeform-surface using eddy current pulsed thermography. *Sensors and Actuators A: Physical*, 251 (2016), pp.248-257.
8. Gao, B., Liu, Y., Ding, C., Liu, S., **Chen, X.**, & Bian, X. (2020). Comparison of visceral fat area measured by CT and bioelectrical impedance analysis in Chinese patients with gastric cancer: a cross-sectional study. *BMJ open*, 10(7), e036335.

Copyright:

In reference to IEEE copyrighted material which is used with permission in this thesis, the IEEE does not endorse any of Newcastle University's products or services. Internal or personal use of this material is permitted. If interested in reprinting/republishing IEEE copyrighted material for advertising or promotional purposes or for creating new collective works for resale or redistribution, please go to http://www.ieee.org/publications_standards/publications/rights/rights_link.html to learn how to obtain a License from RightsLink. If applicable, University Microfilms and/or ProQuest Library, or the Archives of Canada may supply single copies of the dissertation.

Reprint permission:

1. © 2021 IEEE. Reprinted, with permission, from Chen X., Tian, G., Wu, J., Tang, C., & Li, K. "Feature-based registration for 3D eddy current pulsed thermography." IEEE Sensors Journal 19.16 (2019): 6998-7004.
2. © 2021 IEEE. Reprinted, with permission, from Chen X., Tian G., Ding S., et al. "Investigation of skewness feature for evaluation of defects using eddy current pulsed thermography." IEEE Sensors Journal 19.24 (2019): 12118-12125.
3. © 2021 IEEE. Reprinted, with permission, from Chen, X., Tian, G., Ding, S., Ahmed, J., & Woo, W. L., "Tomographic Reconstruction of Rolling Contact Fatigues in Rails using 3D Eddy Current Pulsed Thermography," in IEEE Sensors Journal, doi: 10.1109/JSEN.2021.3086307.

1 INTRODUCTION

This chapter gives a general introduction to the background of eddy current pulsed thermography (ECPT) and an updated three-dimensional (3D) reconstruction technique. Then, the aims and objectives are described, and four sub themes are presented.

1.1 Background

Non-destructive testing and evaluation (NDT&E) is a set of technologies that can provide qualitative and quantitative analysis for defect detection and identification. The ECPT is an emerging NDT&E technique that combines thermography and eddy current induction heating [1-3]. The ECPT system has already shown great potential, especially in sub-surface crack detection, such as in rolling contact fatigue (RCF) in railway tracks [4, 5]. Now, the main interest and challenges lie in the quantification of defects. According to Robert J. Langs (1987), ‘Any reasonable comparison between Aristotle and Galileo shows clearly that there can be no unique lawfulness discovered without detailed quantification’. Although the quantitative evaluation of the defects has improved dramatically in non-destructive testing (NDT) areas over the past years, the ECPT system is still associated with large uncertainties, such as how thermal emissivity occur and reflectivity occur and how the thermal diffusion progression in a complex structure.

With the rapid development of 3D scanning technology, the 3D profile can be acquired at a high refresh speed even with a low cost 3D scanner, such as the ‘Kinect’ manufactured by Microsoft (under 200 pounds with 30 frames per second). Knowledge of precision and quantification of object geometry brings the possibility of solving many uncertainty issues,

such as heat diffusion in complex surface conditions and further analysis of the diffusion into depth. Therefore, it is essential to transform the 2D ECPT into a 3D ECPT.

1.2 Motivations

The NDT&E sprouts and begins during World War II, when there was demand that all war products and goods be defect-free and of high quality. By the 1950s, the strategy in NDT was the ‘zero’ defect strategy. This strategy states that products have to be removed from service if any possible flaw or defect is found. However, in the 1960s, with the emergence of fracture mechanics, people realized that flaws below a critical size are not important in terms of instrument safety issues. The criteria permit the existence of defects in the object if the damage is below a critical level. In the 1970s, when more and more disasters occur, people began to focus on the detectability of the defects because detection was often missed. For example, the report of the F111 aircraft disaster showed that inspection was conducted 11 times and the defect was not found. In the 1980s, the focus was on the requirement of continuing upgrading the inspections in all ageing systems. The requirement of continuous inspection of ageing systems emerged as structure health monitoring in the 1990s.

Nowadays, different NDT technologies can provide high-quality inspection results for defects. The NDT community now focusses on quantitative non-destructive evaluation (QNDE), including the possibility of detection, quantified measurement of defect size and shape reconstruction. In addition, the research of modelled-based analysis and fracture mechanical analysis has boosted NDT from qualitative evaluation to quantified evaluation.

The transient thermal responses in ECPT provide rich information about the defect characteristics because of the complex physical interaction between magnetic fields, eddy currents and joule heating. However, the complex physical interactions also present challenges in the quantification analysis. The 2D ECPT system has many uncertainty factors, including the 3D shape of the testing sample, the measurement of the thermal gradient, the lift-off distance from the excitation coil to the specimen and the directional emissivity issue. With the rapid development of 3D scanning technology, knowledge of precision and quantification of

object geometry brings the possibility to solve these uncertainty issues, such as heat diffusion in complex surface conditions and further analysis of the diffusion in depth. Therefore, it is essential to bring the 2D ECPT into a 3D ECPT framework.

1.3 Aim and objectives

Driven by the motivations outlined above, this thesis aims to design and develop a 3D ECPT systems for NDT&E. The thesis has four main themes and objectives. The four themes are outlined individually in the following sub-sections.

1.3.1 First theme: building the 3D ECPT system

This part of the thesis concerns the set-up of the 3D ECPT system, as well as a literature review of previous ECPT systems. Figure 1-1 gives the outline of the proposed system. The descriptions use this figure as a basis.

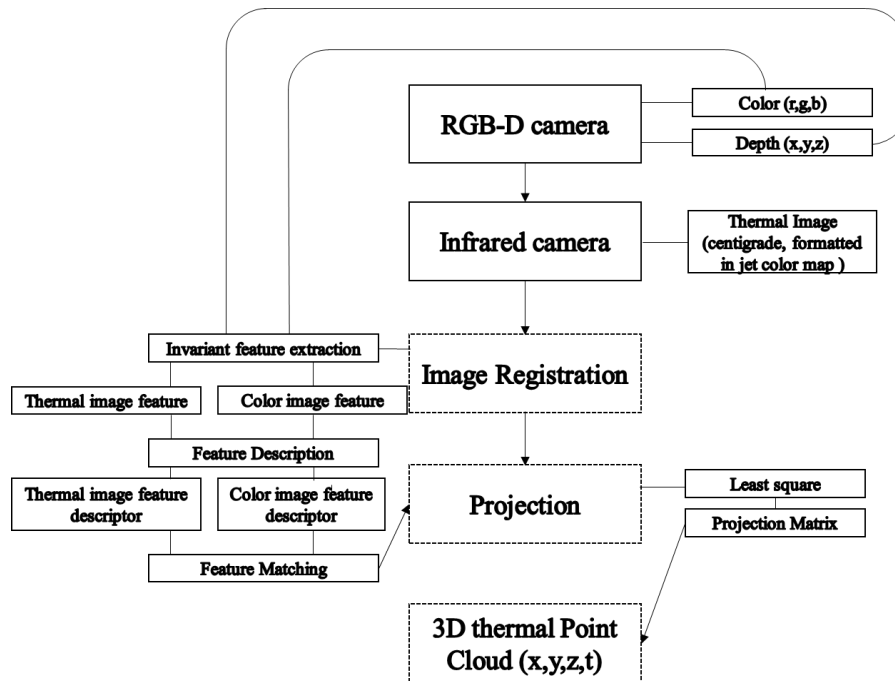


Figure 1-1 Procedure of registering the 3D scanner for the ECPT system and 3D thermal point cloud mapping

The camera system consists of an RGB-D camera and an infrared camera. Two sources of the information are recorded by the RGB-D camera which consists of the visible color information of the object in R, G, B and the geometry information as x, y, z . The coordinate system of the depth camera is referenced as the depth camera itself.

Most works use a calibration board for the registration of the two camera systems. In this work, instead of using a calibration board, a feature-based self-calibration method is proposed in which the common features in the RGB image and the thermal image are found. However, because of the different modalities of the two images, the information they contain is highly different from one to the other; the thermal image contains thermal radiation, whereas the visible image is the light reflection in the visible band. Hence, the challenges lie in extracting and matching the common features of these two modalities of the images. The feature matching basically consists of three steps—feature extraction, feature description and feature matching based on the feature descriptor. The commonly used feature descriptor cannot provide enough information for correct feature matching. A new descriptor for infrared image and color image registration is proposed in chapter 3.

After feature matching, the thermal image is registered to the point cloud via a projection matrix. The projection matrix was calculated by the matched features using the least square method. The more correct the matching features, the more accurate the projection matrix is. Generally the projection matrix gives the correspondence of color image pixel location and the real geometry location x, y, z :

$$z \begin{bmatrix} u \\ v \\ 1 \end{bmatrix} = \begin{bmatrix} m_{11} & m_{12} & m_{13} & m_{14} \\ m_{21} & m_{22} & m_{23} & m_{24} \\ m_{31} & m_{32} & m_{33} & m_{34} \end{bmatrix} \begin{bmatrix} x_w \\ y_w \\ z_w \\ 1 \end{bmatrix} = \mathbf{M}\mathbf{X}_w \quad (1-1)$$

where (u, v) is the pixel location of the color image and (x_w, y_w, z_w) is the geometry location in the 3D world space. The subscript ‘w’ denotes the 3D point in the world coordinate system. \mathbf{M} is the projection matrix and the vector \mathbf{X}_w is the 3D point in the world coordinate. Mathematically the projection matrix is determined by the camera’s intrinsic parameter matrix and extrinsic parameter matrix:

$$z \begin{bmatrix} u \\ v \\ 1 \end{bmatrix} = \begin{bmatrix} a_x & 0 & u_0 & 0 \\ 0 & a_y & v_0 & 0 \\ 0 & 0 & 1 & 0 \end{bmatrix} \begin{bmatrix} \mathbf{R} & \mathbf{t} \\ \mathbf{0}^T & 1 \end{bmatrix} \begin{bmatrix} x_w \\ y_w \\ z_w \\ 1 \end{bmatrix} = M_1 M_2 X_w = M X_w \quad (1-2)$$

Here, M_1 is the intrinsic parameter matrix, M_2 is the extrinsic parameter matrix and M is the projection matrix. In the intrinsic matrix, all the parameters are related to the camera intrinsic property. Here, a_x, a_y are the camera focus length, whereas u_0, v_0 are the optic centre of the camera. The extrinsic matrix M_2 denotes the translation from the object camera to be transferred (thermal camera) to the reference camera (3D RGB-D camera). The matrix \mathbf{R} is a 3×3 rotation matrix and \mathbf{T} is the translation matrix where

$$\mathbf{R} = \begin{bmatrix} \cos\alpha & -\sin\alpha & 0 \\ \sin\alpha & \cos\alpha & 0 \\ 0 & 0 & 1 \end{bmatrix} \begin{bmatrix} \cos\beta & 0 & \sin\beta \\ 0 & 1 & 0 \\ -\sin\beta & 0 & \cos\beta \end{bmatrix} \begin{bmatrix} 1 & 0 & 0 \\ 0 & \cos\gamma & \sin\gamma \\ 0 & \sin\gamma & \cos\gamma \end{bmatrix} = \begin{bmatrix} \cos\alpha\cos\beta & \cos\alpha\sin\beta\sin\gamma - \sin\alpha\cos\gamma & \cos\alpha\sin\beta\cos\gamma + \sin\alpha\sin\gamma \\ \sin\alpha\cos\beta & \sin\alpha\sin\beta\sin\gamma + \cos\alpha\cos\gamma & \sin\alpha\sin\beta\cos\gamma - \cos\alpha\sin\gamma \\ -\sin\beta & \cos\beta\sin\gamma & \cos\beta\cos\gamma \end{bmatrix} \quad (1-3)$$

$$\mathbf{T} = \begin{bmatrix} T_x \\ T_y \\ T_z \end{bmatrix} \quad (1-4)$$

Equation (1-3) gives the mathematical representation of a 3D rotation where α , β and γ are the yaw, pitch and roll. Equation. (1-4) is the translation matrix. The projection matrix gives the mapping relationship from the RGB-D image to the thermal image. Section 3.1 will give the method for solving the projection matrix in detail. After registration, the thermal point cloud set (x, y, z, temperature) is visualized as illustrated in section 3.3.

1.3.2 Three dimensional visualization, multi-modality imaging fusion and defect detection

This part of the thesis concerns the description of the 3D visualization system and the multi-modality imaging fusion, as well as the case studies of defect detection and localization with the 3D ECPT system.

Multi-modality imaging is becoming a standard practice not only in illness detection in the clinical area, but also in the NDT&E area. The multi-modality imaging normally consists of two or more imaging sources, such as visible imaging; far-field infrared (IR; thermal) imaging; near-field IR (reflected IR) imaging; and ultrasonic, magnetic and other electromagnetic field imaging. The functions and benefits of multi-modality imaging for NDT&E should basically provide a more accurate location of defects and clearer resolution of the damage around the defect area and eventually, it should help damage assessment.

Multi-modality imaging is usually set within one experimental examination study. Here, two imaging devices are placed at different viewing angles. The image registration must be processed before fusion of the two or more modality images. Because of projection distortion, there will always be errors when aligning images at different viewing angles. The 3D profile provided by a 3D scanner can be set as a standard world coordinate system. Thus the registration of multi-modality imaging can be treated as an error-free fusion with the 3D profile.

The fusion of RGB-D and thermal image is illustrated in chapter 4. The comparison of 2D fusion and 3D fusion is discussed. In addition, the defect detection using skewness feature and visualization in 3D is presented, where it can be found that the 3D visualization gives a more accurate location and resolution of the damaged area.

1.3.3 Three dimensional thermal imaging and analysis: 3D defect localization and quantification and thermal point cloud defect enhancement.

In this part of the thesis, thermal imaging with 3D information is addressed because single infrared imaging is usually insufficient for inspecting objects of complex shape. Additional information like the viewing angle, and geometry can help to enhance these uncertainty factors. For example, the visible image can bring information of about the object contour, whereas thermal imaging is quite blurred when it comes to the object contour.

The previous chapter has already achieved the fusion of thermal imaging with spatial information. Chapter 4 accounts for the spatial information for the analysis of heat spreading in the 3D dimension, which helps in the diagnosis of defect damage through the heat spreading

effect. Furthermore, a study of enhancing the defect area by the fusion of the calculated magnetic field induced by the coils is presented.

1.3.4 Tomographic reconstruction of the 3D ECPT.

Tomography analysis is a non-destructive method that analyses the object layer by layer (in slices). The research on tomographic reconstruction mostly lies in X-ray imaging, ultrasonic imaging or magnetic resonance imaging (MRI). Researches on thermal tomographic reconstruction is hard to conduct because thermal energy penetrates not only vertically, but also horizontally. Thermal tomography provides advantages in NDT such as in its non-radiative, fast inspection, one-sided and low-cost properties. In this part of the thesis, we investigate the use of the 3D ECPT system for tomographic reconstruction.

RCF in rail tracks is considered one of the main causes for train derailment. In addition, the RCF is a governing reason for rail maintenance and replacement. Thus, it has become a research subject in most countries with railroad systems including the United Kingdom, the United States, China, Canada, Japan, Russia and Brazil. Research has shown that surface-initiated RCF cracks are more common, but sub-surface-initiated RCF cracks are more severe. The requirement of accurate surface and sub-surface RCF cracks inspection, evaluation and quantification is a challenge for rail safety. This work investigates the use of 3D ECPT for RCF tomographic reconstruction.

With the recent advancement of NDT in 3D reconstruction-based tomographic approaches for internal and sub-surface defects, the qualitative and quantitative analysis of RCF types and shapes becomes a crucial and urgent task. The X-ray based computed tomography (CT) has good results for depth estimation in NDT problems. However, the equipment is expensive and bulky, and it poses the risk of radiation effects if continuously used. In addition, the X-ray is unable to penetrate the entire rail, which makes it hard to use X-ray CT for online inspection of RCF cracks. The high-energy industrial CT (above 4 MeV) could penetrate the entire rail track head. However, the higher the energy of the X-ray, the lower the resolution (for 4 MeV, the resolution is 1mm), which makes it impossible to identify

RCF cracks in the rails. The ultrasonic approach has relatively good reconstruction of inner defects. However, it has very low resolution on surface crack reconstruction, which makes it inappropriate for RCF inspection. This thesis first proposed a thermal tomographic approach for the RCF reconstruction. Chapter 5 illustrates the methodology in detail.

1.4 Novelties and contributions of the work

The PhD project aims to establish a 3D ECPT system for QNDE. The major novelties and contributions of the work include the following:

- Establishing the first 3D thermography system for ECPT.
- Proposing and building a feature-based thermal-3D registration algorithm. A shape constrained Scale Invariant Feature Transform (SCSIFT) feature descriptor is designed to find and match the common features from the thermal image obtained from the infrared camera and the RGB-D image from the 3D scanner.
- Quantifying defects based on the ECPT system. A skewness feature is proposed and developed for the quantification of the defect depth.
- Proposing the thermal tomographic reconstruction of the 3D ECPT system.

2 LITERATURE REVIEW

This chapter provides review of the ECPT system and its application in the past few years to address the aim and objectives of the study. In recent years, 3D technology has developed rapidly. Numerous 3D scanning and relevant reconstruction algorithms have emerged. This thesis concentrates on reconstructing 3D thermography with an RGB-D camera and thermal IR camera. The literature review of the recent 3D reconstruction, 3D thermography and image registration are investigated. Finally, to realize the quantitative analysis of the defect and compare it with other NDT&E technologies, the progress of quantitative NDT&E in recent years is presented.

2.1 Thermography and application of NDE

2.1.1 State of the art of thermography

Thermography is the recording of the temperature distribution of an object's surface and formation into an image (thermogram). The term thermography includes 'contact thermography' and 'microwave thermography'[6]. Among the thermography types, IR is the most common method to detect radiation in the long IR range of the electromagnetic spectrum (9~14 μ m).

The history of thermography begins with Sir William Herschel (1738-1822) who first discovered the IR spectrum. In the 1880s and 1990s, Lord Rayleigh and Wilhelm Wien both solved part of the blackbody equation. In the 1950s–1960s, IR thermography underwent a big jump. Before 1955, Honeywell and Texas Instrument had generated IR images. In 1965, Barnes and Agema published the first IR handbook. Then, in 1978 FLIR was founded as a leader of thermal IR camera providers. Figure 2-1 shows the milestones of thermography.

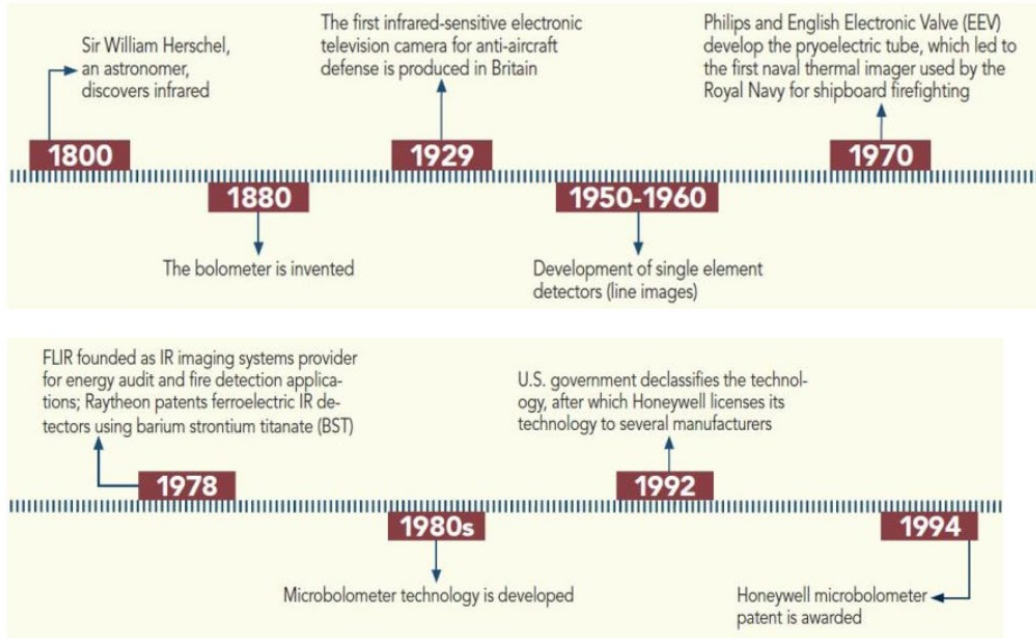


Figure 2-1 Timeline and breakthroughs of the infrared thermography technique

2.1.2 Heat transfer

There are three principal ways of bringing about heat transfer—conduction, convection and heat radiation. *Conduction* dominates the heat transfer in solids. It is the heat propagation of two solid bodies when there exists a heat difference. *Convection* is the major factor in the propagation of heat energy in gas and liquids. It involves the mass movement of molecules in gas or liquids over a large distance. Convection also lies in the boundary of solids and fluids. Finally, *Heat radiation* is internal energy transfer via electromagnetic waves. It present in all matter with a temperature above absolute zero.

Conduction in solid matter is governed by Flic’s second law of diffusion (in one dimension[1D]), where

$$\frac{\partial T}{\partial t} = \alpha \frac{\partial^2 T}{\partial x^2} \quad (2-1)$$

Here, α is the thermal diffusivity.

The heat radiation emitted by the black body is governed by Plank's law

$$K_B(\lambda, T) = \frac{2hc^2}{\lambda^5} \frac{1}{e^{\frac{hc}{kT\lambda}} - 1} \quad (2-2)$$

where h is the Plank constant; k is the Boltzmann constant, c is the speed of light and λ is the wavelength.

The Stefan-Boltzmann law describes the total energy emitted by a black body. Specifically, it states that the energy emitted by unit time is proportional to the fourth power of the black body's absolute temperature:

$$K_B(T) = \sigma T^4 \quad (2-3)$$

2.1.3 Thermography of NDE

IR thermography has wide applications in the NDE area because of its non-contact (large lift-off), rapidity and wide area inspection properties. This approach is used not only to evaluate the material's thermal properties, but also to find flaw discontinuities caused by corrosion, delamination or cracks. IR thermography can be applied to a wide range of materials from fibres, and metals to composite material. To meet the requirements of different applications and materials inspection, a number of NDT thermography techniques have been developed such as flash thermography, ultrasonic thermography, laser thermography and ECPT.

2.1.3.1 Flash thermography

Flash thermography uses a set of flashing lamps and applies the thermal heating pulse to the testing sample. During the experiment, the cooling process of the specimen is recorded by the IR camera. Flaws in the specimen will cause a discontinuity of heat flow, which will be observed and analyzed.

Many methods have been developed using flash thermography to estimate defect depth and size. Researchers have already proved that instead of analysing the single best contrast frame, analysing the whole thermal sequence can give better defect detection and quantification result. The most popular thermal video sequence analysing methods are thermographic signal reconstruction (TSR) and pulse phase IR thermography (PPT).

TSR uses time information whereas PPT analyses the frequency domain. In 1996, Maldague X [7] first proposed a TSR algorithm. TSR fits the temperature curve to a polynomial in the logarithmic domain. In addition, [8] used TSR to analyse the cracks in turbine blades. In contrast, PPT transforms a temperature-time video into the frequency domain and performs analyses via amplitude and phase image. A PhD thesis [9] gave a detailed explanation of PPT with applications. Moreover, [10] and [11] compared TSR and PPT.

2.1.3.2 Ultrasonic thermography

Ultrasonic thermography is also termed sonic IR, vibro IR or acoustic thermography [12-15]. In the 1970s, Henneke et al. [12] first proposed the ultrasonic thermography with a transducer and IR camera for thermal video capture. The authors claimed that this method can detect most cracks in a variety of materials. Since its initial description, ultrasonic thermography has been applied to a wide field of applications.

The ultrasonic thermography system consists of a vibration source, IR camera, computer and sometimes a laser vibrometer for the measurement of the amplitudes and frequencies of the mechanical wave. Compared with other NDT thermography techniques, it has the advantage of detecting micro-cracks and cracks under the surface [16]. Han et al. [17] applied this technique in the aerospace industry. They successfully and efficiently detected tiny cracks ($20 \mu m$) in the aircraft engine disc. Ultrasonic thermography also works well in composite material. Reference [18] introduced ultrasonic IR thermography in the inspection of cracks in carbon fibre reinforced plastic (CFRP). However, it has also been proven that ultrasonic thermography does not work well in certain materials, such as austenitic steel.

2.1.3.3 *Laser thermography*

Laser thermography uses a laser beam with several watts and heats the sample in a spot heating manner. Many applications of crack detection in metals and composite material have been developed. Reference [19] established a numerical model for studying heat diffusion phenomena via laser thermography. The finite element method (FEM) was used for surface crack detection and simulation. Reference [20] delivered a fibre-guided laser array spot thermography (LAST) system, and this proved to have good performance and robustness on metallic structure crack detection. Reference [21] gave a quantitative evaluation of defect depth using the neural network and validated it via experimental study and simulation. Moreover, [22] compared thermosonics and laser thermography, and the author claimed that both techniques are useful in finding delamination. Compared with laser thermography, sonic thermography can find deeper defects with more precision. Meanwhile, laser thermography has a wider inspection range and quicker inspection time. (It only needs one measurement, whereas sonic thermography needs multiple measurements).

2.1.3.4 *ECPT*

ECPT is a multi-physics system that contains interaction between the eddy current, joule heating effect and heat conduction. Figure 2-2 shows the overall 3D ECPT system. The signal generator sends a pulse signal and triggers the induction heater. A period of high power and high-frequency alternating current is generated by the induction heater and goes through the inductive coil. The eddy current is then induced on the surface of the testing sample. When the eddy current encounters defects, there is a discontinuity of both electrical conductivity and magnetic permeability, and the eddy current leads to diversion.

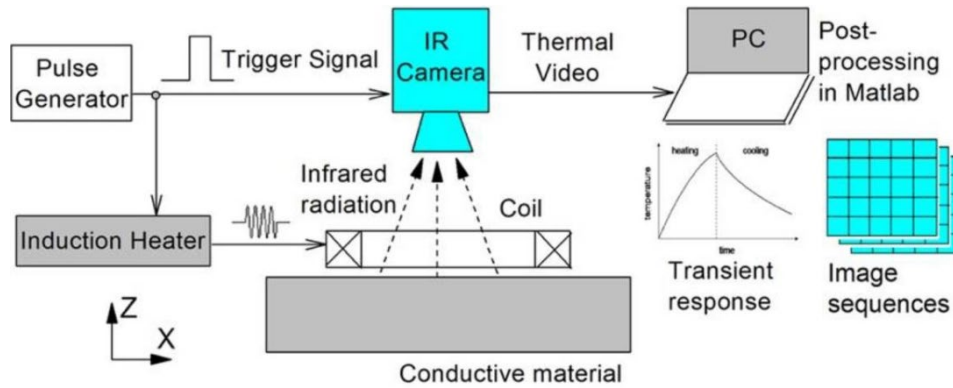


Figure 2-2 Schematic diagram of ECPT

In contrast to laser thermography or flash thermography, which only uses the cooling stage for defect detection, ECPT utilises the heating stage for defect detection while in the cooling stage, and it gives more information for quantitative evaluation.

The ECPT system has been used in a wide range of material inspection including metallic material and composite material. Reference [23] investigated using inductive heating thermography on different steels. In addition [24] successfully used the ECPT system to detect the impact damage of carbon fibre reinforced polymer. Most of the ECPT experiments were carried out on reflection modes. Reference [25] proposed a combination of the ECPT reflection model and transmission model. In addition, Li, K [26] applied an ECPT system to the investigate bond wire conditions in IGBT modules.

Overall, the ECPT is a non-destructive and multi-physical method that can detect not only surface defects, but also sub-surface defects. The hybrid and multi-physical properties of the ECPT system provide rich information on decision making. However, they also presents a higher challenge in terms of quantitative analysis.

2.1.3.5 Summary of IR thermography NDT techniques

In this section, different active IR thermography methods are discussed and compared. Active thermography can be categorised according to its active excitation sources and its modulation type. For different excitation sources, there are radiation type, convection, thermal conduction and internal sources. The radiation type and internal sources are most frequently

used. They have unique advantages and limitations; for example, induction heating-based thermography can only be applied on conductive material. Ultrasonic thermography is hard to apply to material with complex shape, such as for defects in gears, and it has a relatively low resolution of surface defects. Radiation thermography, including laser and flash thermography, is strongly influenced by the material's reflectivity and emissivity. The thermal conduction needs direct contact with the object's surface. The advantages and disadvantages found in the references are shown in Table 1.

Table 2 gives a comparison of different active IR thermography types categorised by their modulation. Pulsed thermography, step-in thermography, long-pulse thermography and lock-in thermography are listed and compared. Their excitation heating time is gradually increased, where pulsed thermography has the lowest excitation heating time and lock-in thermography usually has the longest heating time duration. The first three—which are pulsed, step-in and long pulse types—only consist of one heating period, whereas lock-in thermography consists of multiple heating periods. This modulated thermography is widely used in radiation thermography, such as flash and laser thermography and internal source thermography, including induction thermography and ultrasonic (mechanical wave-based) thermography.

External sources			
Category	Heating sources	Advantage	Disadvantage
Radiation	Flash [27-29], halogen lamp [30]	Non-contact, quick inspection; large area inspection; quantified thermal excitation	Low thermal contrast, very sensitive to the surface condition of the material
	Laser [31-33]	Non-contact, high contrast, quick excitation and good quantification	Potential of eye hazard, sensitive to surface condition of the material, small area inspection.

Convection	Hot/cold air blower [34]	Robust to surface condition; reduces the contaminant influence with air blowers	High power consumption, sensitive to geometry shape and air flow direction; potential environmental disturbance
Thermal conduction	Cold/hot compress [35]	Robust to geometrical shape; widely used in medical applications because of the lowest influence on the human body	Needs direct contact of specimen surface. very long excitation time; normally, 10-20 minutes of cold compress on the human body is required
Internal sources			
Sources	Advantages	Disadvantages	
Sonic [36, 37] or ultrasonic [38-41]	Internal volume heating; good ability of internal and deep defect detection	Weak in surface defect detection; significant noise; contact excitation on surface or acoustic couplant is needed	
Induction heating [42, 43, 60]	Internal volume heating. High detection resolution in surface and sub-surface range. Quick inspection and non-contact	Uneven heating. Only effective for conductive material.	

Table 1 Active infrared thermography categorized by excitation sources

Modulation types	Advantage	Disadvantage
Pulsed thermography [44-47]	Short excitation time and better resolution of shallow cracks; all frequencies' information of the excitation signal	Image becomes blurred with time; suffers from reflectivity and emissivity issue

Step-heating thermography [48,49]	Stabilise the image with time; possible to find deeper cracks	Longer inspection time; not full frequency information
Long pulse thermography [50,51]	Suitable for low thermal conducting material	Very long inspection time
Lock-in thermography [52- 54]	More robust for the reflectivity and emissivity issue of material surface	Suffers from blind frequency where the defects in some phase images disappear

Table 2 Active infrared thermography categorised by modulation type

2.2 3D reconstruction and image registration

Owing to the high speed and relative cheapness of computers, 3D imaging devices have won more and more applications. Compared with two-dimensional (2D) imaging, the 3D imaging gives the real geometry of the world. Particularly, many studies have been conducted such as life science [55-56], civil engineering [57] and information science [58].

The highly developed computer devices industry has also boosted the 3D imaging devices. The recently developed 3D imaging devices, such as Kinect, can achieve high speed scans up to 30 frames per second. The 3D imaging technology can be generally categorised as laser based or camera based. Laser scanning is well-known in Lidar devices. Camera-based method includes stereo vision, structure light projection and structure from motion.

2.2.1 Review of 3D scanning techniques

There are many methods for acquiring an object's 3D profile. The popular 3D scanning technologies include passive stereo vision (two or more camera systems) [59-62], active stereo vision (structure light projection) [63-66] and time of flight (TOF; Lidar, Kinect system) [67-

70]. In addition, it is worth noting that these 3D scanning technologies complement each other [71]. C. Netramai, et al. [72] proposed a 3D scanning method by combining TOF camera and stereo camera. The results prove that the combination of ToF camera and stereo vision camera improves the range data significantly.

The stereo vision system uses triangulation to calculate depth information. Passive stereo vision uses matched features, whereas the active stereo vision uses projected lighting patterns to obtain depth. The structure light projection projects pre-defined pattern sequences to the object. The patterns are captured by a paired camera, where the image is filled with deformed patterns caused by the object shape. The depth information is calculated by analysing the distortion of the patterns. There are different ways of defining the structure light patterns. The simplest method is the stripe pattern with binary coding [73]. Fechteler et al. [74] used color stripe patterns to reconstruct the high-resolution 3D images.

Passive stereo vision is the most economical and convenient way of 3D capture. The system requires only a stereo vision camera rig [62, 75] or even a monocular camera with structure from a motion algorithm [75-78]. The stereo vision system reconstructs the 3D environment via matched features. Thus, its performance suffers if the scenery has insufficient features. Compared with passive stereo vision, the active stereo vision system (structure light projection) projects lighting patterns on the object. As a result, it can deal with scenes that do not have enough texture information. However, the structure light projection is highly sensitive to environmental lighting conditions. Thus, the structure light projection method can only be applied in the indoor environment. The TOF camera, which is different from the stereo vision camera—that calculates triangulation—emits a reflective light and measures the depth information by calculating the travelling time of the light reflecting back to the camera.

2.2.2 Kinect and David 3D scanners

To meet the different applications of the 3D ECPT system, two 3D scanning systems are chosen for the 3D profile rendering—the Kinect structure light camera and David 3D scanner.

In November 2010, Microsoft released the first version of the Kinect system for Xbox. Since then, two different Kinect systems have been offered: Kinect structure light (SL) and Kinect ToF. As mentioned above, as different range sensing techniques, SL and ToF have different advantages and disadvantages, and they may also complement each other with error fixings. Reference [79] gave a detailed comparison of the Kinect SL and ToF systems. For the ECPT system, the selection of 3D scanners is mainly based on two key factors—the influence on ambient light and the influence on shiny surface objects.

First, the Kinect SL camera and the Kinect ToF camera use different depth sensing techniques. The Kinect SL camera is based on near-IR structure light projection. The system is composed of an 850 nm near-IR projector, a near-IR camera and a visible camera. The near-IR projector projects dot patterns on the object, which are captured by the near-IR camera. The depth information is estimated using these dot patterns by calculating their triangulation relationships. To achieve high-speed 3D scanning (30 frames per second), the Kinect SL only uses a low number of patterns.

With the breakthrough of microelectronic devices, a new range sensing device—the ToF camera emerged. Unlike Lidar devices, which directly measure the travelling time of light, the Kinect ToF camera utilises continuous wave (CW) intensity modulation. The key idea of CW technology is to modulate the infrared emitter wave and calculate the phase shift of the IR wave captured by the receiver [80].

The IR emitter sends an IR wave signal as follows:

$$S_E(t) = A_E[1 + \sin(2\pi ft)] \quad (2-4)$$

where $S(t)$ is the IR wave signal with an amplitude of A_E and frequency of f . Then, the signal S_E is reflected back and reaches the receiver as

$$S_R(t) = A_R[1 + \sin(2\pi ft) + \varphi] + B_R \quad (2-5)$$

where $S_R(t)$ is the received signal with the amplitude of A_E and a phase delay of φ . B_R is the energy loss when the signal reaches the receiver. The coefficients of A_R and B_R are measured as volts. In addition, φ is the most important parameter, indicating the distance as

$$\varphi = 2\pi f t = 2\pi f \frac{2D}{c} \quad (2-6)$$

$$D = \frac{c}{4\pi f} \varphi \quad (2-7)$$

To obtain the phase shift φ , the A_R and B_R are estimated via measuring the signal of $S_R(t)$ four times per period. Thus, four sample signals of $S_R^0(t = 0)$, $S_R^1(t = \frac{1}{4f})$, $S_R^2(t = \frac{1}{2f})$, and $S_R^3(t = \frac{3}{4f})$ are obtained.

After some simple algebraic manipulation, the following expressions are obtained:

$$\hat{A} = \frac{\sqrt{(S_R^0 - S_R^2)^2 + (S_R^1 - S_R^3)^2}}{2} \quad (2-8)$$

$$\hat{B} = \frac{S_R^0 + S_R^1 + S_R^2 + S_R^3}{4} \quad (2-9)$$

$$\hat{\varphi} = \arctan(S_R^0 - S_R^2, S_R^1 - S_R^3) \quad (2-10)$$

Finally, the distance is calculated as:

$$\hat{D} = \frac{c}{4\pi f} \hat{\varphi} \quad (2-11)$$

The David 3D scanner shares the same working principle as the Kinect SL camera, which uses structure light projection for 3D reconstruction. The David 3D uses a high-resolution visible camera (Kinect SL near-IR) and multiple stripe patterns (Kinect SL uses few patterns or even a single pattern) to reconstruct the 3D profile; thus, it has a much higher resolution compared with Kinect SL (up to 0.5 mm). In compensating for the high resolution, it also takes a much longer time of 2 minutes per scan.

Reference [79] made an elaborative comparison between the Kinect SL camera and the Kinect ToF camera. The researchers claimed that for the ambient background light, the Kinect SL camera is unable to handle strong light over $1\mu w$. However, compared with the Kinect ToF camera, it has a more robust depth measurement in the working ambient background light range. In the 3D capture of the shiny surface, the Kinect SL camera also performs better and causes fewer problems compared with the Kinect ToF camera. Because the Kinect SL camera

is more robust to the contexts of both shiny surfaces and ambient background light, here, the Kinect SL camera is used together with David 3D for range image capturing.

2.3 Feature extraction and quantification of ECPT

Non-destructive evaluation aims to acquire knowledge of a material structure's health and reliability. The high demand and importance of high-cost structure inspection resulted in the evolution of NDT from a qualitative to a quantitative manner. The high-cost structures considered bridges, aerospace and new energy devices. The primary interest of QNDE lies in assessing the state of the material, including the defect size and how it results in failure.

A quantitative evaluation must stand in terms of the quantitative model and quantitative measured data. A good numerical model is of vital importance in comprehending the experimental process using measured data. The characteristics of defect features can be further analysed with the numerical model, which facilitates the process from qualitative analysis to quantitative analysis. IR non-destructive techniques are now widely applied in defect detection because of their wide inspection range and high-speed inspection. The ECPT system is an active thermal IR non-destructive evaluation method that is used for conductive defect detection. The ECPT system uses the eddy current as an external heating source for active heating. Therefore, it gives a higher contrast between the defective area and the non-defective area. However, in some cases, the defective area and non-defective area have the same temperature which cannot reveal the hidden flaws [82]. Thus, it is desired to establish the prior knowledge of the following:

- a) The geometric shape of the testing sample.
- b) The position of the heat source and heating model.
- c) The type of thermal heating experiment and parameters (power, heating time).

Based on the ECPT system, different applications and methodologies of defect detection emerge. Oswald and Tian used ECPT to investigate penetration depth of temperature and analyse the defect via experimental studies and simulations [82]. Chen, L. investigated a

pattern-level feature of thermal transient response using integration of principal component analysis (PCA) and independent component analysis (ICA) [83]. This work used PCA for dimension reduction, orthogonal transformation and defect area separation. The work successfully extracted thermal patterns according to the thermal transient response. Libing Bai also presented a pattern level feature of transient thermal response using blind source separation [84]. This method has been validated through the artificial slot and thermal fatigue of natural cracks. However, it is hard to use the pattern-level features (high-level features) for the quantitative analysis of defect characteristics, including precise localisation, sizing and depth estimation.

Instead of using time domain features, He, Y. et al. investigated the angle in the frequency domain of the transient thermal response [85]. Different phase features were extracted and analysed. The results showed that the phase features from the frequency domain successfully eliminated the non-uniform heating effect from ECPT, and the phase features were validated to have a linear relationship to the defect depth. However, the work done was on a planar surface sample; moreover, the frequency features suffered from the problem of lack of spatial and geometry information, making it difficult to work on the 3D object with a complex structure. In the phase image, some edges of the testing object disappear while some additional phase edges appear, bringing ambiguity for the defect identification in the complex structure object. Jia Liu et al. analysed the early contact fatigue of the gear using ECPT in an optical flow analysis manner [86].

Above all, the qualitative analysis of defects in ECPT has been studied using IR image processing. The quantitative analysis of defect size and depth has not been studied well. Shi, Z [87] conducted a quantitative study on defect sizing on steel using ECPT. The 2D imaging edge detection approach was used to classify and identify cracks. However, for complex objects, this method cannot give accurate sizing of defects because of the distortion of projection.

To boost ECPT technology from a qualitative manner to a quantitative manner, both the analytical model and numerical model have been studied by researchers in recent years.

2.3.1 Analytical study and physical comprehension for ECPT

The physical model for the ECPT system is based on Maxwell's equation and heat conduction. Compared with numerical simulation, the analytical model shows advantages in physical comprehension and physical phenomenon characterisation, which is vital for inverse engineering.

For homogeneous field excitation which is parallel to the specimen surface, the depth is given by

$$\delta = (\pi\mu\sigma f)^{-1/2}. \quad (2-12)$$

where δ is the current penetration depth, μ, σ are the magnetic permeability and electrical conductivity, and f is the frequency of the excitation signal. When the electrical magnetic field reaches the conductive material, the joule heating effect is induced as:

$$Q = I^2 R = \frac{1}{\sigma} |\sigma E|^2 \quad (2-13)$$

It is worth noting that electrical conductivity also has a relationship with temperature rising, expressed as

$$\sigma = \frac{\sigma_0}{1 + \alpha(T - T_0)} \quad (2-14)$$

where σ_0 is the material conductivity at the reference temperature T_0 and α is the coefficient of temperature resistivity. Finally, the heat diffusion process is governed by

$$\frac{\partial T}{\partial t} = \frac{\lambda}{\rho C_p} \left(\frac{\partial^2 T}{\partial x^2} + \frac{\partial^2 T}{\partial y^2} + \frac{\partial^2 T}{\partial z^2} \right) + \frac{1}{\rho C_p} q(x, y, z, t) \quad (2-15)$$

where ρ , C_p and λ are the material density, heat capacity and thermal conductivity, respectively; $q(x, y, z, t)$ is the unit internal heat generation caused by the eddy current; T is the heat diffusion; and (x, y, z) are the Euclidean coordinates.

References [88] gave a physical explanation of ECPT. Blind source separation was proposed for transient pattern extraction. A physical explanation was also given in the article. Reference [89] performed an analytical study on ECPT at different excitation studies for metallic material study [90] analysed the patterns of defects in the ECPT experiment and proposed the pattern separation model.

Until now, the analytical model of the ECPT system has not been completed, especially for a complex defect structure. The complex multi-physical interaction in the ECPT experiment requires a more quantified study in physical parameter quantification, pattern (feature) level and numerical simulation study.

2.3.2 Numerical study of ECPT

Numerical models are mathematical tools based on pre-set physical rules; they follow a procedure of time-stepping iterations. They are also a valuable tool that can validate the results of the experimental study. [91] Compared with the analytical model, the numerical model is more flexible and able to handle models with complex physical interactions and complex structures.

The WPUT group has conducted numerous numerical simulations of heat transfer in different materials induced using various energy sources. The FEM was utilised with both stationary and time-dependent solvers. Using this method, it is possible to solve so-called multi-physics problems, where the set of differential equations related to different physical phenomena are to be solved. This is especially important in microwave heating simulations, where electromagnetic wave propagation has to be considered. These research results were published in peer-reviewed journals and presented during important conferences dedicated to thermography. Numerical simulations were conducted, including the following:

- (a) Microwave heating used in underground object detections. In this task, various problems were analysed—that is, influence of chosen external conditions on microwave heating efficiency, optimisation of the heating device, and detected objects parameters reconstruction

- (b) Microwave heating of composite structures used in wind turbine blades
- (c) Optical heating of various composite structures. This includes the aspect of detected defects parameters' reconstruction.

In addition, researchers in Poland conducted a series of experiments based on multi-mode stimulation to detect defects in the GFRP samples with artificial defects. The WPUT group developed thermography techniques based on halogen-lamp-microwave and cool-down excitation to enhance the detection capacity with multi-mode thermography, especially when detecting internal defects [92].

2.3.3 Relevant work on IR thermography-based NDT and challenges

According to the radiative thermal simulation by Thomas [93], the radiation captured by sensors is determined by the target's temperature, the sensor area, the distance between the power source and the sensor, and the angle concerning incident rays. This brings difficulties for such applications as wind turbines. The surface of a wind turbine blade is large and complex, and the curvature will affect the radiation we obtain from the IR thermal images. Xavier [94] suggested that the best solution is using a 3D camera to obtain both orientation and distance from the surface. With the development of 3D techniques, the price of the 3D camera goes down and the quality of 3D images goes up. In addition, new method and algorithm emerge to process the 3D images.

Passive 3D thermography is effective in qualitative diagnosis. Hellstein [95] applied 3D passive thermography in the non-destructive testing of composite structures like boats, planes and wind turbines. In medical monitoring, Barone [96] and Grubisic [97] realised the preventive detection of diabetic foot disease and breast cancer. To quantitatively analyse the depth of defects, 3D active thermography is necessary. Akhloufi [98-100] developed an integrated algorithm to detect the sub-surface defects and display the defects on the 3D model. Feature extraction, image registration, depth estimate, defect segment and 3D visualisation are used to determine the defect depth and location. The algorithm was tested on metals and composites with flash-tube excitation. However, the emissivity is still unresolved. Besides,

Lagüela [101] and Tang, C. [102] attempt the building and rail inspection with registration and fusion of IR and visible images.

Model-based defect characterisation works successfully in the lab environment but fails when the 1D assumption is broken [103]. Using the back-propagation [104] algorithm, deep learning modifies the parameters of the network and discovers features in a large amount of data. Deep learning has made great progress in computer vision, natural language processing, and other fields. Deep convolutional neural networks (CNNs) [105, 106] have made remarkable progress in image recognition, with the help of the availability of large-scale annotated datasets (i.e., ImageNet [107, 108]). CNNs enable learning data-driven, highly representative, layered hierarchical image features from sufficient training data [109]. Although CNNs perform well in the recognition and classification of visible images, the use of CNNs to classify IR thermal images is still a challenging task because of the lack of IR thermal datasets similar to ImageNet [107, 108], which has a large amount of labelled data. Some researchers apply CNNs to the identification and classification of IR targets [110, 111], but the application of CNNs in the field of NDT is still challenging to evaluate materials and monitor machines [112-113].

The active thermography-based NDT is an important branch in the NDT area. It has the unique advantage of large area inspection, non-contact, quick inspection and non-radiative testing [114-116]. Previous studies have validated the ability of active thermography in the detection of cracks, delamination and corrosion [40,117,118]. Many materials are inspected using active thermography techniques including metal material [120], fibre [119] and composite material [115, 119]. Section 2.1.3.5 listed the different methodologies of active thermography. Among these active thermography techniques, ECPT is widely used in conductive material testing; it has the advantage of volume heating and rich information of the multi-physics interaction. ECPT is validated to be an effective testing method of surface and sub-surface defect detection in the CFRP [115], wind turbine [24] and railway applications [121].

Active thermography detects defects by recording the thermal image sequences. The defect qualification and quantification are based on the temperature-time response from the thermal image sequences. One thermal image alone is usually insufficient for the decision making of defects. Thus signal processing need to be used before decision making and

quantitative evaluation of the defects. Chen, L. et al. [83] proposed using PCA and ICA for the decision making of defects in CFRP. This work proposed using PCA for dimensional reduction. The orthogonal transform was then used for the pattern-level defect separation.

Bai, L. et al. [84] gave another pattern level feature that used the blind source separation from the transient thermal response. This work was validated using both artificial and natural cracks. The pattern-level features were suitable for qualitative evaluation. However, it is hard to provide a quantitative evaluation of crack characteristics. The pulse excitation in ECPT contains rich frequency information. He, Y. et al. investigated the frequency domain from the transient thermal response [85]. In this approach, the phase and magnitude in the frequency domain are analysed as features for defect characterisation. However, some edges disappear in the phase image, whereas some additional edges appear. In addition, in [85], the testing specimen was in a planar geometry. For a non-planar body, the phase image lacks the information of geometry which brings difficulty in the measurement of defects in a complex geometry body. Jia Liu. et al. [86] gave an optical flow analysis of thermal responses in ECPT and early fatigue contact in gear. A pulse compressed method for ECPT was proposed in [115], which gives the detection of delamination in CFRP. Other features used, including the true positive rate (TPR), false positive rate (FPR), time-phased and thermal gradient, have also been investigated [122]. However, these methods are based on qualitative data where the 3D geometry and real physical thermal gradients are unknown. In addition to these signal processing methods other approaches include the model-based method [123], and artificial intelligence (AI) learning approach [122].

Over all, previous study conducts the experiment using the a 2D IR camera. However, it is hard to achieve quantitative defect evaluation based on 2D thermal data without spatial information about the specimen. Thus, this thesis developed 3D ECPT for the quantitative measurement of the 3D heat flux. The quantitative analysis based on the 3D ECPT is given. The skewness feature and thermal tomographic reconstruction based on the differential time square root of the temperature drop (DTSTD) and TSR are presented in the thesis.

2.4 Three dimensional capture and 3D temperature mapping

Currently, most of the researches and studies on thermography are based on raw images from 2D IR cameras. Because the thermal images are blurred and lack information about geometry, there is a requirement that the thermal image not only be properly captured, but also be ordered, well-calibrated and geo-tagged. In recent years, researchers have explored 3D thermography for different applications both on macro scene and micro scene [124-126]. For 3D thermography on the macro scene, one of the most popular areas is the monitoring of energy distribution on buildings for the detection of thermal leakage. The energy lost in buildings consumes 41% of all the energy production in developed countries [127]. The 3D thermography shows potential for heat insulation inspection with the advantage of quick and large area inspection [128-129]. For applications in micro scene, quantitative NDT shows a high requirement of quantified data. A previous published paper [130] showed the usage of 3D ECPT for the detection of RCF.

2.5 Summary and problems identified

In this chapter, a literature review of thermal IR technology in the NDE area and the 3D reconstruction techniques were reported. Section 2.1 gave a summary of different thermal IR techniques, including flash thermography, ultrasonic thermography, laser thermography and ECPT. To combine thermography with the 3D scanner, up-to-date 3D scanning techniques were reported in section 2.2. Following this, section 2.3 described a quantitative analysis of the ECPT system.

It is apparent from the literature review that the quantitative study of ECPT should stand on a quantified data. Previous research on ECPT gave little or no consideration to the measured data characteristics, for example, the measured temperature data from specific parts of the specimen or the distance between the excitation coils and the measured point. Previous research mainly focussed on defects on planar surfaces [2, 3]. The authors use the set-up of planar specimen defect detection and limited the region of interest (ROI), but the problem of direction emissivity (in which direction the camera receives thermal IR) is still evident because the material has different emissivities at different emitting angles. This results in a temperature measuring error. For an object with a complex geometry, the situation becomes worse because of the following points:

- A more complex heat diffusion in 3D.
- The varying distances from the excitation coil to the different parts of the specimen.
- Projection distortion in 2D imaging.

To overcome the lack of data characteristics, the real physical location is of vital importance for quantitative study. In this thesis, we propose a 3D ECPT system. The next chapter gives a system diagram of the proposed 3D ECPT system with the newly developed registration algorithm.

3 DESIGN AND DEVELOPMENT OF 3D ECPT

This chapter focusses on the first two themes of the aims and objectives—the design of the 3D ECPT system and 3D visualisation, multi-modality imaging fusion and defect detection. The chapter begins with the introduction of the 3D ECPT system set up and camera registration. The IR camera and RGB-D camera are positioned in different coordinate systems. To achieve accurate 3D temperature mapping, the relative position of the cameras (rotation angle and distance from each other) and the camera parameters need to be estimated. This thesis proposes a new camera registration algorithm based on the matched features from the thermal image captured by an IR camera and visible image from an RGB-D camera. Section 3.1.1 gives the hardware structure of the proposed 3D ECPT system. In section 3.1.2, an introduction of current camera registration methods is presented. The proposed feature-based registration algorithm is given in section 3.3.

In section 3.2, two 3D scanners used for 3D capturing are introduced individually. Kinect 3D scanning is introduced in section 3.2.1. To achieve a denser point cloud, multiple scans from Kinect are used and stitched. Section 3.2.2 shows the David structure light 3D scanning system including its set-up and 3D rendering.

Multiple spectrum image fusion is widely used in remote sensing and medical applications because it contains complementary information in different spectrum bands. In the ECPT experiment, multiple spectrum cameras are placed at different viewing angles. The image alignment with proper affine transformation is used to align the images to the same coordinate system. The 3D profiles provided by the 3D rangefinders enable an accurate image alignment of the images taken from different angles. Section 3.3.1 present the developed visualisation software. Section 3.3.2 shows the thermal-visible image 3D fusion and the COMSOL simulation results.

3.1 Design and development of 3D ECPT system and camera registration

This section gives the system set up of the 3D ECPT with camera registration. Figure 3-1 shows the 3D ECPT set-up. The signal generator sends the signal to both the IR camera and the induction heater. The induction heater generates a high-frequency pulsed current to the coil. The eddy current is induced at the conductive material (In Figure 3-1 the testing sample is a rail track head). The heating effect is captured by an IR camera. At the same time, the 3D geometry is captured by the David 3D system.

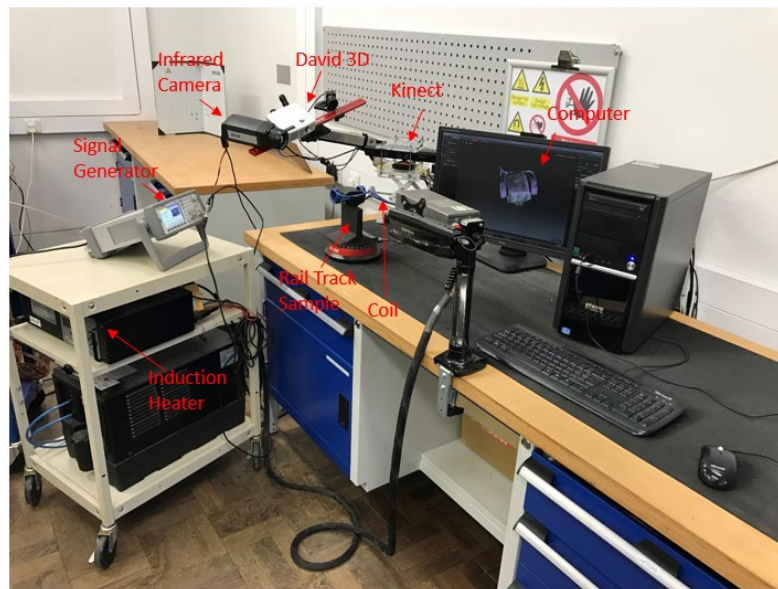


Figure 3-1 Three-dimensional eddy current pulsed thermography system



Figure 3-2 Three-dimensional scanners Kinect and David 3D

Since the 3D ranger and IR camera stand on different viewing angles as shown in Figure 3-2, it is necessary to unify the coordinate system of the 3D camera and the IR camera. This process is termed as *camera calibration*. The calibration of the two camera systems aims to find the intrinsic and extrinsic parameters in order to align the two coordinate systems.

The camera calibration process models the camera system with intrinsic and extrinsic parameters. The cameras were modelled as pin-hole cameras in this research. Using the mathematical model of the camera systems, the objective of camera calibration is to find the camera system's extrinsic and intrinsic parameters.

One of the most popular calibration methods is Tasi's camera calibration method [131-133] because this can deal with planar and non-planar points. First, the Kinect point cloud in the Kinect viewpoint is transferred to the IR camera viewpoint:

$$X_{Infrared} = R_{Infrared}X_{Kinect} + T_{Infrared} \quad (3-1)$$

$$X_{Kinect} = R_{Kinect}X_{Kinect} + T_{Kinect} \quad (3-2)$$

Here, $X_{Infrared}$, and X_{Kinect} are the physical coordinates from the IR camera and Kinect coordinate systems. Moreover, $R_{Infrared}$, and R_{Kinect} are the rotation matrices, whereas $T_{Infrared}$, and T_{Kinect} are the displacement matrices.

$$X_{Infrared} = R_{Infrared}R_{Color}^{-1}X_{Kinect} + T_{Infrared} - R_{Kinect}^{-1}T_{Kinect} \quad (3-3)$$

The transformation between the 3D point cloud and thermal image point is given as

$$\begin{aligned} Z_c \begin{bmatrix} u \\ v \\ 1 \end{bmatrix} &= \begin{bmatrix} \frac{1}{dx} & 0 & u_0 \\ 0 & \frac{1}{dy} & v_0 \\ 0 & 0 & 1 \end{bmatrix} \begin{bmatrix} f & 0 & 0 & 0 \\ 0 & f & 0 & 0 \\ 0 & 0 & 1 & 0 \end{bmatrix} \begin{bmatrix} X_C \\ Y_C \\ Z_C \\ 1 \end{bmatrix} \\ &= \begin{bmatrix} a_x & 0 & u_0 & 0 \\ 0 & a_y & v_0 & 0 \\ 0 & 0 & 1 & 0 \end{bmatrix} \begin{bmatrix} X_C \\ Y_C \\ Z_C \\ 1 \end{bmatrix} \end{aligned} \quad (3-4)$$

where $(u, v, 1)$ is the homogeneous coordinate of the image coordinate system in pixels; $(x, y, z, 1)$ is the homogeneous coordinate of the image coordinate system in centimetres; dx , and dy are the physical lengths for each pixel in the x and y directions respectively; (u_0, v_0) is the centre point of the camera.

From the the above formulas, we can see that if we obtain $R_{Infrared}$, $T_{Infrared}$, R_{Kinect} , T_{Kinect} , $a_{xKinect}$, $a_{yKinect}$, $a_{xInfrared}$, $a_{yInfrared}$, $u_{Infrared}$, $v_{Infrared}$, u_{Color} , and v_{Color} , we can map each thermal point $(u_{thermal}, v_{thermal})$ to the point cloud $(X_{Kinect}, Y_{Kinect}, Z_{Kinect})$

To find the parameters, the mapping from pixel values to the 3D point cloud can be formulated as follows:

$$Z_c \begin{bmatrix} u_i \\ v_i \\ 1 \end{bmatrix} = \begin{bmatrix} \frac{1}{dx} & 0 & u_0 \\ 0 & \frac{1}{dy} & v_0 \\ 0 & 0 & 1 \end{bmatrix} \begin{bmatrix} f & 0 & 0 & 0 \\ 0 & f & 0 & 0 \\ 0 & 0 & 1 & 0 \end{bmatrix} \begin{bmatrix} R & t \\ 0^T & 1 \end{bmatrix} \begin{bmatrix} X_{wi} \\ Y_{wi} \\ Z_{wi} \\ 1 \end{bmatrix} \quad (3-5)$$

$$= Z_c \begin{bmatrix} u_i \\ v_i \\ 1 \end{bmatrix} = \begin{bmatrix} m_{11} & m_{12} & m_{13} & m_{14} \\ m_{21} & m_{22} & m_{23} & m_{24} \\ m_{31} & m_{32} & m_{33} & m_{34} \end{bmatrix} \begin{bmatrix} X_{wi} \\ Y_{wi} \\ Z_{wi} \\ 1 \end{bmatrix} \quad (3-6)$$

The aim is to find the m matrix that maps the 3D point cloud X_{wi}, Y_{wi}, Z_{wi} to IR pixel u_i, v_i .

Expressed a different way, Eq. (3-6) comprises the three following equations:

$$\begin{aligned} Z_c u_i &= m_{11} X_{wi} + m_{12} Y_{wi} + m_{13} Z_{wi} + m_{14} \\ Z_c v_i &= m_{21} X_{wi} + m_{22} Y_{wi} + m_{23} Z_{wi} + m_{24} \\ Z_c &= m_{31} X_{wi} + m_{32} Y_{wi} + m_{33} Z_{wi} + m_{34} \end{aligned} \quad (3-7)$$

Solving Eq. (3-7) we obtain

$$\begin{aligned} m_{11} X_{wi} + m_{12} Y_{wi} + m_{13} Z_{wi} + m_{14} - u_i m_{31} X_{wi} - u_i m_{32} Y_{wi} - u_i m_{33} Z_{wi} &= u_i m_{34} \\ m_{21} X_{wi} + m_{22} Y_{wi} + m_{23} Z_{wi} + m_{24} - v_i m_{31} X_{wi} - v_i m_{32} Y_{wi} - v_i m_{33} Z_{wi} &= v_i m_{34} \end{aligned} \quad (3-8)$$

From this equation, we know that if we have n points' locations, we can solve a 2n linear equation. We can writing the 12 equations in the following matrix:

$$\begin{bmatrix} X_{w1} & Y_{w1} & Z_{w1} & 1 & 0 & 0 & 0 & 0 & -u_1X_{w1} & -u_1Y_{w1} & -u_1Z_{w1} \\ 0 & 0 & 0 & 0 & X_{w1} & Y_{w1} & Z_{w1} & 1 & -v_1X_{w1} & -v_1Y_{w1} & -v_1Z_{w1} \\ \dots & \dots & \dots & \dots & \dots & \dots & \dots & \dots & \dots & \dots & \dots \\ X_{wn} & Y_{wn} & Z_{wn} & 1 & 0 & 0 & 0 & 0 & -u_nX_{wn} & -u_nY_{wn} & -u_nZ_{wn} \\ 0 & 0 & 0 & 0 & X_{wn} & Y_{wn} & Z_{wn} & 0 & -v_nX_{wn} & -v_nY_{wn} & -v_nZ_{wn} \end{bmatrix}$$

$$* \begin{bmatrix} m_{11} \\ m_{12} \\ m_{13} \\ m_{14} \\ m_{21} \\ m_{22} \\ m_{23} \\ m_{24} \\ m_{31} \\ m_{32} \\ m_{33} \end{bmatrix} = \begin{bmatrix} u_1 m_{34} \\ v_1 m_{34} \\ \dots \\ \dots \\ \dots \\ \dots \\ \dots \\ \dots \\ u_n m_{34} \\ v_n m_{34} \end{bmatrix} \quad (3-9)$$

Equation. (3-9) can be written as

$$Km = U \quad (3-10)$$

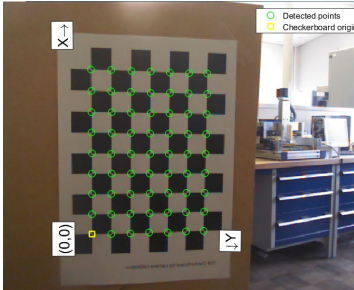
$$m = (K^T K)^{-1} K^T U \quad (3-11)$$

Equation. (3-11) solves the m matrix and the pixels from the 2D IR image correspond to the solved projection matrix m.

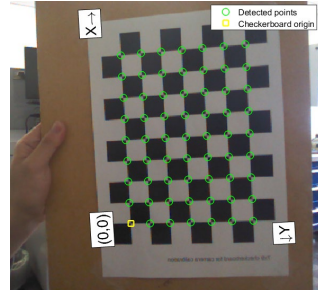
3.1.1 State-of-the-art of camera registration algorithms

Instead of using a 3D calibration board, Zhang [134-136] presented a more convenient method using a planner checkerboard. Compared with Tsai's algorithm, Zhang's method only requires a planner calibration board. However, it also requires several shots from different positions.

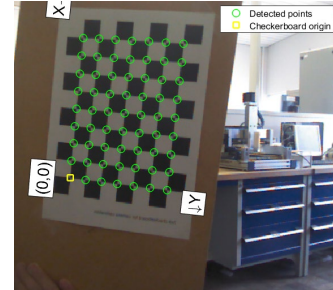
MATLAB provides a toolbox for Zhang's algorithm. With previous knowledge of checkerboard block size, this method detects the intersection of checkerboard blocks and calculates intrinsic and extrinsic parameters.



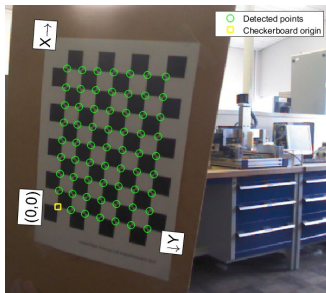
(a)



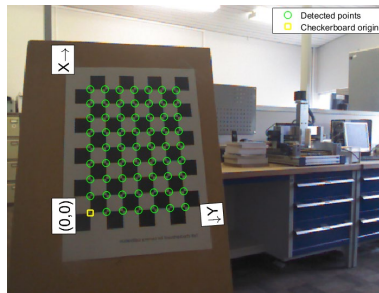
(b)



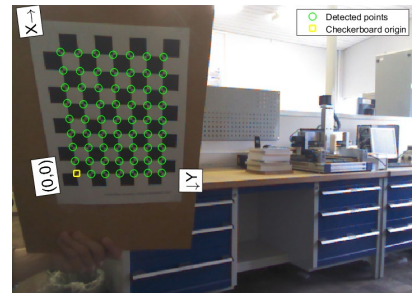
(c)



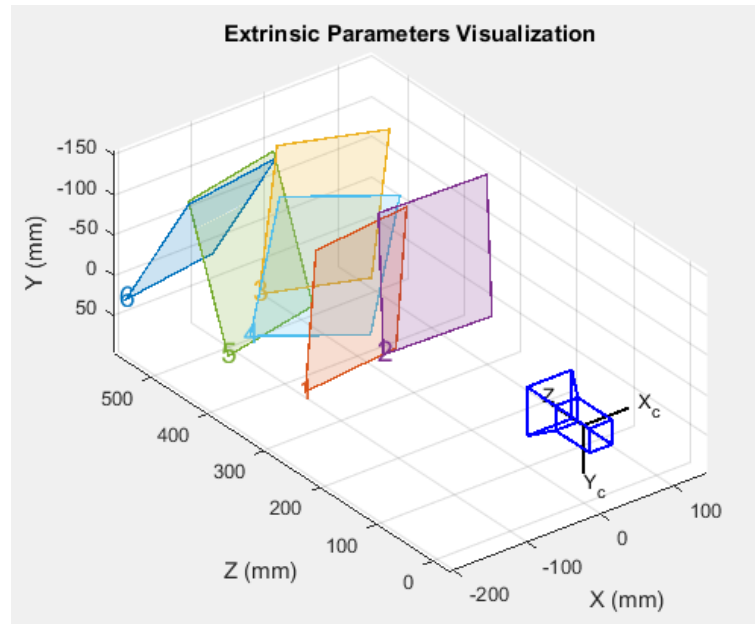
(d)



(e)



(f)



(g)

Figure 3-3 Camera calibration using checker board

Figures. 3-3 (a-f) show the result of color camera calibration from multiple views. The features are first extracted. Then, the extrinsic parameters (rotation and translation) are visualised in Figure. 3-3(g).

However, the standard method cannot be applied to a thermal camera because the thermal camera cannot detect checkerboard patterns from a standard checkerboard.

Until now, checkerboard detection has always been a popular topic in computer vision. The most popular one is Zhang Zhengyou's method [134]. This method has the advantage that it only needs a planner calibration board. The intrinsic parameters and extrinsic parameters are estimated with high precision by moving the camera in a different poses towards the planner checker board. Reference [137] proposed a subpixel checkerboard detection algorithm by using a pre-defined corner prototype. This work can detect checkerboard patterns at the subpixel level. Other methods [138] uses Hough transform and Harris corners to locate and detect checkerboard patterns.

From the algorithms listed above, none so far can be implemented on thermal images. This work uses a new registration algorithm based on the proposed shape-constrained Scale Invariant Feature Transform (SIFT) feature detector and descriptor.

3.1.2 Proposed feature-based IR-RGB-D camera registration algorithm

3.1.2.1 *Background of feature based registration*

In this work, an image feature based calibration method is used. The visible camera registration technology is supported by robust feature extraction and description techniques such as SIFT [139, 140]. H. Bay improved the SIFT algorithm and speed up feature detection and description with the Speed Up Robust Feature (SURF) [141]. Later, A. Alahi proposed the Fast Retina Keypoint (FREAK) algorithm [1]. However, whereas all these descriptors work

well for visible spectrum images, they fail for multi-spectrum images because the descriptors use local information around extracted features and the multi-spectrum images are quite different in terms of their local information. Recently, researchers have begun to solve this issue by using global information. Shan-e-Ahmed Raza et al. [142] proposed using contour of multi-spectrum images extracted with wavelet transform. Y Gu et al [143] proposed using a shape matching algorithm with polynomial fitting. However, these algorithms still do not have enough robustness if only contour information is used. The performance of the matching becomes bad when they have too much difference in their edges.

In real practice, visible images have more contour information compared with thermal images because the thermal images are usually blurred. Yong Li et al. [144] proposed establishing key-point matches on multispectral images utilising descriptors with global information over entire image. The work has achieved good and robust matching results. However, this approach still needs prior knowledge, including the field of view constraint and the spatial constraint. C. Aguilera et al [145] proposed a SIFT-Like-Based approach for the Far Infrared-visual (FIR-VS) registration. The work modified the SIFT descriptor by histograms of the contours in the neighborhood of the given key-points instead of using neighborhood gradient information. However, this approach still depends on the performance of edge extraction. Over all, the feature matching from multi-spectrum images remain a challenge.

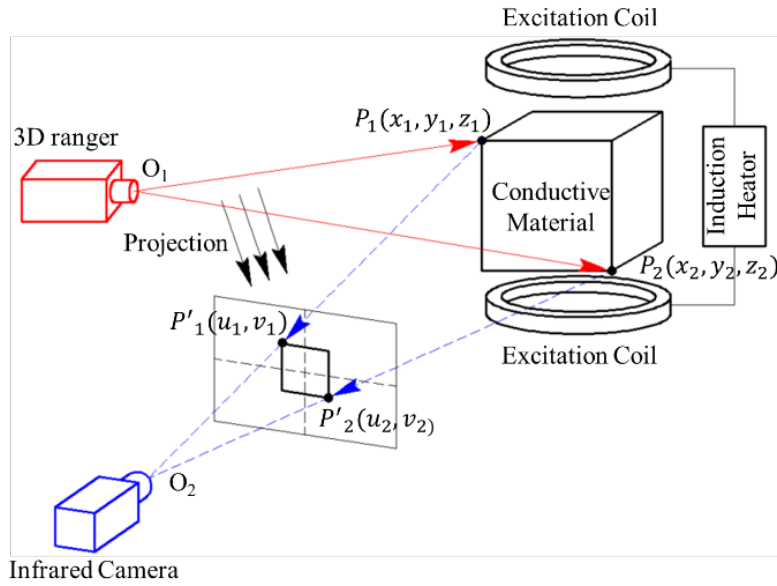


Figure 3-4 The system diagram of 3D ECPT

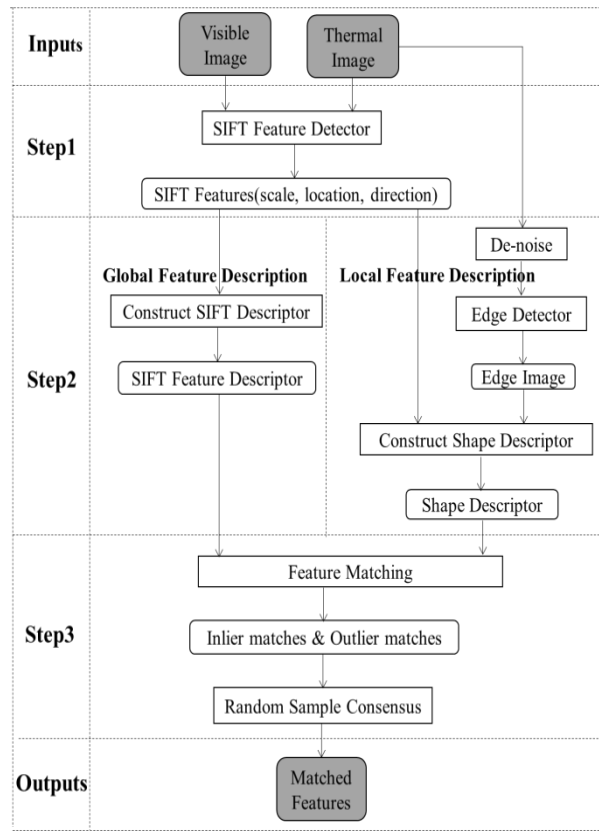


Figure 3-5 Overview of the proposed feature matching algorithm

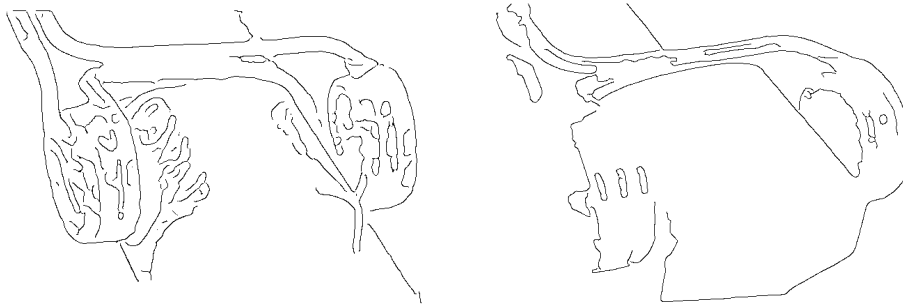
To give reliable feature matching for the registration of the 3D ECPT system, a robust descriptor for the thermal image and the visible image feature is desired. This section gives a newly developed descriptor for the thermal-visible image feature matching. The SCSIFT is proposed. The descriptor combines both local information and global information with a proper weighting. The combined descriptor automatically gives global information with the extracted contour information, whereas the dependency of the edge extraction result is reduced with the local descriptor.

3.1.2.2 Methodology of the proposed features and image registration

The registration from the thermal image to the RGB-D image is achieved by a projection matrix. The projection matrix is calculated by finding the matched features from the thermal image and the RGB-D image. According to the least square principle, it requires at least six matched feature points to solve the 12 unknown elements of the projection matrix [131]. The sketch diagram is shown in Figure 3-4, where O_1 is the optical centre of the RGB-D camera and O_2 is the optical centre of the IR camera. The point cloud obtained from the RGB-D camera $P_1(x, y, z)$ is projected to the infrared camera plane with the pixel noted as $P'_1(u_1, v_1)$. O_1 and O_2 are the optical centres of the RGB-D camera and IR camera respectively. Each point from point cloud $P_1(x, y, z)$ is projected to the IR plane as $P'_1(u_1, v_1)$. The pixel $P'_1(u_1, v_1)$ is the crossing point of the line O_2P_1 with the IR camera plane. The mathematical camera model above is called a pin-hole camera model [134]. The corresponding transformation of a point cloud $P_1(x, y, z)$ to the pixel location $P'_1(u_1, v_1)$ is obtained from the projection matrix [135].

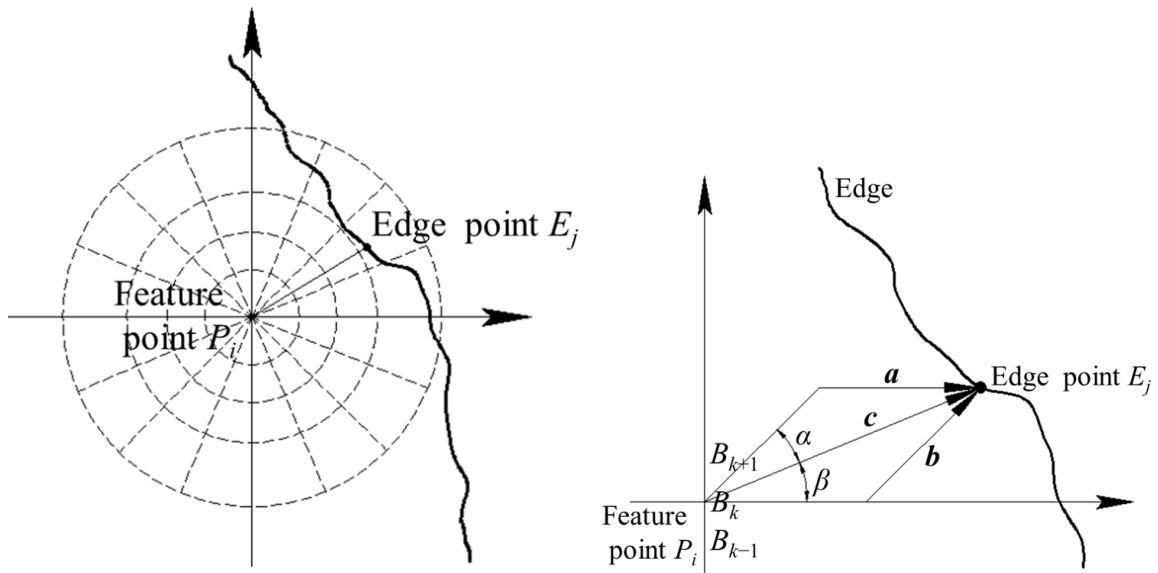
In conclusion, to give the correspondence relationship from the point cloud to IR pixels, the projection matrix needs to be found, which requires at least six matched features from the RGB-D image and the thermal IR image. Thus, the reliable matched features are desired. The

next section gives the proposed SCSIFT descriptor used for the feature matching between IR camera and RGB-D camera. The diagram of the proposed SCSIFT is sketched in Figure 3-5.



(a) Contour of the thermal image (b) Contour of the visible image.

Figure 3-6 Edge extraction of thermal image and visible image.



(a) Circular template histogram (b) Vector decomposition.

Figure 3-7 Construction of the shape descriptor

This section gives the details of the proposed SCSIFT descriptor. The proposed descriptor can generally be divided into three steps: feature extraction, feature descriptor construction and feature matching.

1) Step one: feature extraction

The work uses the SIFT detector [139] for feature extraction. The SIFT operator is used in both the visible image from the RGB-D camera and the thermal image from the thermal camera. The SIFT feature contains not only the location but also the scales and directions information.

2) Step two: feature descriptor construction

This step gives the procedures for constructing the SCSIFT descriptor. The proposed SCSIFT descriptor contains both local and global information. For the local information, the SIFT descriptor is used and applied in both the thermal image and the visible image. For the global constraint, the thermal image is de-noised first with anisotropic diffusion [148], after which the Canny operator [149] is used for the edge extraction in both the visible image and the de-noised thermal image. The shape descriptor is constructed with both the local descriptor and the thermal descriptor.

3) Step three: feature matching

Feature matching is based on the description of the features. Each feature descriptor is a vector consisting of a local feature descriptor and a global feature descriptor. The matched features are those with the minimum distance of their feature descriptor vectors. However, considering that the shape descriptor and the local SIFT descriptor are the different descriptions of information, they are different in both scales and data structures. Before combining the local descriptor and the global shape descriptor, the two descriptor vectors need to be normalized before being grouped into one descriptor vector. Finally, the grouped descriptors with minimum vector distance suggest a possible match. In the end, to remove wrong matches, the random sample consensus (RANSAC) was used [150].

The detailed steps and explanations are given in the next part. Table 3 shows the notations used in the algorithm. Step one completes SIFT feature extraction from the thermal image and the visible image. Step two completes the construction of the SCSIFT descriptor. In the end, the feature matching, including the normalization and combination of the global shape descriptor and local SIFT descriptor, are given.

Symbol	Description
P_i	current feature point
E_j	current edge point
W	weighting of feature P_i
b	number of bins in the circular template
B_k	value of features (with weighting function) for the k^{th} bin.
α	angle between line P_iE_j and upper line of bin B_k
β	angle between line P_iE_j and lower line of bin B_k
φ	angle of each bins interval
$d_{S(L)}^i$	local descriptor for feature i in source image
$d_{S(G)}^i$	global descriptor for feature i in source image
$D_{ref(L)}^{all}$	local descriptor set for all features in reference image
$D_{ref(G)}^{all}$	global descriptor set for all features in reference image
E_G^i	The distance set for $d_{S(G)}^i$ to $D_{ref(L)}^{all}$
E_L^i	The distance set for $d_{S(L)}^i$ to $D_{ref(L)}^{all}$
S^i	Scaling factor of E_L^i and E_G^i

Table 3 Symbol of notations for the proposed feature matching algorithm

a) Global shape constraints and feature descriptions

Since SIFT feature descriptors are not sufficient for the registration of the different modality images, global features for capturing image contexts are required in addition to local SIFT features. Before the edge extraction, de-noising of the thermal image should be performed. In practice, the thermal image is blurred and lacks edge information. In this work, anisotropic diffusion [123] is used, which shows a good balance between noise reduction and edge preservation for the thermal image. After filtering, the Canny edge operator [124] is selected for the edge extraction of both the smoothed thermal image and the visible image. The extracted edge images are shown in Figure 3-6. From the two images, it can be found that there also exist much difference in the thermal image contour and the visible image contour. The result also indicates that it is not practical only to use contours for registering of the thermal image and the RGB-D image.

As mentioned previously, the shape descriptors are based on the contours of the images. After thermal image smoothing and edge extraction, the next step is to construct the shape feature descriptors. The sketch of the construction of the shape descriptor is shown in Figure 3-7. In the figure, the symbol P denotes the feature point. During the procedure of the SIFT feature

extraction, the rotation angle of γ is also calculated which is the dominant gradient direction for each feature point P_i ($i \in \mathbb{N}^+$). To make the feature description and feature matching invariant to the camera rotation. The local area is rotated with γ angle.

The shape descriptor was constructed via the edge image and the circular template for counting the surrounding edge pixels. The sketch of the circular template is given in Figure. 3-7 (a). For each feature point, a circular template is generated that separates the surrounding area into 16 bins (16 directions). Each other edge pixel is decomposed to the surrounding bins (directions). The decomposed weighting value W is given in Eq. (3-12) and Eq. (3-13) and shown in Figure 3-7 (b):

$$\Delta B_{k+1} = \frac{W \sin(\alpha)}{\sin(\varphi)} \quad (3-12)$$

$$\Delta B_k = \frac{W \sin(\beta)}{\sin(\varphi)} \quad (3-13)$$

In the equation, $\varphi = 2\pi/16$, which is the angle of each bins; W denotes the direction decomposition weighting; and α and β are the upper angle and lower angle which are the angle between line $P_i E_j$ and upper line of bin B_k , and the angle between line $P_i E_j$ and the lower line of bin B_k .

For the counting of the edge pixels surrounding the extracted feature, a proper weighting should be given where the far region edge pixels are suppressed or even ignored and the near region edge pixels have a larger weighting which means that the close region pixel has a larger impact on the global descriptors. In this work, the relationship between weighting and distance is decided by the spiral of Theodorus [146,147]. The mathematical expression is given in Eq. (3-14):

$$W = \arcsin\left(\frac{1}{\sqrt{d}}\right) \quad (3-14)$$

In the formula above, W is the calculated weighting of each pixels, and d is the distance from the extracted feature point to the edge pixel. Figure 3-8 shows the spiral and the relationship between the weighting and the distance. In the figure, the distance d is the d_{th} point in the curve. The angle between the d_{th} point and $(d-1)_{th}$ point forms the weighting function.

Mathematically, the angle of two successive square number points, for example, the 16th point and 25th point is striving to reach $360^\circ/\pi$.

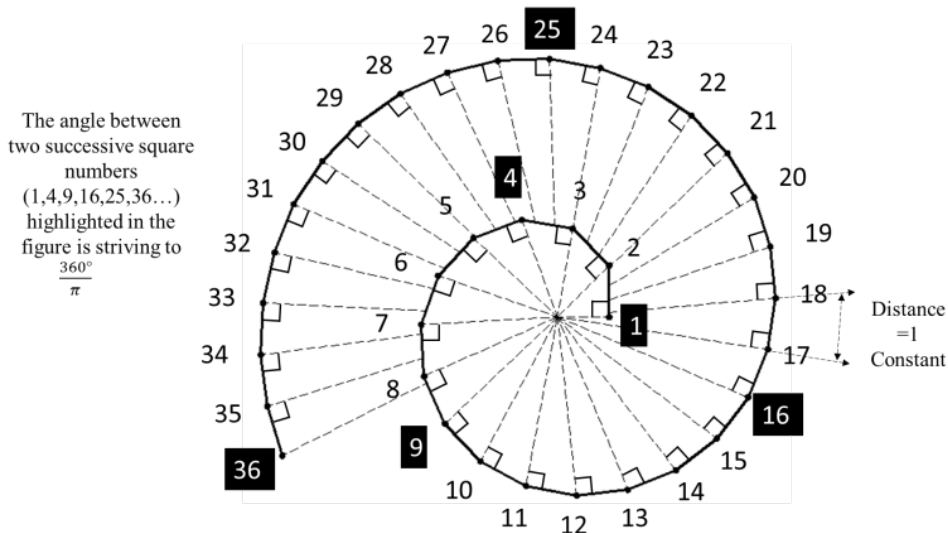


Figure 3-8 Weight for different distance

The new global descriptor describes the surrounding edges of the feature point. From humans' perception, humans can easily identify and match the feature points of two modalities of images (e.g. thermal and visible). Humans identify the object mainly based on the shape and global information, rather than the detailed local pixels. By combining the global descriptor with the SIFT descriptor, it is possible for the machine to match the two images with different image formations.

b) Global and local feature descriptor normalization and feature matching

The previous part discussed the procedure of constructing the shape descriptor. In this section, feature matching and descriptor normalization are presented. The global descriptor describes the counting of edge pixels surrounding the feature point, whereas the local features are the magnitude and gradient. Since they are two different mathematical descriptions, they need to be normalized before being combined as the SCSIFT descriptor vector. For the global and local descriptor vector normalization, the normalization weighting value is calculated using the minimum vector distance, which is obtained during the process of calculating the distance of descriptors. In this work, the reference image is the RGB image obtained from the RGB-D camera and the source image is the thermal image. During the process of normalization,

the feature point i in the source image is denoted as f_S^i with the descriptor denoted as d_S^i , the distance of global descriptor $d_{S(G)}^i$ and local descriptor $d_{S(L)}^i$ to all global and local features descriptors $D_{ref(G)}^{all}$ and $D_{ref(L)}^{all}$ in reference image are calculated respectively, denoted as set E_G^i and set E_L^i shown in Eqs.(3-15) and (3-16):

$$E_G^i = \sqrt{(D_{ref(G)}^{all} - d_{S(G)}^i)^2} \quad (3-15)$$

$$E_L^i = \sqrt{(D_{ref(L)}^{all} - d_{S(L)}^i)^2} \quad (3-16)$$

The scaling factor S^i is the ratio of maximum value of sets E_G^i and E_L^i shown in Eq.(3-17). Since the Euclidean distance calculations for descriptors are inherently in the process of feature matching, it will not increase the computing complexity.

$$S^i = \frac{\max(E_L^i)}{\max(E_G^i)} \quad (3-17)$$

Finally, the unification process is expressed as follows:

$$E^i = E_G^i \cup \frac{E_L^i}{S^i} \quad (3-18)$$

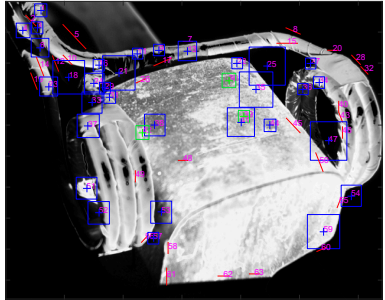
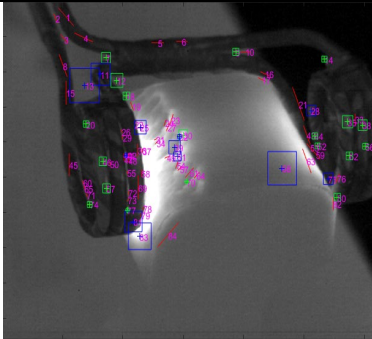
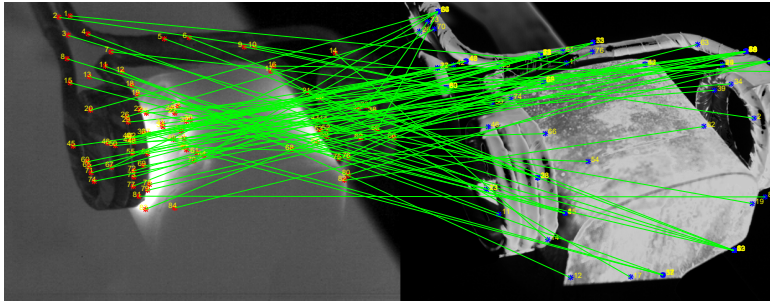
where E^i is the unified distance set for f_S^i to all features in the reference image. The minimum value in set E^i indicates the best possible match. In this way, for each feature, an appropriate scaling value can be dynamically calculated according to the maximum global distance and maximum local distance.

After the descriptor normalization, the global descriptor and local descriptor are combined into one descriptor. Finally, RANSAC is used to remove possible wrong matches [150].

3.1.2.3 Experimental study of the proposed registration method

In this part, an experimental study is conducted using one rail track sample with natural cracks caused by the RCF. A sample with artificial cracks was also investigated for comparison study.

For the RCF cracks, a Helmholtz coil is used as an excitation coil since it can generate a nearly uniform magnetic field in the rail track sample. The excitation coil is cooled by water. The heating time is 200ms. The excitation current is 260kHz and 300A. The work follows the procedures introduced in the previous part. First, this part compares and analyses the differences and features extracted from the visible and thermal image. Then, a comparison is made between the proposed SCSIFT feature matching and the original SIFT feature matching. Finally, the 3D fusion result is presented.

Process	Description	Output															
SIFT feature detector	Feature vector <table border="1" data-bbox="391 835 526 1031"> <tr><td>x location</td></tr> <tr><td>y location</td></tr> <tr><td>scale</td></tr> <tr><td>edge flag</td></tr> <tr><td>orientation</td></tr> </table>	x location	y location	scale	edge flag	orientation	 <p>(a) Visible image SIFT features</p>	 <p>(b) Thermal image SIFT features</p>									
x location																	
y location																	
scale																	
edge flag																	
orientation																	
Feature descriptor	Feature descriptor <table border="1" data-bbox="399 1245 537 1724"> <tr><td>local SIFT descriptor</td></tr> <tr><td>⋮</td></tr> <tr><td>orientation</td></tr> <tr><td>⋮</td></tr> <tr><td>128</td></tr> <tr><td>⋮</td></tr> <tr><td>local SIFT descriptor</td></tr> <tr><td>shape descriptor</td></tr> <tr><td>⋮</td></tr> <tr><td>orientation</td></tr> <tr><td>⋮</td></tr> <tr><td>16</td></tr> <tr><td>⋮</td></tr> <tr><td>shape descriptor</td></tr> </table>	local SIFT descriptor	⋮	orientation	⋮	128	⋮	local SIFT descriptor	shape descriptor	⋮	orientation	⋮	16	⋮	shape descriptor	 <p>(c) Original SIFT-based matching</p>	
local SIFT descriptor																	
⋮																	
orientation																	
⋮																	
128																	
⋮																	
local SIFT descriptor																	
shape descriptor																	
⋮																	
orientation																	
⋮																	
16																	
⋮																	
shape descriptor																	

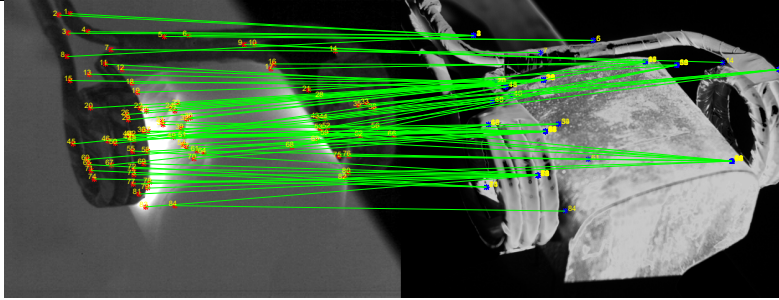
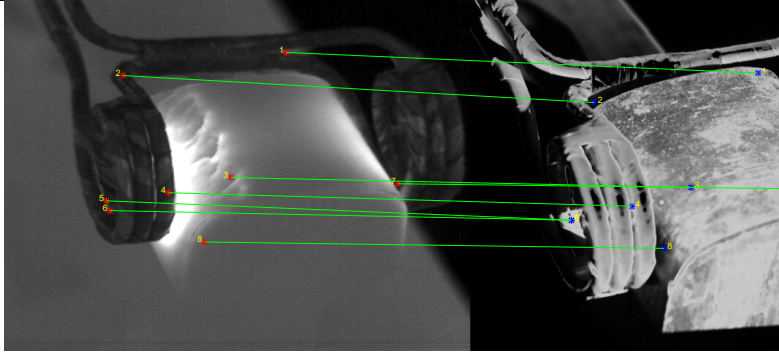
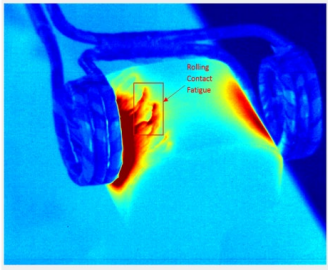
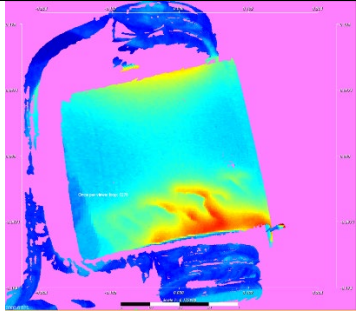
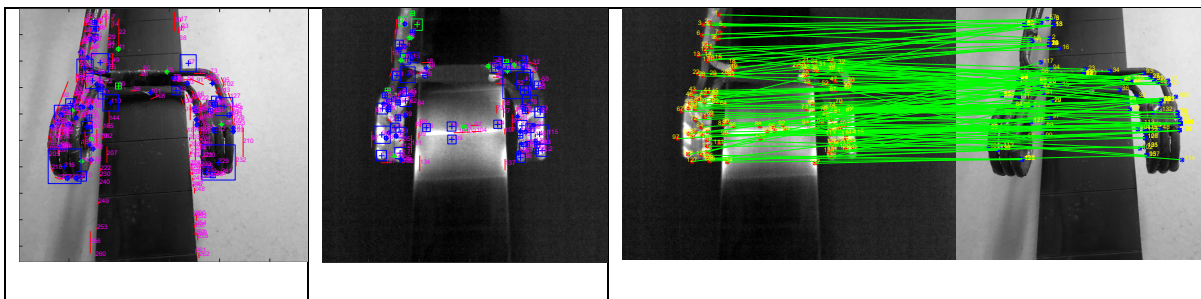
			
		(d) Proposed SCSIFT-based matching	
Random Sample Consensus	[150]		
		(e) Image registration after RANSAC	
2D & 3D fusion	Ref. Eq. (3-9)		
		(f) 2D thermal image	(g) 3D fusion image

Figure 3-9 Rail track feature matching and fusion



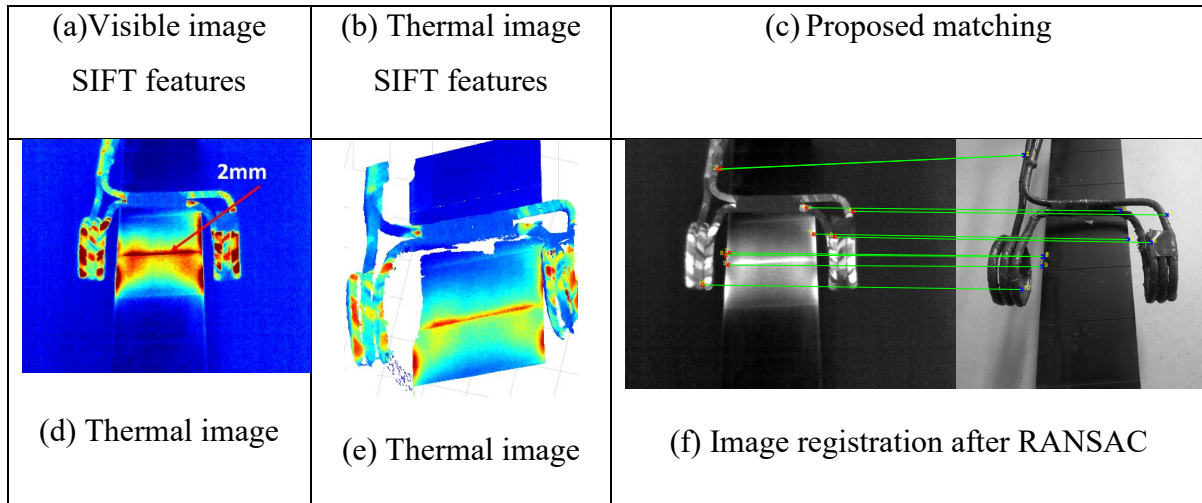


Figure 3-10 Feature matching and fusion of man-made sample

The raw data are shown in Figure 3-9 (a) as the visible image of the natural crack sample and Figure 3-9 (b) as the thermal image. The SIFT features and thermal image SIFT features for the rail track are also marked in the image. From the two images, the thermal image clearly shows RCF. However, the thermal image lacks the texture information. In addition, the edge area is blurred in the thermal image. In contrast, the visible image complements the drawback of the thermal image. The visible image does not have enough crack information, but provides a clear view of edges and texture information. Thus, it is desired to combine thermal images and visible images or RGB-D images together. From Figures. 3-9 (a) and (b), the red lines are features on the edges. The box features are the features that are not in the edge. The colour of the box indicates the quality of the extracted features. The blue boxes indicate possible good features, while the green boxes are the features with low quality. The feature scale is also marked as the scale of the boxes. In the ECPT system, the coils used for eddy current excitation are apparent features, that can be used as markers for image registration. From Figures 3-9 (a) and (b), it can be seen that most of the features lie on the two coil sides. Furthermore, the coils lie in the same plane as the rail track surface, which helps to point out the major ground truth plane. This will contribute to pointing out the ROI and decreasing the 2D fusion error.

The feature descriptor is built based on the discussion in the previous part. Comparing the thermal image with the visible image, the local area information has extensive difference, leading to a failure in SIFT feature matching (see Figure 3-9 (c)). However, by adding global

shape information, the features are correctly matched, as shown in Figure 3-9 (d) with the proposed SCSIFT descriptor. Finally, Figure 3-9 (e) is the registration of the two modality images after RANSAC and 3D temperature mapping is accomplished using detected matched features shown in Figures 3-9 (g).

For a comparison study and a better evaluation of the fusion between crack and 3D heat flow, a man-made sample with angular slots is tested. Figures 3-10 (a) and (b) show man-made crack samples in visible images and thermal images with SIFT features. Figure 3-10 (c) shows the proposed feature matching. Figure 3-10 (f) shows the feature matching after RANSAC. Figure 3-10 (d) shows the original thermal image. Finally, the 3D fusion of a man-made crack is shown in Figure 3-10 (e). The man-made slot is 2mm deep with a slant angle of 45°. The thermal image used was taken at 200ms after the signal generator sends signal. The heating time is 200ms, and the excitation current is 300A and 260 kHz. In a comparison of the proposed registration and fusion for man-made and natural samples as illustrated in the Figures 3-9 and 3-10, natural samples have more robust matched feature points, which is important for real-world applications.

3.2 Kinect fusion and David 3D scanning

In this work, two 3D rangers of the Kinect SL camera and David 3D camera were chosen. This section presents the investigation on 3D scanning including their working principles, limitations through comparison and 3D fusion technologies for 3D ECPT systems.

3.2.1 Kinect SL ranger and its features for fusion

The Kinect SL sensor is a low-cost 3D ranger that has a wide-ranging field of view of 43° (vertical) × 57° (horizontal). The sensor captures 30 frames per second. The component structure of Kinect is shown in Figure 3-11. It consists of a near-IR emitter, near-IR camera and RGB camera. The near IR emitter and near-IR camera are used for depth measurement.

The Kinect one uses structure light projection which is an active stereo vision technique for depth estimation. The IR emitter projects random IR patterns, as shown in Figure 3-12 (a-d). These images were taken with the near-IR camera. Figure 3-12(a) shows the near-IR patterns. Figure 3-12 (b-d) shows the near-IR patterns in medium distance, close distance and far distance. The images were captured in the near mode.

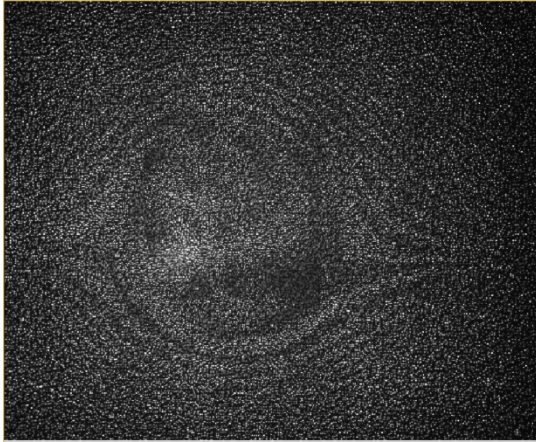
There are several issues that can be raised from Figures 3-12 (a-d). First, there appear many holes among the IR patterns. This is either caused by the IR emitter, which cannot light that area at some specific angle, or the infrared beams that cannot reflect back at the shiny surface area or edged area. Second, the Kinect has a limited sensor range. There are two modes for Kinect sensors—near mode and normal mode. The normal mode has a range of 0.8 meters to 4 m and the near mode are in the range of 0.4 m to 3 m. The near mode is used in this study.

Because the Kinect scanner has a very low spatial resolution for 3D scanning, it can hardly meet the requirements for quantitative NDT. To increase the spatial resolution, Kinect fusion technology is used which merges several scans into one scan. The Kinect fusion process data via Direct X 11 is compatible with GPU and C++ AMP. The modern GPU makes it fluently processed in real-time 3D reconstruction and point cloud stitching.

The Kinect fusion technology generally consists of the steps outlined below.



Figure 3-11 Structure of Kinect 3D scanner



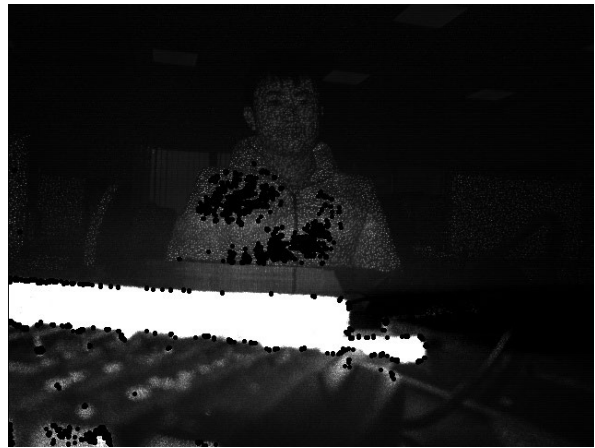
(a) Kinect infrared pattern (structure light)



(b) Infrared patterns on mid-distance



(c) Infrared patterns on close distance



(d) Infrared patterns on far distance

Figure 3-12 Kinect infrared patterns

The first stage is the conversion from raw depth data acquired from the Kinect sensor to the floating point depth in meters. After the data conversion, the surface normal vectors are calculated as the pre-processing of the next step. In addition, the de-noising process is conducted with a proper filter.

The second stage uses the iterative closest point to track the camera movement and align the neighbourhood frames of the point clouds. The general idea of Iterative closest point (ICP) is to iteratively merge two point clouds in a greedy algorithm manor. The essential steps of ICP are as follows:

- 1) For each point in the source point cloud (the previous frame point cloud), match the closest point in the reference point cloud (the current frame point cloud).

- 2) Estimate the rotation and translation matrix using a root mean square point to point distance metric minimization technique.
- 3) Using the estimated transfer matrix, rotate and translate the source point cloud
- 4) Iterate the above steps

Figure 3-13 shows the merging of two surfaces using the ICP algorithm.

The red surface is the original point cloud generated by:

$$z = \sin(x * y), -2 < x < 2; -2 < y < 2 \quad (3-19)$$

The blue surface is the transformed point cloud with a translation of:

$$T = [0.5, \quad -0.3, \quad 0.2]$$

and rotation of:

$$R = [0.3, \quad -0.2, \quad 0.05] \quad (\text{rad.})$$

From the ICP result of Figure 3-13 it can be seen that the red surface is successfully registered to the blue surface. Kinect fusion uses the ICP when each new frame is captured and calculates the translation and rotation. The third stage is merging several point clouds into one point cloud. This procedure is repeated for each new frame captured by the depth ranger. The holes are filled in when moving the 3D rangers to different positions and viewing angles. Figure 3-14 shows Kinect scan and fusion with a thermal IR camera.

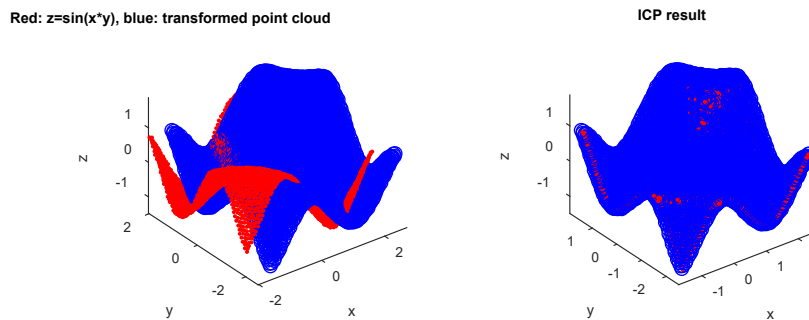


Figure 3-13 Iterative closest points algorithm



Figure 3-14 Kinect visible-thermal fusion

3.2.2 David 3D systems and their features for fusion

The David 3D scanning system consists of a visible projector and a high resolution visible camera. Unlike the Kinect system which has a fixed projector-camera distance, the David 3D has an adjustable camera-to-projector distance and adjustable camera rotation angle α . Thus, before each 3D scanning, a calibration process must be taken with a calibration board.



Figure 3-15 David 3D scanning system

3.2.3 Experimental set-up and samples

The David 3D scanner system uses a visible projector for pattern rendering and a high-resolution RGB camera for depth estimation of the captured patterns. The projector and RGB camera were mounted on a rail. The projector position and camera position on the rail are adjustable. In addition, the camera angle is adjustable in the range of $0^{\circ} - 30^{\circ}$. To acquire the best quality of 3D scanning, the ROI is optimized by properly adjusting the angle of the camera and projector–camera distance.

To obtain the best ROI, the focus of the projector and camera needs to be adjusted. Furthermore, the system has to be recalibrated each time the camera (projector) position or rotation angle is changed. To achieve the best scan, the white balance also needs to be properly adjusted. The white balance is affected by the testing object reflectivity (shiny or rough surface)

and the background light. The white balance can be adjusted by controlling either the projector brightness or the aperture of the RGB camera.

The first step is to obtain the best ROI. This is done by putting the testing sample in front of the 3D scanner and adjusting the projector and the RGB camera until it reaches the maximum overlapped area. To obtain a good quality 3D scanning, it is suggested that the camera rotation angle should be not less than 22° because of triangulation principles.

The second step is to use the calibration board for calibration and adjust the white balance. The software automatically calibrates the system with an accurate estimation of its intrinsic and extrinsic parameters. The white balance is adjusted manually by either controlling the projector or the RGB camera.

The final step of 3D scanning is merging scans of the point clouds. The system enables multiple scans and uses the iterative closest point for point cloud merging. The testing sample is rotated either manually or using a turning table. To obtain the best quality of 3D reconstruction, it is suggested to have at least 16 scans for 360° scanning.

3.3 3D Visualization of thermal point cloud flow and fusion

This section gives visualization of the 3D thermal flow. First, the 3D heat flow software platform is shown in section 3.3.1. Second, the post-processing procedure, including thermal-visible 3D fusion and COMSOL simulation, is described in section 3.3.2.

3.3.1 The three-dimensional visualization software platform

The obtained 3D thermal flow with time is a four-dimensional (4D) matrix that contains the 3D heat flow in different time slots. Thus, the software should provide 3D visualization in not only space but also the temperature response over time. Figure 3-16 shows the 3D visualization software platform.

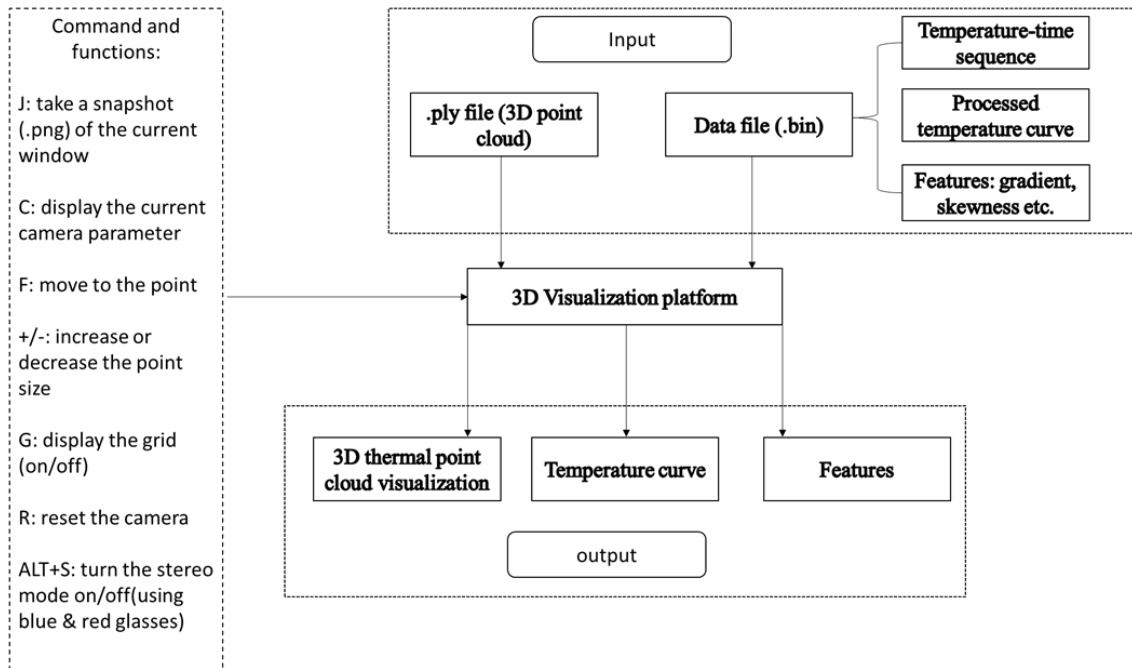


Figure 3-17 Program structure of 3D visualization platform

The program structure of the visualization platform is shown in Figure 3-17. There are two inputs to the visualization platform—the point cloud file and the data file. The platform currently only supports .ply file format for the input of the 3D point cloud. The point cloud acquired from the Kinect 3D ranger or David 3D ranger must be formatted to .ply first. Other information such as the temperature-time sequence, and features are saved in the binary data file. The binary file format is defined by the thesis author and given in the Appendix.

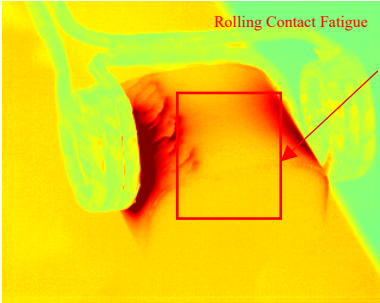
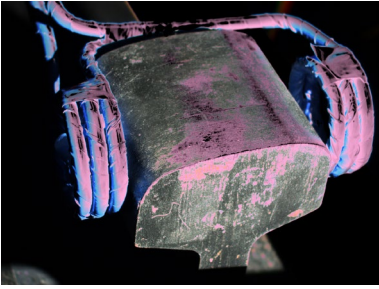
There are several command and functions of the visualization platform. The command is simply keying the following keywords:

- **Keywords: J/j.** This command takes a snapshot of the cloudviewer window. The snapshot is saved as .png image file.
- **Keywords: C/c.** This command displays the camera parameter. The command is used to see the rotation and displacement of the operation to the point cloud.
- **Keywords: F/f.** This command is used to move the camera forward (zooming in) to the position of the mouse.
- **Keywords: +/-.** This command is used to increase (+) or decrease (-) the size of the point cloud.

- Keywords: G. This command enables or disables the grid information. The grid is used to display the ruler of sizing with units of length (cm, mm, etc.).
- Keywords: R. This command resets the camera to the original status.
- Keywords: ALT+s. This command switches between normal mode and stereo vision mode. The stereo vision mode is the anaglyph 3D, which shows the 3D effect to your eye by adding a pair of red blue glasses.

3.3.2 Crack localization, sizing and thermal visible fusion

In this section, one railway sample with an RCF is used for the case study. The rolling contact fatigue is the most common defect for rail track inspection. The RCF is a multiple-crack defect with a direction of 30° – 45° towards the rail track radial direction (the direction in which the train moves). Eddy current testing is an efficient method for RCF inspection [121]; RCF is clearly shown in the active thermal image using ECPT in Figure 3-18 (a), whereas it cannot be seen in the visible image as Figure 3-18 (b).

Process	Outputs	
ECPT thermal image and 2D RGB image	 <p data-bbox="459 1507 764 1539">(a) 2D Infrared thermal</p>	 <p data-bbox="846 1499 1305 1535">(b) Infrared thermal 3D point cloud</p>

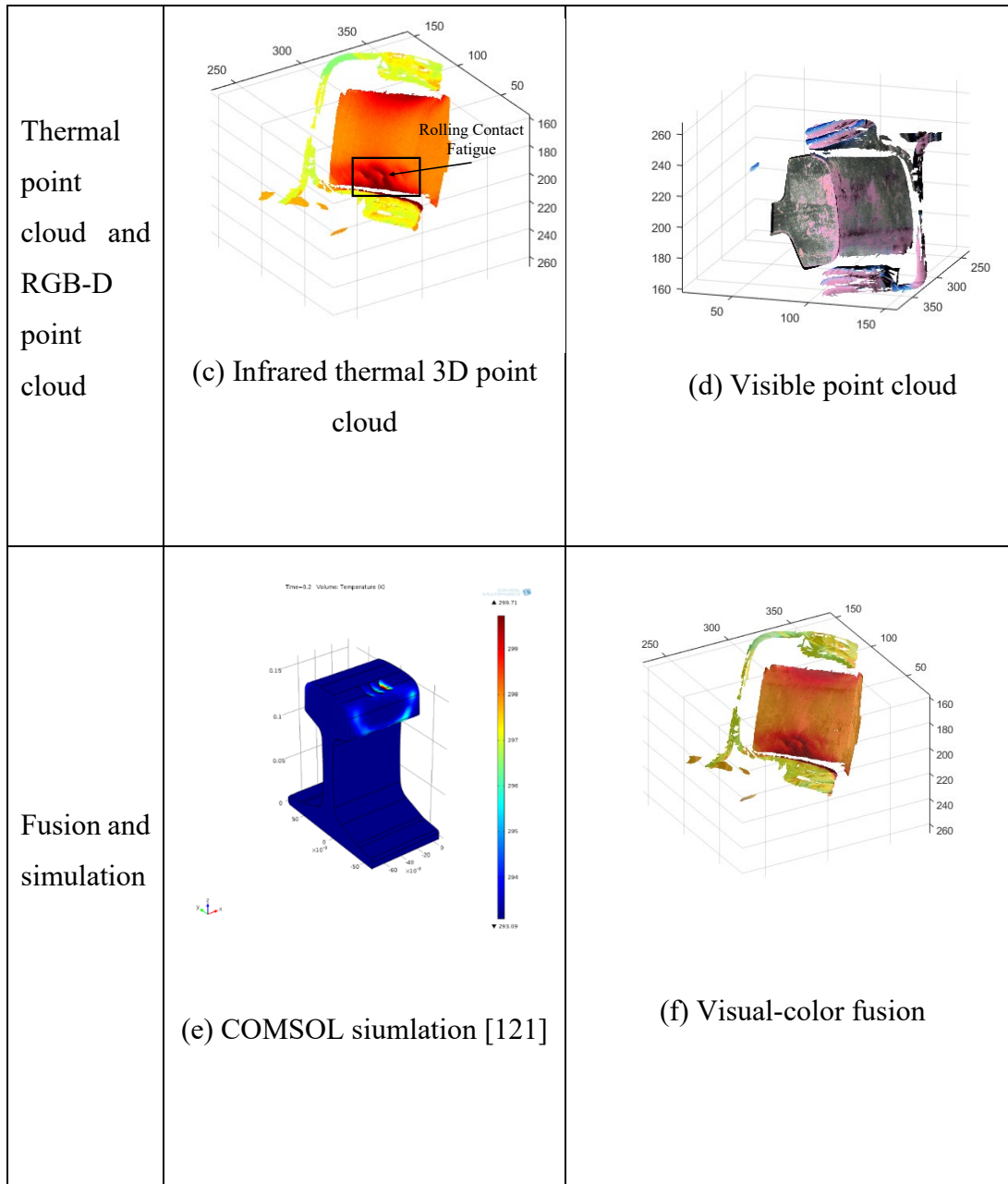


Figure 3-18 Three-dimensional reconstruction, visible and thermal fusion and simulation

Figures. 3-18 (c) and 3-18 (d). 7 show the 3D reconstruction results. The procedure follows the steps illustrated in section 3.1.2. The feature points are extracted in both Figure. 3-18 (a) and (b) and are matched with SCSIFT. The projection matrix is obtained by using the matched feature points. After this, the texture image sequences (thermal heat flow and optical flow) are mapped onto the point cloud. Figure 3-18 (a) is the thermal image taken at 30ms after the pulse generator sends the start signal to the induction heater. Comparing Figure. 3-18 (a) and Figure 3-18 (c), it can also be seen that the 2D thermal IR image is blurred and lack

geometric information. The boundary area is not clear which is a common problem for thermography. When the 3D physical coordinate is added, it can be seen that the edges are now clearly shown. Furthermore, not only can the defect be detected, but it can also be quantified. The heat flow mapped to the point cloud enables the tracking of heat flows in a quantitative manner, where the heat distribution and spreading speed can be calculated with geometry information provided by the point cloud. This enables a better analysis and understanding of the multi-physical phenomenon of the ECPT system.

Another advantage of 3D over 2D is the accurate multi-sensor fusion. Generally, 2D images' alignment and fusion is based on assuming the objects are lying on a plane. Thus, the 2D affine transform results in rough image alignment. Using the depth information provided by the point cloud, the images from different sensors can be accurately aligned to the same coordinate system with the projection matrix as shown in Figure 3-18 (f). Finally, the 3D FEM simulation of ECPT in COMSOL is conducted to validate our 3D ECPT system. The simulation environment setting is the same as the experimental study environment set up. The eddy current pulse is 200A with 200Hz. The heating time is 200A. Figure 3-19 (e) shows the simulation results of the RCF on the railhead. The 3D FEM model provides both 3D physical coordinates and temperature responses, which is valuable for the quantified evaluation of defect characterization. Accordingly, the proposed 3D ECPT in this paper matches the 3D FEM model, and therefore, the 3D ECPT has great potential for quantified NDT&E.

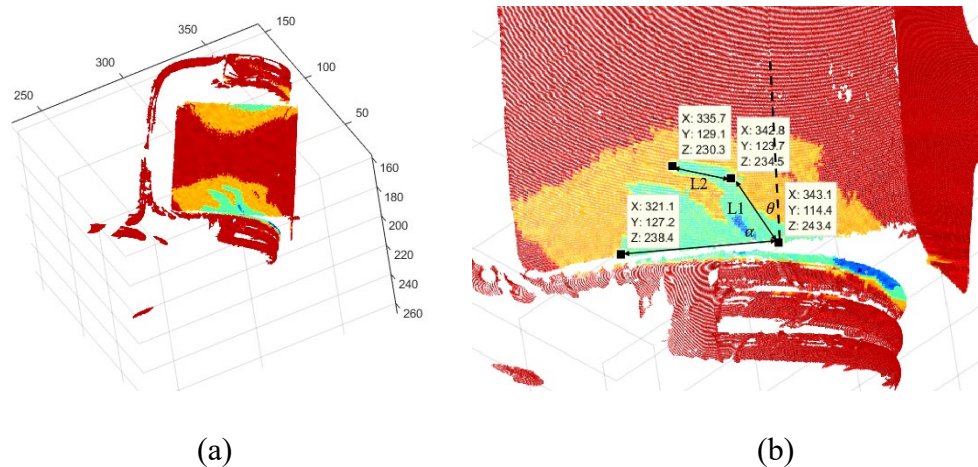


Figure 3-19 Defect sizing and localization

In this section, the defect area is enhanced by thresholding the temperature value. The defect size and angle are measured manually. Figure 3-19 (a) shows the thresholded thermal point cloud and Figure 3-19(b) shows the measured crack size and angle. The 3D ECPT not only gives a better measurement of defect geometry and visualization but also for analysing the defect thermal transient response and further analysis of the defect characteristics, such as size, depth and crack angle. This part is introduced in chapter 4.

3.4 Summary

In this chapter, a new 3D ECPT system was proposed. The primary task is unifying the coordinate system from different imaging sensors. The unification process was done by finding the matched features from the multi-spectrum images, and the 3D scanning and rendering process from the Kinect system and David 3D system were presented individually. Fusion of the point cloud with thermal IR images enables the ability not only to detect the defect but also quantify it. The point cloud brings the information of geometry to the thermal IR image, which solves the blurred problem of the thermal IR image to some extent. Finally, an accurate colour image-thermal image alignment and fusion was performed. The multi-spectrum image also brings complementary information, which helps in further analysis and detection of the defect.

4 DEFECT DETECTION AND VALIDATION USING THE 3D ECPT SYSTEM AND VALIDATION

This chapter describes the studies on defect detection and quantification using the 3D ECPT system. PCA is a statistical tool for high dimensional data feature extraction, so it is applied to the point cloud. Section 4.1 is a case study of rail track defect localization using PCA. Section 4.2 proposes a new transient feature of skewness for defect detection and quantitative analysis. The thermal gradient is a physical parameter in heat transfer. In section 4.3, the quantification of the thermal gradient is given and visualized in 3D through validation with man-made and natural RCF crack samples.

4.1 Segmentation of thermal point cloud data of rail track using PCA

The point cloud segmentation is a process that divides the point cloud into multiple regions. The point cloud has the same properties in a single region [151]. This study aims to automatically localize the ROI of RCF on a rail track head and enhance the visualization of cracks in depth.

Point cloud segmentation is a widely discussed topic in computer vision in both 2D and 3D contexts. Besl [152] first proposed the seeded-region method which clusters the points with seeds and grows by adding nearby points. Biosca [153] introduced an unsupervised clustering algorithm with fuzzy logic.

The normal vector of the point cloud surface represents the curvature information of the 3D object. In this specific study, the normal vector is used for the localization of the RCF since the RCF only appears on the shoulder of the rail track head. The curvature information of the rail track shoulder is detected and gives the interest of region (IOS) of the defect area.

The PCA [154, 155] is used as a tool to assess the planarity of point vectors. For each point \vec{p}_q in the 3D point cloud sets, the first step is finding the nearest point set of the query point. Then, the covariance matrix is calculated as:

$$C = \frac{1}{k} \sum_{i=1}^k (\vec{p}_i - \vec{p}_q)(\vec{p}_i - \vec{p}_q)^T \quad (4-1)$$

where $\vec{p}_q = (x_q, y_q, z_q)$ denotes the coordinate of the query point, $\vec{p}_i = (x_i, y_i, z_i)$ denotes the coordinate of the surrounding point cloud sets, and k is the number of the surrounding point cloud sets.

Since the covariance matrix denotes the dispersion of the data, it estimates the direction in which the data mainly lies. [156]. Using PCA on the 3D point clouds yields the principle orthonormal planes $p = [\vec{p}_1, \vec{p}_2, \vec{p}_3]$ of the point cloud set. Thus PCA is one solution to extract normal vectors of a point cloud surface. The third principal component vector \vec{p}_3 is the normal vector of the point cloud plane.

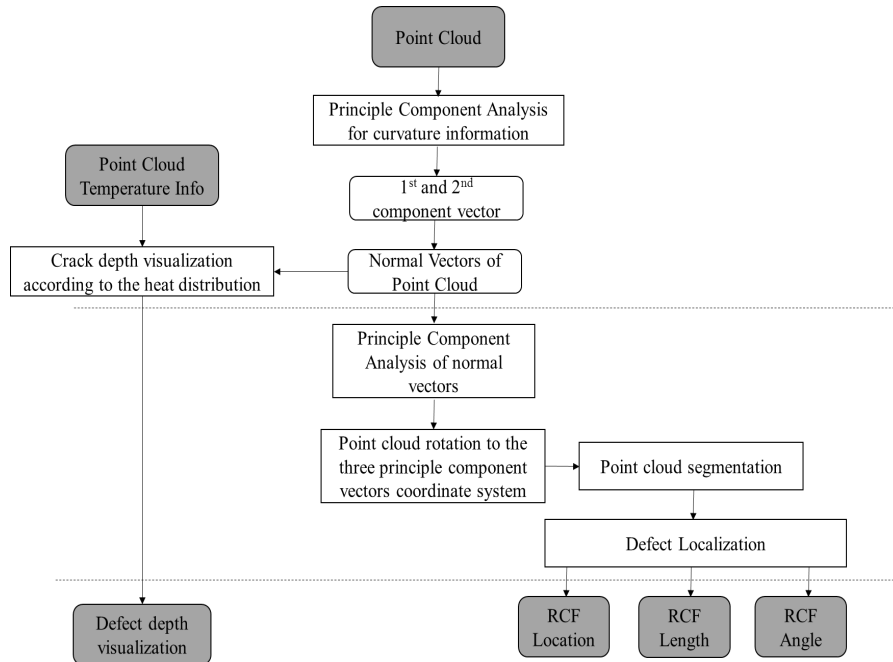


Figure 4-1 Point cloud command window

Figure. 4-1 shows the procedure carried out for defect localization and visualization. First, the curvature information which comprises normal vectors of the point cloud is extracted using PCA [157].

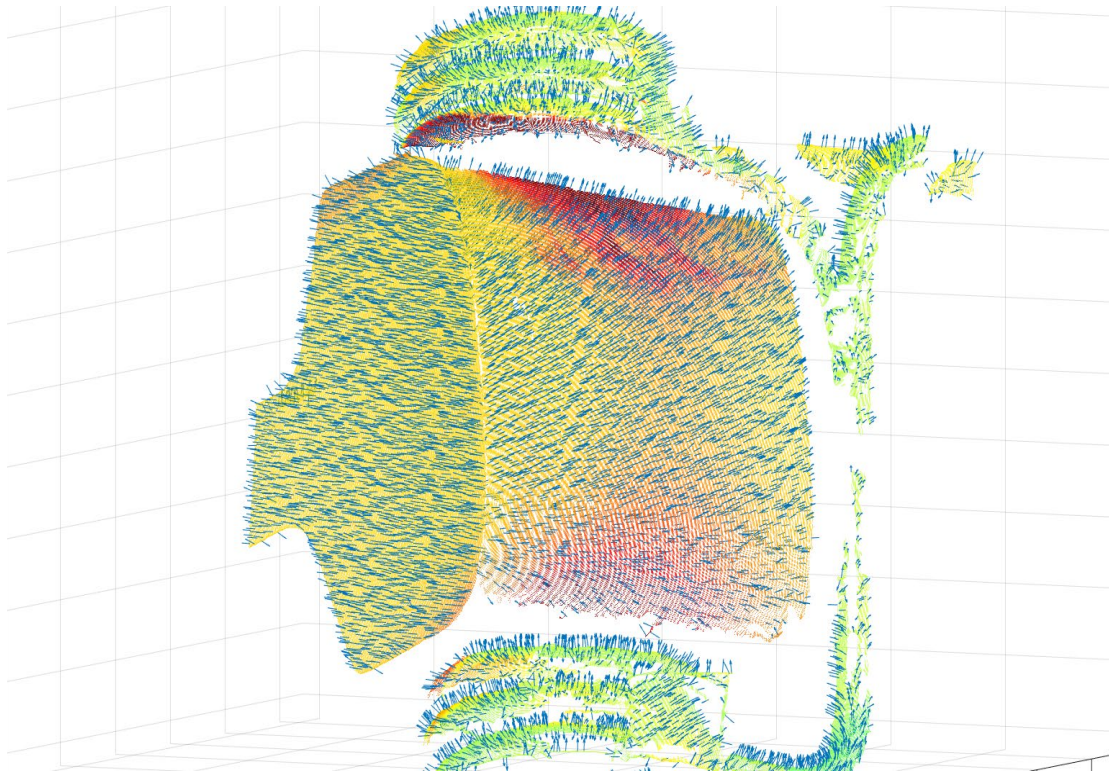


Figure 4-2 The normal vector of rail track head

Since that the RCF appears in the shoulder of the rail track head, the shoulder position is localized with the normal vectors information. In this case study, the rail track head is a cubic object. By the same principle, using PCA to the normal vectors, the point cloud of the rail track head can be projected into the orthogonal way (front, and back sides on the x-axis; left

and right sides on y-axis; top and bottom sides on z-axis).

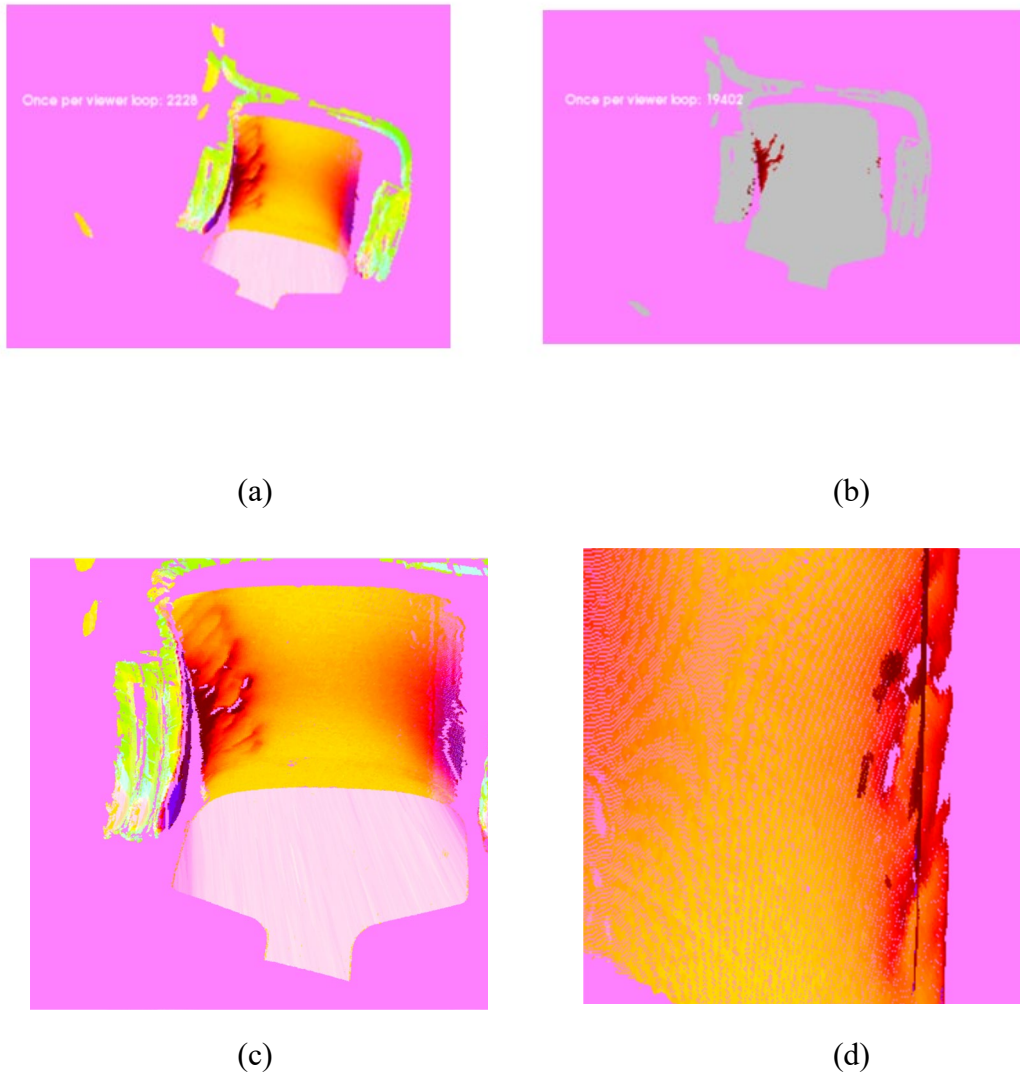


Figure 4-3 Defect enhancement, localization and visualization

The ROI lies on the left, right and top sides of the railway head as shown in Figure 4-3 (a). The rail track is separated into six parts: 2 rail track shoulders, and the rail track front, back, top and bottom. For the thermal texture colour. Finally, the thresholding image is shown in Figure 4-3(b).

After crack localization, the crack area is enhanced and visualized as a sink under the surface. Since the 3D scanner can only capture surface information, the original data cannot show the depth of the RCF. However, previous studies [2-3] have shown that the thermal

information captured by the IR camera carries information about defect depth. Reference [4] showed that the maximum temperature gradient is a quantification of the defect depth and defect angle. In this work, we visualized the depth of the crack and sunk the defective point cloud under the surface according to the maximum temperature gradient. Figure 4-3 (c) shows the enhanced point cloud, and Figure 4-3 (d) is the zoomed area visualization.

4.2 Skewness features

During the ECPT experiment, the transient temperature response of the specimen was captured by the IR camera and recorded as a thermal image sequence. In each frame, the thermal image is recorded in a two-dimensional matrix $I(x,y)$ that gives the temperature at each pixel location. The 3D matrix $Y(x,y,n)$ is used to record the whole thermal image sequences, where n is the frame number. The frame number can be later transferred to represent time as $t = n/f_s$, where f_s is the recording frame rate.

Many studies have been carried out for the study of transient temperature response on active thermography. Reference [61] used the maximum thermal rise as a feature of defect depth. Reference [83] used PCA and ICA as distinguishing features for defect detection. Other methods, such as blind source separation [62], also show that the transient temperature response provides information not only on defect size but also defect depth. In this study, the new skewness feature of the transient temperature response is used. This result is validated for man-made cracks with different defect depths.

4.2.1 Thermal transient response in ECPT

In the ECPT experiment, the transient thermal responses in both the heating stage and the cooling stage contain rich information. The defect can be identified and localized from the heat flow discontinuity (geometry side) and heat transfer curve. Figure 4-4 shows the 3D heat point cloud at the end of the heating stage. As can be seen from Figure 4-4, the defect further

from the excitation coil shows low contrast between the defective and defect-free area. For comparison study, five typical points are selected and investigated as follows:

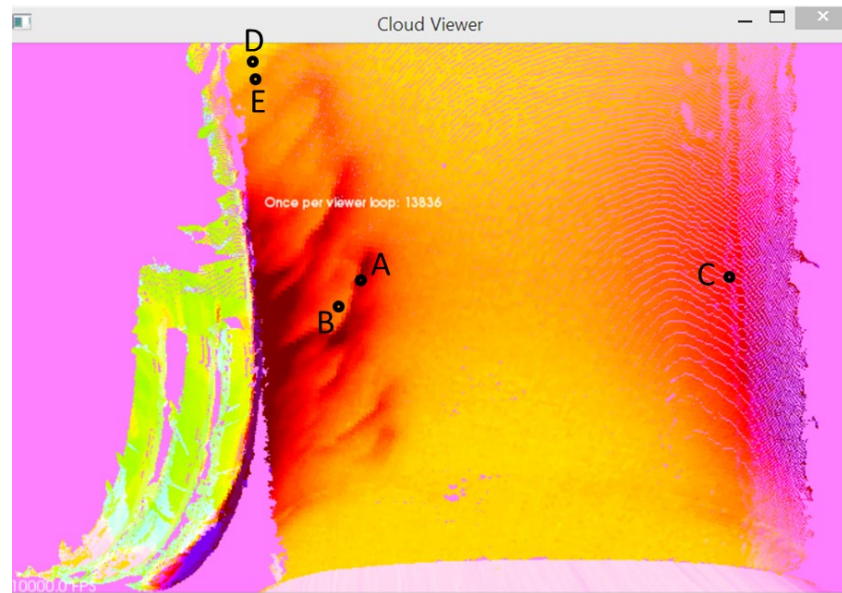


Figure 4-4 Selected points locations

- Point A: defect point near the excitation coil;
- Point B: point near defect point proximal to the excitation coil;
- Point C: non-defect point near to the excitation coil;
- Point D: non-defect point far from the excitation coil;
- Point E: defect point far from the excitation coil;

The temperature curvature is shown in Figure 4-5. Comparing points A and E, both of which are defect points, we find that they share the same curvature shape, with a rapid temperature rising and cooling. Comparing point A with B and point E with D, we find that they are close to each other in geometry. The heat is propagated from point A to B; and point E to D. Thus, point B has a slow temperature rise and very slow temperature decay. The same situation happens with points E to D; however, for point E, the point is too far from the excitation coil to be heated in the non-defect area. The temperature response of point D appears as a slow, rising line-shape curve. As a result, there appears to be a strong difference in curvature between the defective area and the defect-free point near the defect.

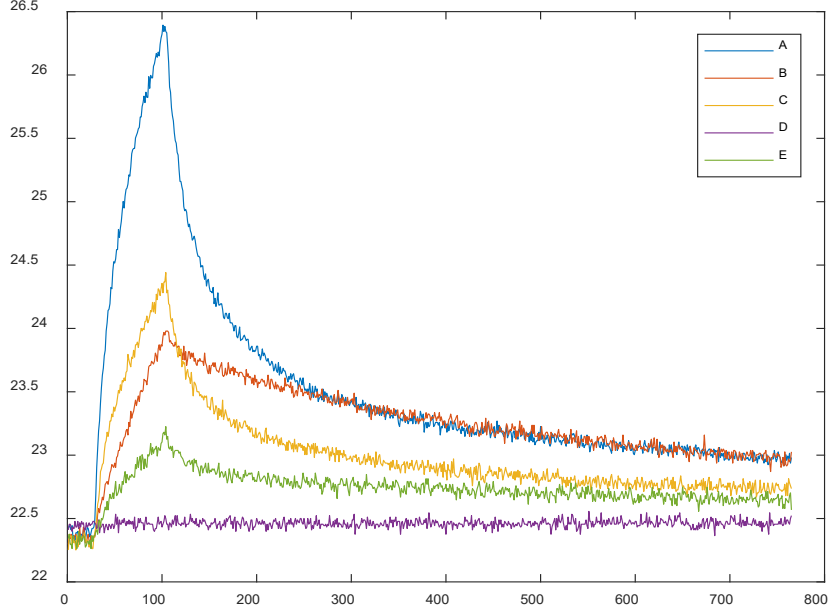


Figure 4-5 Thermal transient response on selected points

According to Newton's cooling law, the heat transfer in the cooling stage is given as follows:

$$\frac{dQ}{dt} = h * A * (T(t) - T_{env}) = h * A \Delta T(t) \quad (4-2)$$

where Q is the thermal heat in joules, h is the heat transfer coefficient, A is the heat transfer surface area, T is the surface temperature and T_{env} is environment temperature: $\Delta T(t) = T(t) - T_{env}$.

The solution to Newton's equation is written as

$$T(t) = T_{env} + (T(0) - T_{env})e^{-\frac{t}{t_0}} \quad (4-3)$$

Thus,

$$\Delta(T)_1 = T(t) - T_{env} = a_1 * e^{k_1 t} \quad a_1, t, k_1 > 0 \quad (4-4)$$

The heating stage of the ECPT system accounts for both heat diffusion and joule heating, as given in Eq. (4-5):

$$\frac{\partial T}{\partial t} = \frac{\lambda}{\rho C_p} \left(\frac{\partial^2 T}{\partial x^2} + \frac{\partial^2 T}{\partial y^2} + \frac{\partial^2 T}{\partial z^2} \right) + \frac{1}{\rho C_p} q(x, y, z, t) \quad (4-5)$$

The total power P given by the inductor heater is constant.

Because of the heat dissipation, which is $\frac{\lambda}{\rho C_p} \left(\frac{\partial^2 T}{\partial x^2} + \frac{\partial^2 T}{\partial y^2} + \frac{\partial^2 T}{\partial z^2} \right)$ (4-6), the curve in the heating stage is non-linear, as shown in Figure 4-5. In the rest of this section, all image sequences are pre-processed with the subtraction of the first frame:

$$I'(x, y, n) = I(x, y, n) - I(x, y, 1) \quad (4-7)$$

As a result, the time–temperature curve for each pixel $I(x, y)$ starts from zero.

A single thermal image is insufficient for the decision making of the defects. There are three reasons for this. First, it is hard to select which frame to analyse to locate the defect. Second in the specific frames, the sub-surface cracks have the same temperature as they are in the non-defective area, which results in difficulties and inaccurate judgement in determining the crack area. Finally, it is almost impossible to quantify defect size and depth based on the single frame. For these reasons, the transient thermal response is used, which is captured by a high-speed IR camera and recorded as optical flow. The optical flow can be used to target the displacement of images at different time slot. The displacement of the thermal flow (heat flow) reflects the heat propagation direction and magnitude. Quantified heat flow can help the quantification study of the factors related to the defect size, depth and direction.

Based on the optical flow, different features are extracted with advanced signal processing methods, such as PCA, ICA and blind source separation. This section gives the analysis of the transient thermal responses in the statistical histogram manner, and different defect depths are compared and with skewness feature.

Skewness is the measurement of data to determine its asymmetry around its mean. It is a statistical tool that has the advantage that it is independent of the mean of the distribution.

Skewed distribution is compared to the normal distribution, where a normal distribution is symmetrical, with a skewness of zero. A negative skewness reveals that more data spreads

on the left of the mean, where a positive skewness reveals that more data spreads on the right of the mean.

The systematic study of skewness began with Karl Pearson [158], who first investigated the property of skewness for different types of statistics. This was followed by the works in [159-162], which gave a summary of skewness properties of different distributions including Gamma distribution, log-logistic distribution, lognormal distribution and Weibull distribution. More recently, [162] assessed different ways of measuring skewness and how to decide which way fits best. The ways of measuring skewness include the following:

$$\frac{\text{mean}}{\text{median}} \quad (4-8)$$

$$\frac{\text{max}-\text{median}}{\text{median}-\text{min}} \quad (4-9)$$

$$\frac{1/2(\text{min}+\text{max})}{\text{median}} \quad (4-10)$$

$$\frac{\frac{1}{n}\sum_{i=1}^n(x_i-\bar{x})^3}{\left(\sqrt{\frac{1}{n}\sum_{i=1}^n(x_i-\bar{x})^2}\right)^3} \quad (4-11)$$

$$\frac{3(\text{mean}-\text{median})}{\text{standard deviation}} \quad (4-12)$$

Equations. (4-11) and (4-12) are the standard measurement of skewness. Equation (4-10) is the formal definition of skewness, and Eq. (4-12) is Pearson's skewness coefficient.

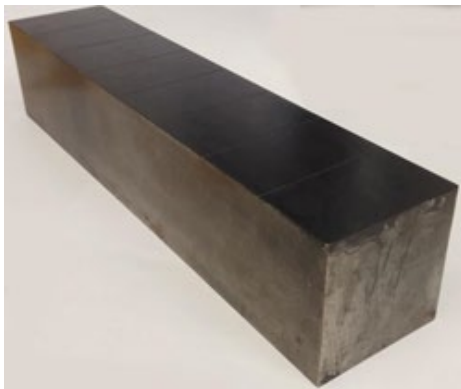
In this study, Eq. (4-11) is used for the measurement of the skewness of the transient thermal response.

4.2.2 Skewness features for the characterization of defect depths and validation

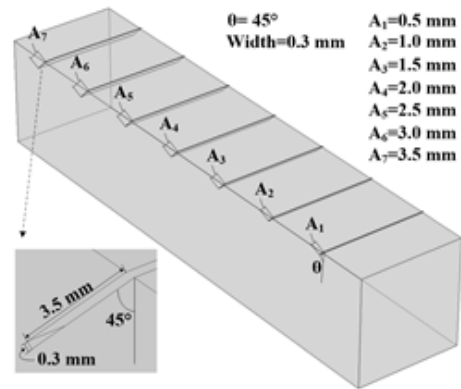
This study investigates the following points:

- How does the defect depth affect the the histogram of the temperature curve (the histogram mean, standard deviation and skewness)?
- Is the skewness feature related to the defect depth? If so, why?
- What is the skewness feature in the heating stage, cooling stage and all stages in the ECPT experiment?
- Can the skewness feature detect sub-surface defect?
- Is the skewness robust to other factors, such as heating time, cooling time and sampling frequency?

In this study, one man-made steel sample with cracks of different depths was used and tested with an ECPT system at Newcastle University. The ECPT experimental set-up used a heating time of 200ms and cooling time of 800ms. A helomots coil was used for induction heating. The capturing frame rate of the IR camera was 50 frames per second. The excitation frequency was 260kHz with a current magnitude of 300A.



(a) Photo of the artificial sample



(b) Sketch diagram of the artificial sample

Figure 4-6 Photo and sketch diagram of artificial angular crack sample

Figure 4-6 gives the photo and sketch diagram of the artificial angular crack sample. The sample is $(300 \times 30 \times 63) m^3$ in dimension. The defect comprises open-angler slots with different depths of 0.5mm, 1.0mm, 1.5mm, 2mm, 2.5mm, 3.0mm and 3.5mm. The inclination angle of the angular slots are 45° . The material of the sample is AISI 1045 carbon steel. The material density is $7.80 \times 10^3 kg/m^3$, the heat capacity is $4.86 \times 10^2 J/kg \cdot K$, the thermal conductivity is $49.8W/m \cdot k$ and the electrical conductivity is $6.17 \times 10^6 S/m$.

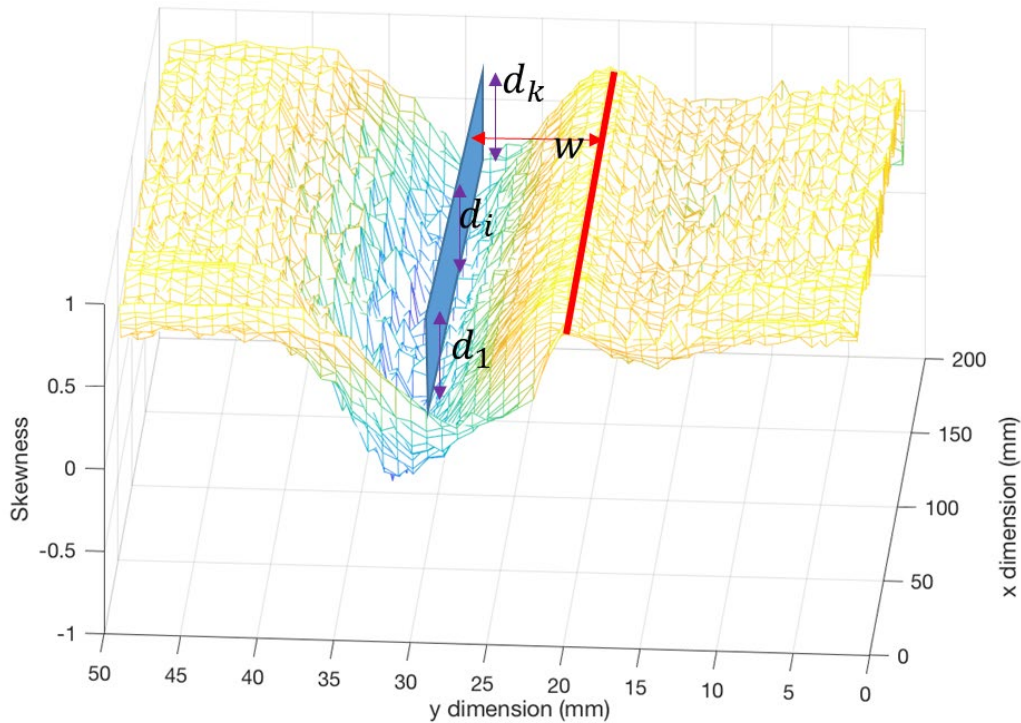


Figure 4-7 Measured parameters on skewness distributions

Figure 4-7 shows one skewness mesh image. The measured parameters included: the mean skewness in the y dimension, the mean peak to valley value d_i in the y dimension, the standard deviation, the mean of the temperature histogram and the skewness distribution in 3D space.

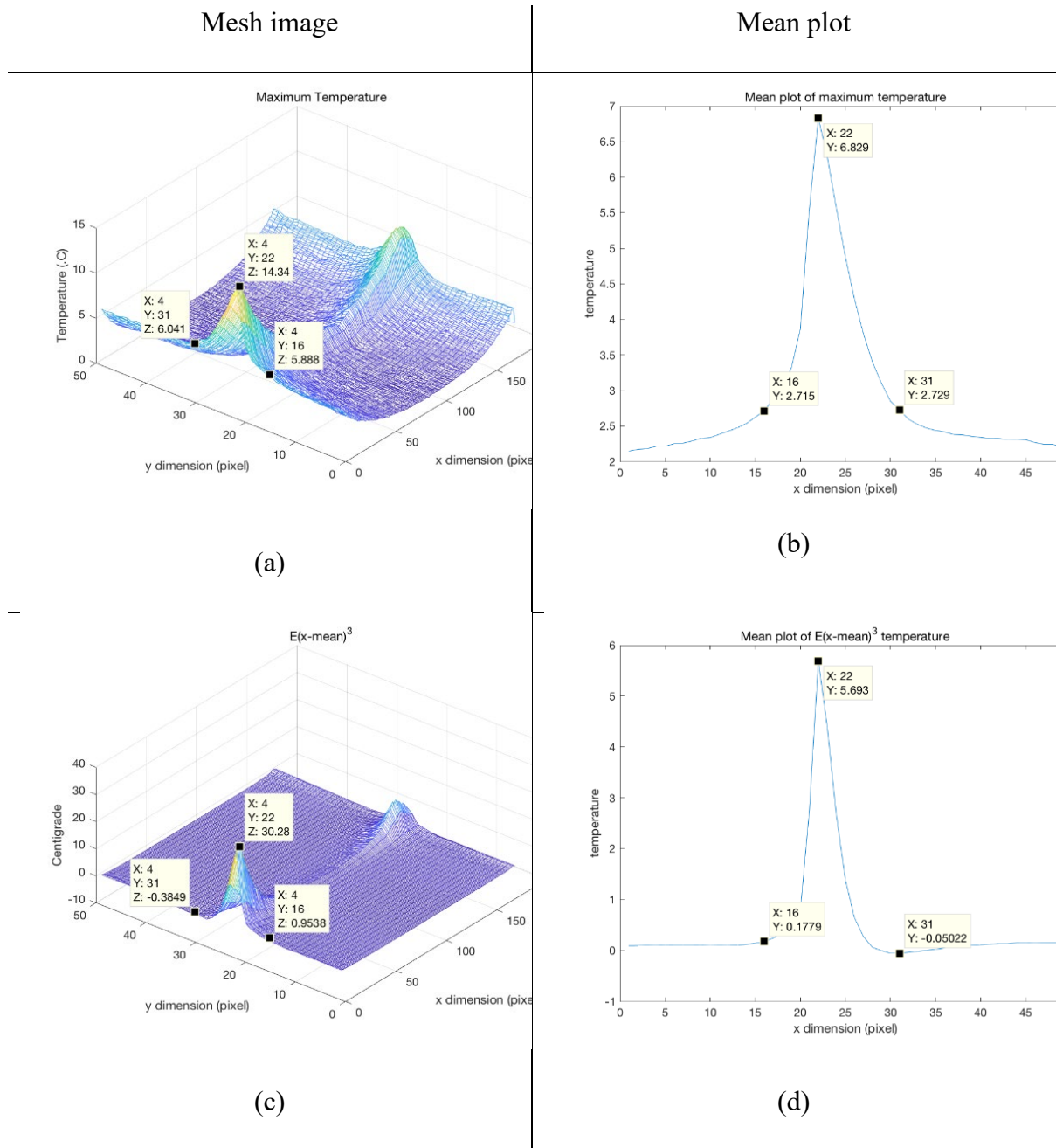
4.2.3 Statistical analysis of the transient thermal response

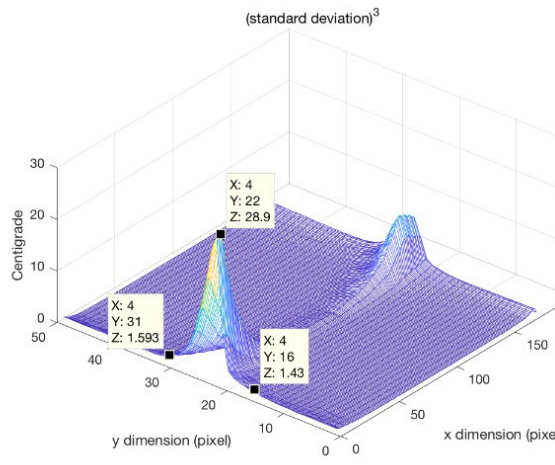
This part uses the data from the entire ECPT experiment, includes the heating and cooling stages. The heating time is 200 ms (50 frames) where as the cooling time is 800 ms (200 frames).

The image sequence can be treated as a 3D matrix. The pixel at location (x, y) in the specific frame n is denoted as $I(x, y, n)$. This part begins with the analysis of the maximum temperature matrix $I_{Max}(x, y, n = 50)$, mean temperature matrix $\bar{I}(x, y) = \frac{\sum_{n=1}^N I(x, y, n)}{N}$ and

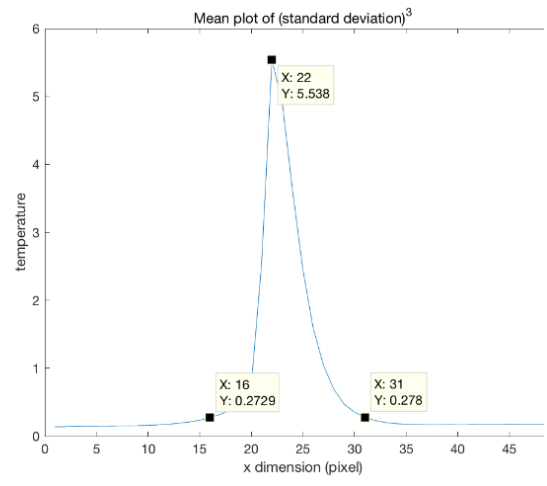
standard deviation matrix in time space $std(x, y) = \sqrt{\frac{\sum_{n=1}^N (I(x, y, n) - \bar{I}(x, y))^2}{N-1}}$, where N is the total number of frames.

The description that follows focusses on comparison study of I_{Max} , $E(x - \text{mean})^3$, $std(x, y)^3$ and skewness. Only a crack of 3mm in depth crack is included here because of space limitation of the thesis.

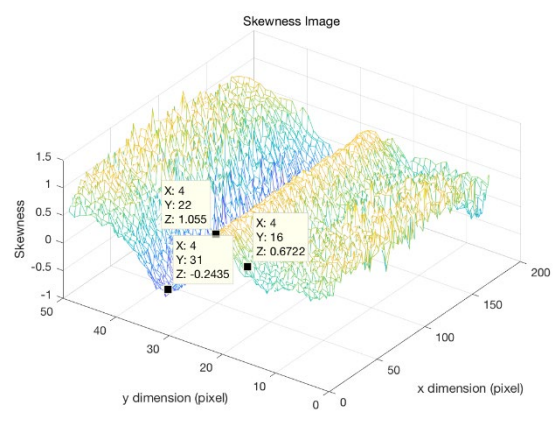




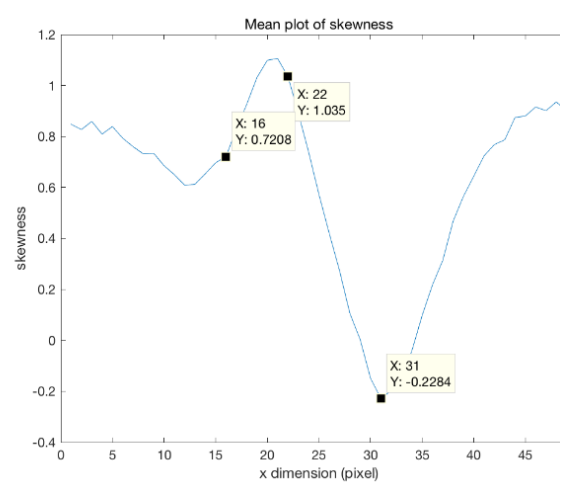
(e)



(f)



(g)



(h)

Figure 4-8 Maximum temperature, $E(x - \text{mean})^3$, *standard deviation*³ and skewness

First, consider the maximum temperature frame. The maximum temperature frame was captured on the last frame in the heating stage. This is usually considered the best quality frame for active thermography because it gives the highest thermal contrast between the defective area and the defect-free area. Reference [121] used the maximum temperature frame for the RCF detection and localization on a rail track head.

The calculation of skewness is given in Eq. (4-13)

$$\frac{\frac{1}{n}\sum_{i=1}^n(x_i-\bar{x})^3}{\left(\frac{1}{n}\sum_{i=1}^n(x_i-\bar{x})^2\right)^{\frac{3}{2}}} = \frac{E(x-\text{mean})^3}{\text{standard deviation}^3} \quad (4-13)$$

In Eq. (4-13), the skewness is the ratio of two parts, A/B , where $A = E(x - \text{mean})^3$. Part A is the re-location of the data, and it is zero centred. Afterwards, it is powered to the order of three. B is the standard deviation to the power of three. Thus, the study investigates the relationship between A and B. Figures 4-8 (a), (c), (e) and (g) show the mesh images of A and B and their skewness ratios.

For the four images on the left column above, we denote the pixel at location (x, y) in image q as $I_q(x, y)$. For example, the peak point in image a is denoted as $I_a(4,31)$. The same rule applies to the four curves on the right column, where $y_n(x)$ denotes the value of the point at location x in image n.

The images on the left column plot the mean values over the y dimension of the left images. The curves $P(x)$ on the right column are calculated as

$$P(x) = \frac{1}{k}\sum_{y=1}^k I(x, y) \quad (4-14)$$

From the figures, we can see that the attenuation in y dimension of $E(x - \text{mean})^3$, $(\text{standard deviation})^3$ from peak to valley keeps consistency with the maximum temperature frame. The following can be seen from single pixels: $I_a(4,22)$ to $I_a(4,31)$ and $I_a(4,16)$; $I_c(4,22)$ to $I_c(4,31)$ and $I_c(4,16)$; $I_e(4,22)$ to $I_e(4,31)$ and $I_e(4,16)$ and $I_g(4,22)$ to $I_g(4,31)$ and $I_g(4,16)$. The spatial distances from peak to valley are 9 pixels (left side) and 5 pixels (right side). The mean values over the y dimension share the same law as the single pixels.

For the attenuation in the z dimension from peak to valley, the $(\text{standard deviation})^3$ and maximum temperature frame are almost symmetrical regardless of the crack angle. In contrast, $E(x - \text{mean})^3$ is more relative to the crack angle (45° from the surface to the bottom left), where it can be seen in the left column of the mean value curves and described as outlined below.

The maximum temperature frame (mean value) remains the same, as can be seen from $y_b(31) = 2.729$; $y_b(16) = 2.715$. For the standard deviation (mean value), $y_f(31) = 0.2729$; $y_f(16) = 0.278$; which remains almost the same.

However, the exception of $(x - \text{mean})^3$ is influenced by the crack angle and results in the skewness affected by the crack angle. Here, $y_d(31) = -0.05022$ is a negative number and $y_d(16) = 0.1779$ is positive. The negative value of $y_d(31)$ reveals the temperature curves on column $y = 31$ are left skewed, and the positive value of $y_d(16)$ reveals that the curves on column $y = 16$ are right skewed.

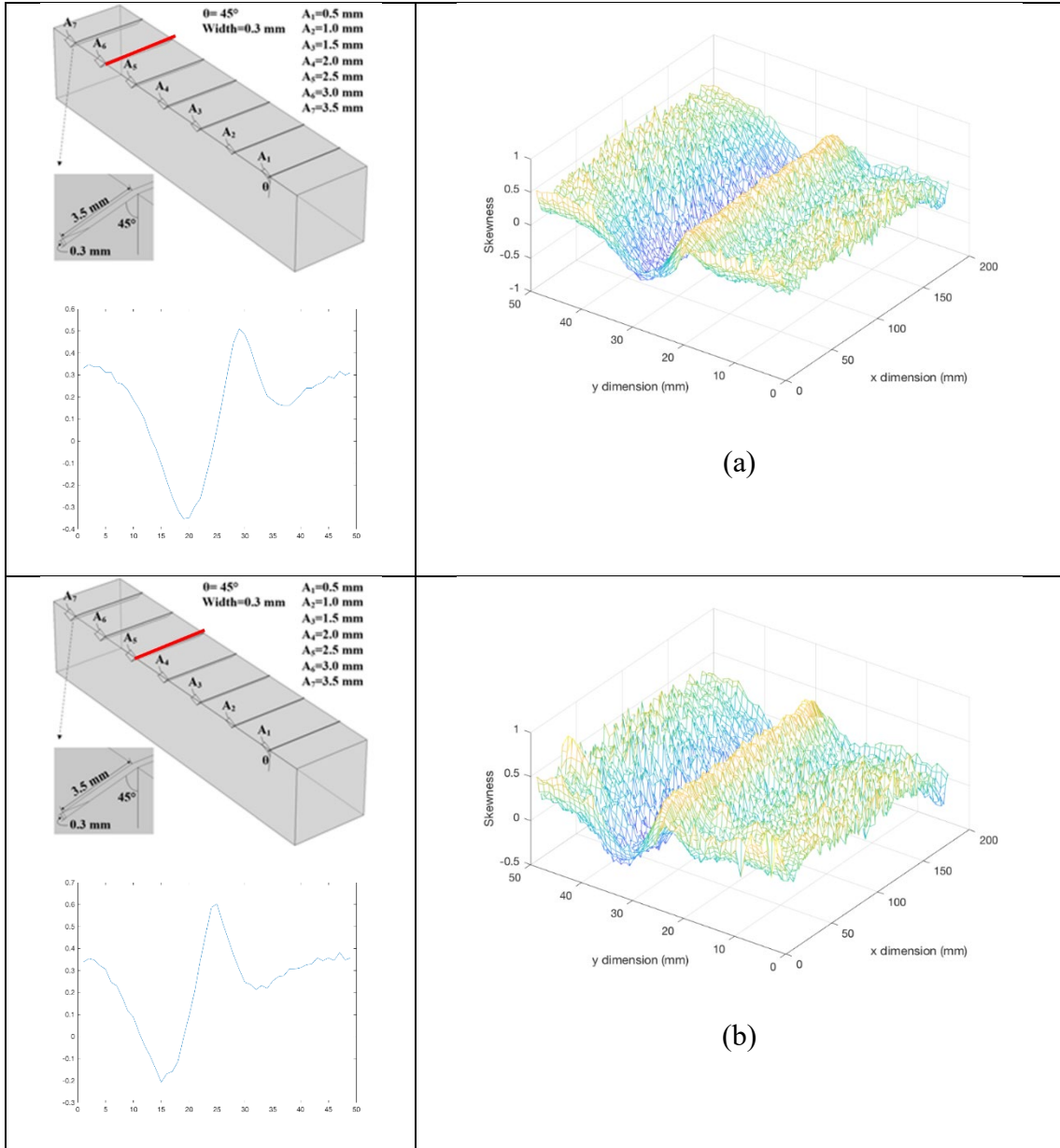
Figures 4-8 (c), (e) show that the amplitude of standard deviation and $E(x - \text{mean})^3$ have a strong dependence on the distance to the excitation coil. However, their ratio (skewness) is irrelevant in terms of the distance to the excitation coil. This can be obtained as in non-defective area, where $E(x - \text{mean})^3$ is proportional to $(\text{Standard deviation})^3$ regardless of its distance from the excitation coil. In the defective area, besides when the effect from distance to the excitation coil is removed, the skewness points to the crack direction in the skewness goes deeper (smaller) in the crack direction.

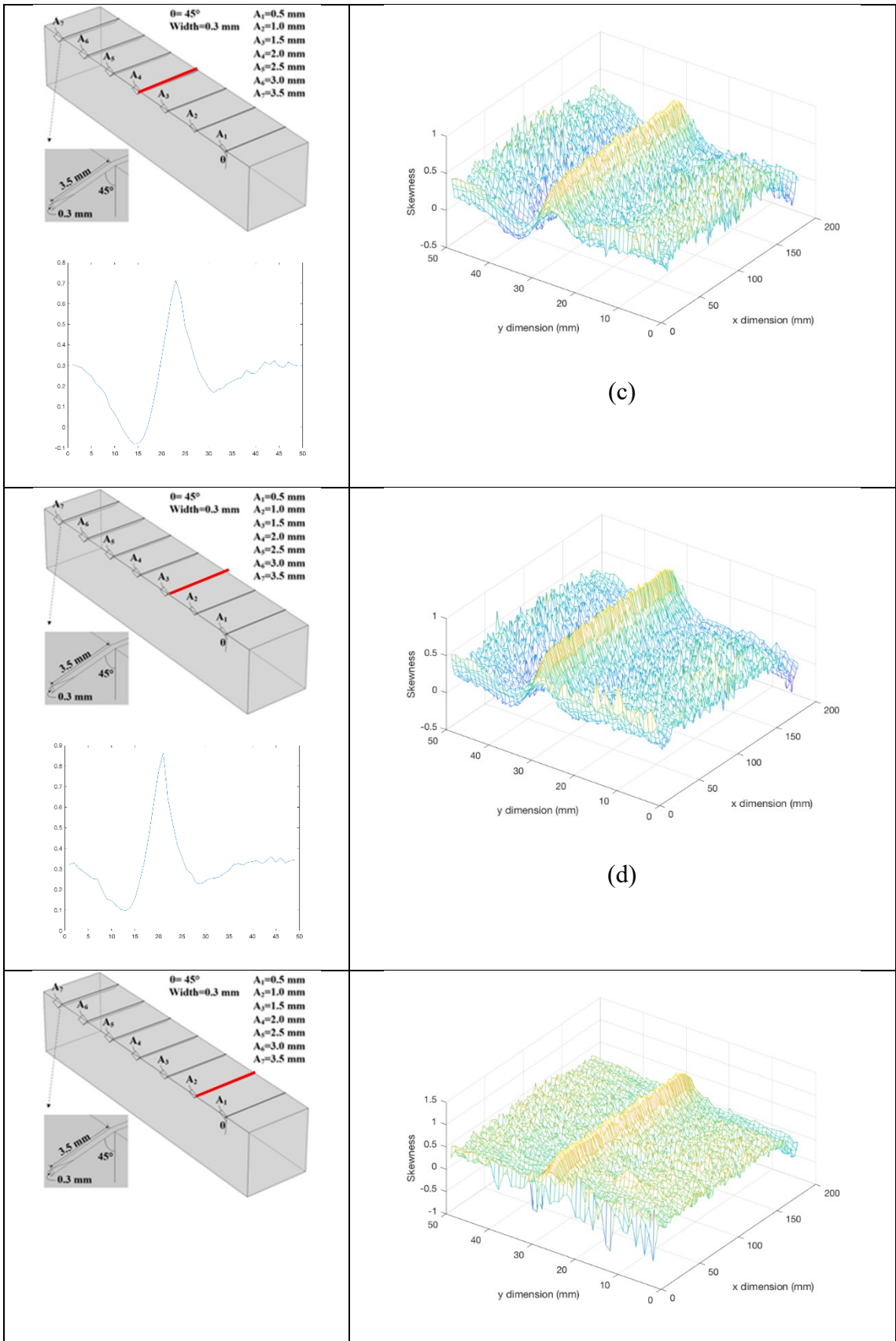
There are two factors that results in a higher temperature at the left and right sides of the man-made slot. First, this area is closer to the excitation coil. Second, the skin effect of the eddy current leads to a higher eddy current density in the edge region. From Figure 4-8 (h), it can be seen that the skewness is a feature independent of crack position and excitation position because the figure shows an almost line shape in the y dimension. The skewness feature is not only independent of the effect of uneven heating with the distance to the excitation coil, but it is also independent of the skin effect of the eddy current. (In the different positions of the cracks, the eddy current has different distributions where the edge area has a higher current density than the middle area).

The next section investigates the relationship between skewness and defect depth.

4.2.4 Skewness feature versus depth

This section considers the skewness relative to the defect depth. As in the previous sections, the mean operator is applied to the y dimension of the mesh image, and the curve is plotted in the bottom left in each row of the table.





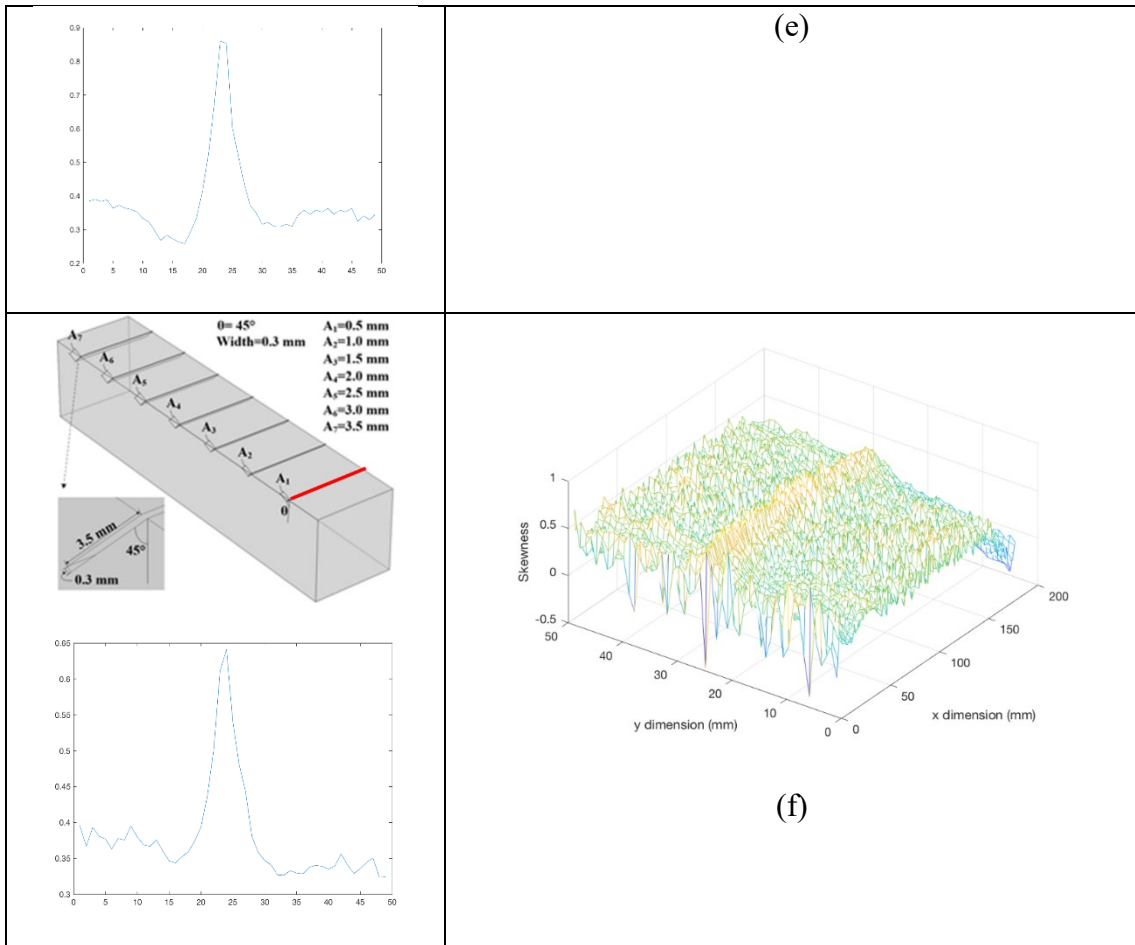
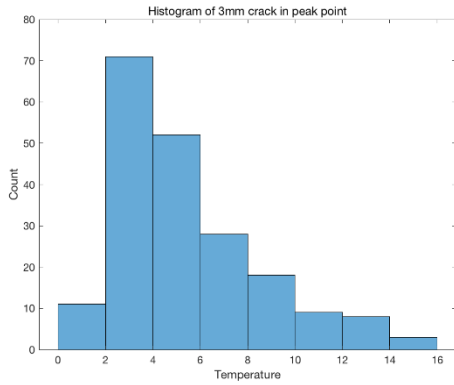
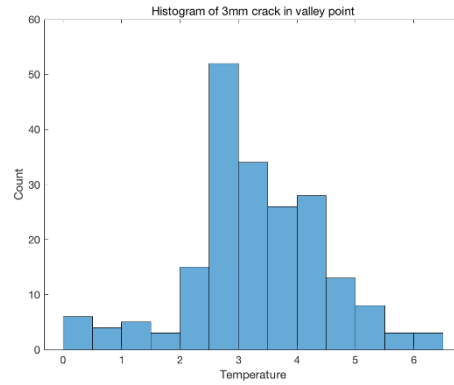


Figure 4-9 Skewness feature on different depth

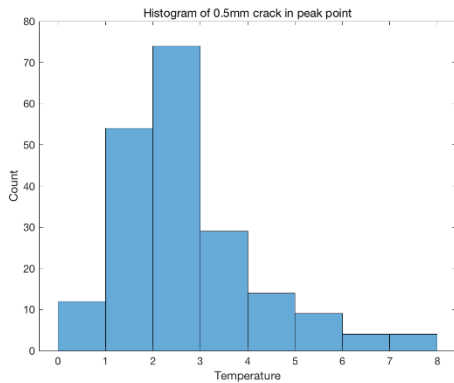
The first thing to note is that the surface crack has the highest skewness. This conclusion is identical to that in previous section 4.2.4 and proves that the skewness feature can locate the surface crack location with the highest skewness value. This phenomenon is caused by the skin effect and heat dissipation. The eddy current tends to gather at the edge or the surface area. Thus, it produces more heat in the crack area and then causes larger heat dissipation from the crack point to the nearby region.



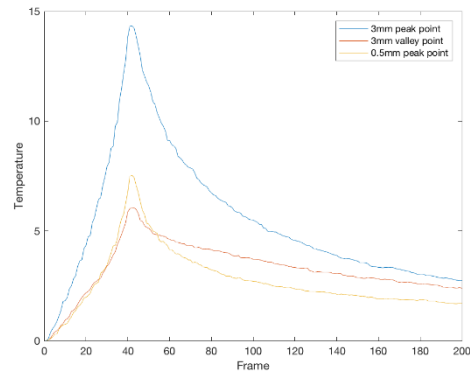
(a) Skewness(3mm) peak = 1.0554



(b) Skewness(3mm) valley = -0.2435



(c) Skewness(0.5mm) peak = 1.2354



(d) Temperature curves

Figure 4-10 Histogram of 3mm crack and 0.5mm crack at peak (valley point) and temperature curve

Figure 4-10 (a) shows the histogram of the peak pixel ($I_a(4,22)$ in Figure 4-8) for a 3mm crack, and Figure 4-10 (b) is the histogram of the corresponding valley pixel ($I_a(4,31)$ in Figure 4-8). From the histogram and the skewness value, we find that the peak point (a) is positively skewed, whereas the valley (b) is slightly negatively skewed.

The histogram of peak pixel is shown in Figure 4-10 (c) for 0.5 mm crack. The corresponding valley pixel is not shown here because there is no valley pixel for 0.5 mm crack as can be noted in Figure 4-9 (f)

Sampe	Peak value	Valley value	Peak-valley	Peak_valley/ Δx
3mm	1.099	-0.2284	1.3274	0.1207
2.5mm	1.255	0.04639	1.2086	0.1209
2mm	1.357	0.2036	1.1534	0.1282
1.5mm	1.581	0.524	1.0570	0.1174
1mm	1.6	0.8101	0.7899	0.1128
0.5mm	1.3	0.9065	0.3935	0.0492

Table 4 Skewness peak and valley values

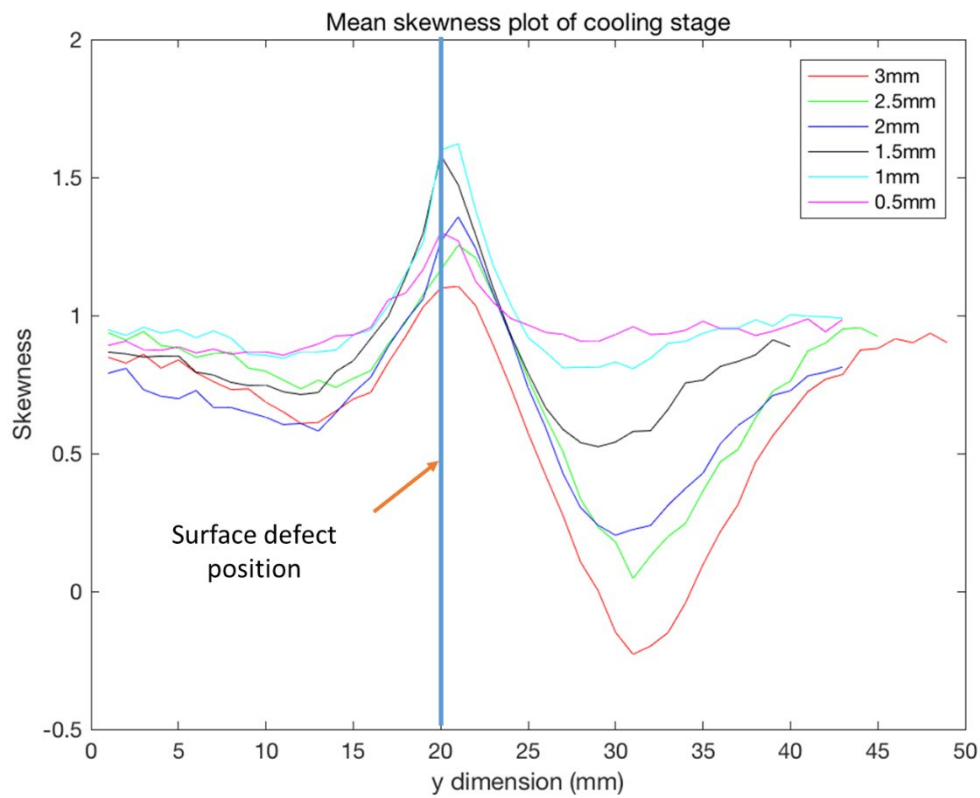


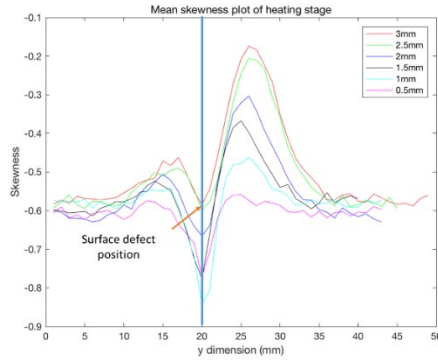
Figure 4-11 Mean skewness plot of different crack depth

From Table 4 and Figure 4-11 we can conclude that the skewness of the single pixel transient thermal response (pixel-level feature) cannot clearly show the defect depth. Table 4

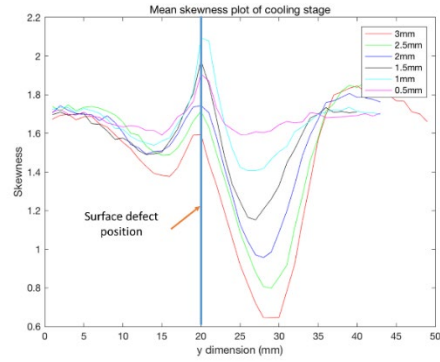
reveals the relationship between defect depth d and skewness peak value S_p and valley value S_v . The peak skewness gives the location of the surface crack; however, the peak skewness is not directly related to the depth of the crack. The crack depth is more related to the nearby valley skewness. Thus, the skewness is not a pixel-level feature but a local area feature. The skewness distribution in 3D is important for the analysis of the crack depth and angle. For the purpose of the quantification, 3D ECPT is needed in order to measure the skewness gradient in 3D space. This is because the skewness is a local area feature. Compared with the non-defective area, there is an abnormal transient thermal response in the crack area and its surrounding region, which causes changes in the skewness value. The skin effect causes the eddy current to gather in the crack area and induces a higher temperature rise in the heating stage and a very fast heat dissipation in the cooling stage. Thus there will be a peak skewness value in the crack position. In contrast, the surrounding area has a smooth temperature rise in the heating stage but a very slow temperature drop because of the heat transfer from the crack region. Thus, a valley skewness value will appear in the area surrounding the crack. In addition, the deeper the crack is, the smaller the skewness it has. For this reason, the skewness not only reveals the crack position and depth, but also the crack direction under the surface.

4.2.5 Skewness feature with different stages of ECPT (heating and cooling stage)

In the previous sections, data from all stages were used in the ECPT experiment. This section gives the study on the skewness feature over different stages in the experiment. The skewness of different responses from the periods of induced eddy current heating, thermal propagation, and cooling and the whole period are computed and shown in the individual tables. The skewness results at different locations are compared and discussed.



(a)



(b)

Figure 4-12 Skewness in different stages of the ECPT experiment

Stage: Heating

Sample	Peak value	Valley value	Peak-valley	Peak_valley/ Δx
3mm	-0.1744	-0.5848	0.4104	0.0684
2.5mm	-0.2058	-0.5989	0.3931	0.0655
2mm	-0.3034	-0.6655	0.3621	0.0603
1.5mm	-0.3677	-0.7763	0.4086	0.0817
1mm	-0.4616	-0.8418	0.3804	0.0634
0.5mm	-0.5588	-0.7722	0.2134	0.0427

Table 5 Skewness peak value and valley value in the heating stage

Stage: Cooling

Sample	Peak value	Valley value	Peak-valley	Peak_valley/ Δx
3mm	1.594	0.6466	0.9474	0.1184
2.5mm	1.714	0.8073	0.9067	0.1133

2mm	1.744	0.9706	0.7734	0.1105
1.5mm	1.976	1.165	0.8110	0.1352
1mm	2.093	1.407	0.6860	0.1143
0.5mm	1.906	1.595	0.3110	0.0622

Table 6 Skewness peak value and valley value in the cooling stage

In the above tables, the skewness in the heating stage (Figure 4-12 a), cooling stage (Figure 4-12 b) and all stages are compared and discussed. The relationship of their peak value S_p , valley value S_v , peak-valley S_{p-v} , depth d , and surface crack location P_{surf} are listed shown in Tables 4-6.

For the heating stage, the crack position appears at valley value S_v , whereas the peak value S_p has a monotonic relationship to the defect depth. The opposite is the case in the cooling stage. The crack position appears at peak value S_p , whereas valley value S_v has a monotonic relationship to the defect depth. This is because the heating stage and valley have opposite heat attenuations. In the cooling stage, the temperature curve is significant at the beginning and becomes smaller as it goes further towards the peak point. In contrast to the cooling stage, the temperature attenuation in the heating stage is small when it nears the peak point and becomes larger as it goes further from peak point. The inverse attenuation relationship in the heating and cooling stages make it unreasonable to conduct asymmetric measurement using skewness. Thus, the invertible transformations in Eqs. (4-15) and (4-16) are used; these can make the curve ‘looks symmetric’ in shape:

$$\tau(t) = \frac{d(T(t_1-t))}{dt} \quad (4-15)$$

$$T_m(t) = \int_0^{t_1} \tau(t) * dt \quad (4-16)$$

It is worth noting that the above transformations are invertible, which means that the information of the data is not lost with the transformations. The original temperature response and the modified temperature response are plotted in Figures 4-13 (a), and (b), respectively.

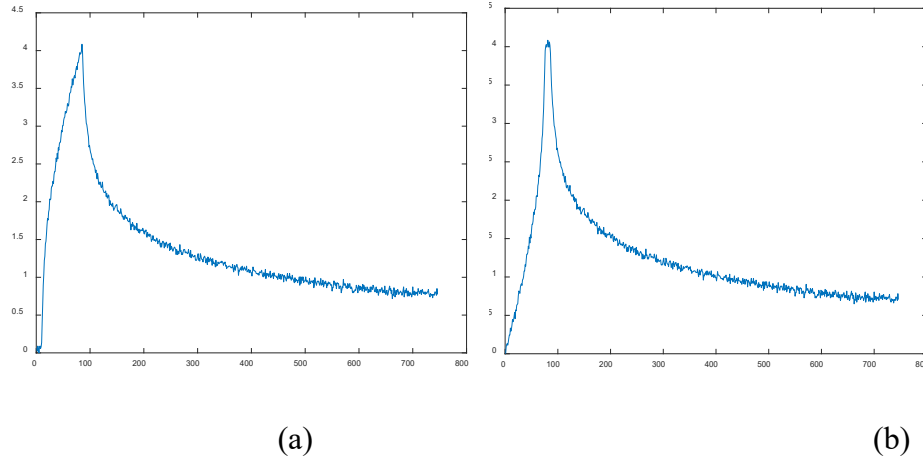


Figure 4-13 Design and computation of skewness features

For a deeper crack, the heat generation is quicker because the current tends to gather at the edges of the crack. At the beginning of the heating stage, joule heating of the eddy current is the main affecting factor for the heat generation. The temperature rise is almost a straight line of time. However, when approaching the end of the heating stage, with the increasing temperature divergence, non-linear heat dissipation takes effect. In addition, the larger temperature gradient between the crack point and surrounding point causes a larger heat propagation in this area, which leads to the temperature rise at the crack point becoming slower. (Joule heating and heat dissipation conflict with each other). For this reason, it appears as a peak skewness value, which means that the data lie in the high temperature area. In the cooling stage, only heat propagation exists, which leads to a rapid temperature drop at the maximum temperature point. Thus, the minimum skewness appears at the surface crack point, which means that the data mainly lie in the low temperature area.

For the skewness of the entire stage, the temperature curves are first pre-processed using Eqs. 4-16, and 4-17, which give make the temperature curve in the heating stage the same distribution as in the cooling stage. As a result, the relationships between crack location, depth, skewness peak value, S_p , and valley value S_v are the same as in the cooling stage: The location of S_p indicates the surface crack location P_{surf} . and S_v has a monotonic relationship to the defect depth, as shown in Figure 4-13.

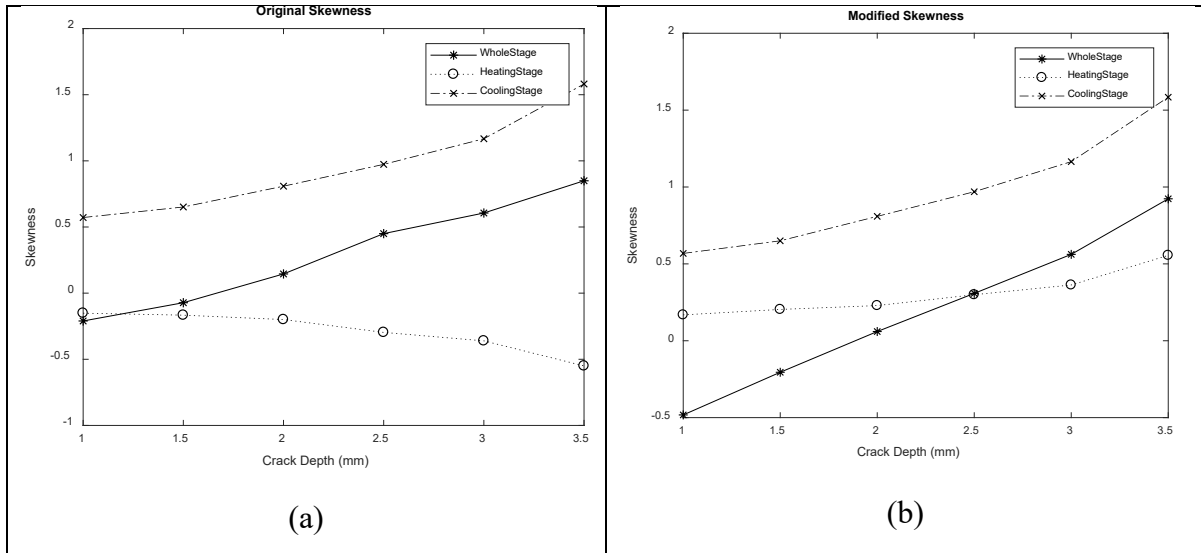


Figure 4-14 Skewness and crack depth; (a) original temperature response, (b) transformed temperature response with inversion of the heating stage.

Figure 4-14 shows the skewness values of the original thermal responses and the modified thermal responses. In summary, it can be found that there are two opposite properties of the skewness feature in the thermal responses at the heating and cooling stages as shown in the the Figures 4-12, and 4-14.

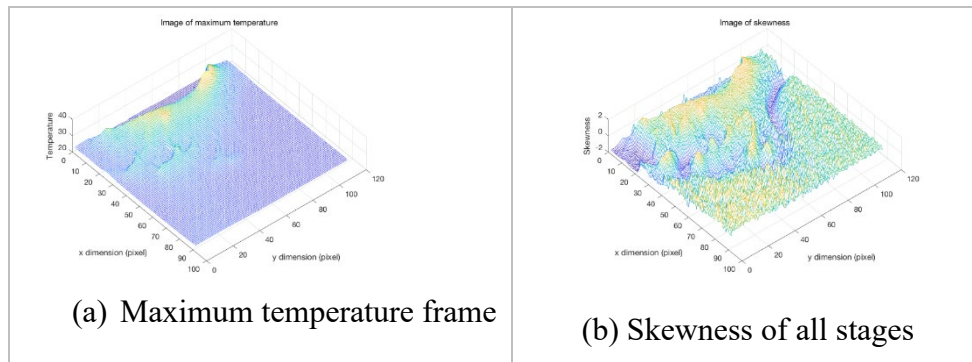
Opposite behavior 1: the first opposite behavior is in the valley and peak point of the skewness feature. In Figure 4-12 (a) which is the skewness value plot of the heating stage, the valley skewness position indicates the surface crack position. The peak skewness gives the linear relationship of defect depth where the larger the skewness, the deeper the defect depth. In the cooling stage shown in 4-12 (b), the peak skewness position gives the surface crack position. The valley skewness gives the linear relationship of defect depth where the smaller the skewness, the deeper the defect depth.

Opposite behavior 2: The second opposite behavior can be found in Figure 4-14 (a). The skewness value in the heating stage is a negative correlation of defect depth: The deeper the defect, the smaller the skewness value. The skewness value in the cooling stage has a positive correlation where the deeper the defect, the larger the skewness value.

Mathematically, these opposite behaviours are caused by the concavity and convexity of the curve data. The heating stage is a convex curve, where the temperature rise becomes slower with proximity to the peak temperature. Thus, most data lie in the lower temperature region and the skewness is right biased. In the cooling stage, the curve is a concave curve. The temperature drops slowly in the low temperature region; thus, most of the data is in the low temperature region, and the skewness value is left biased. Because of the opposite behaviors of the thermal responses in the heating and cooling stages, the temperature curve needs to be modified using Eq. (4-15) and Eq. (4-16) before the calculation of the skewness value in the whole stage. The modified skewness plots of different depths at different stages are shown in Figure 4-14 (b). The skewness values in both the heating and cooling stages have a positive correlation with defect depth, and the skewness value in the whole stage shows a linear relationship with the defect depth [173].

4.2.6 Skewness feature on nature cracks

The previous section clarified the relationships between crack location, depth and skewness distribution (skewness peak value S_p , valley value S_v). This section considers a natural crack which is an RCF on a rail track head.



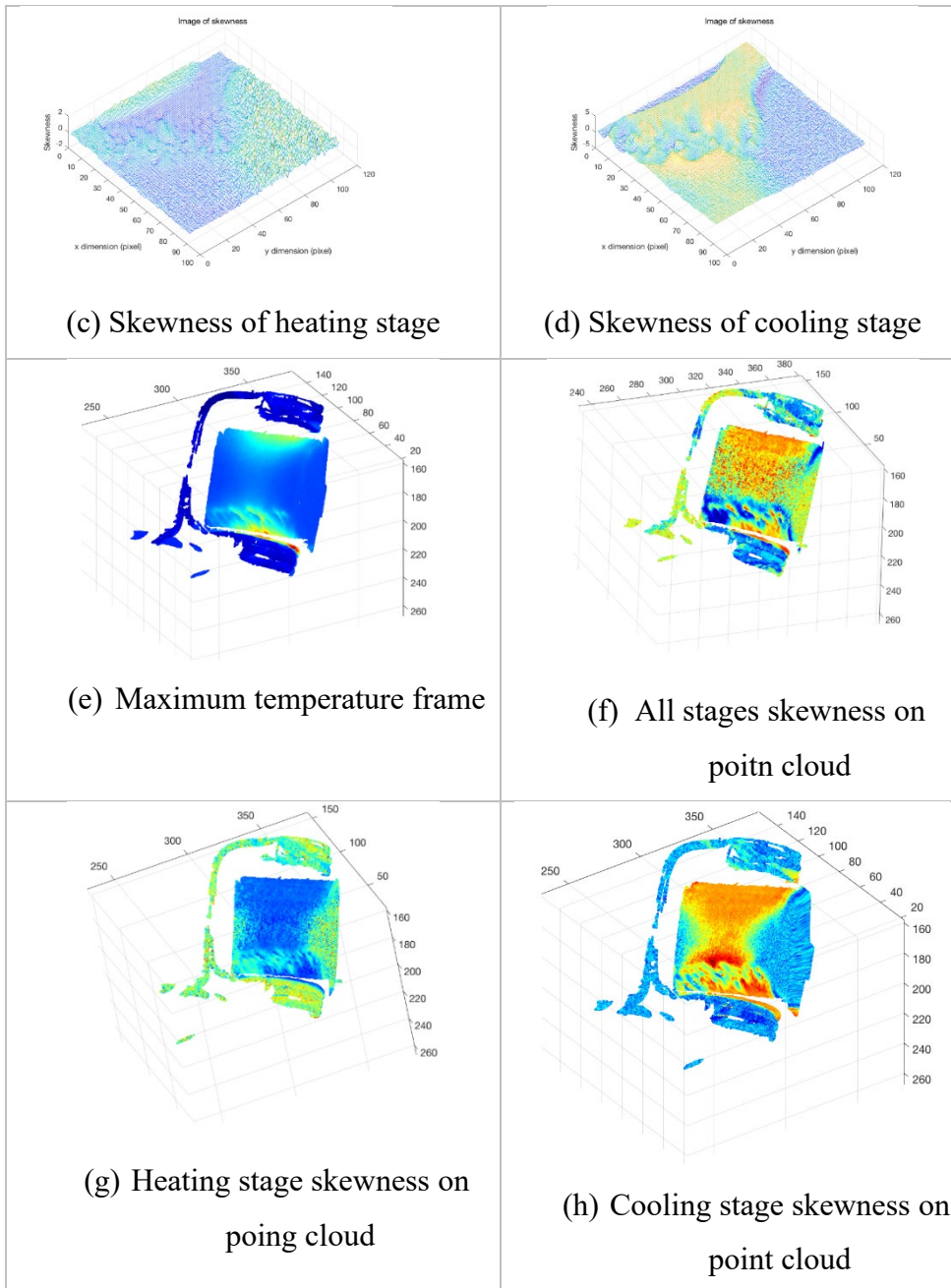


Figure 4-15 Skewness feature on rolling contact fatigue

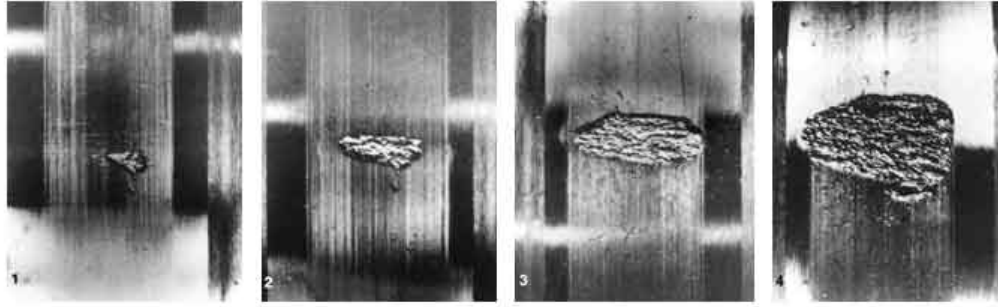
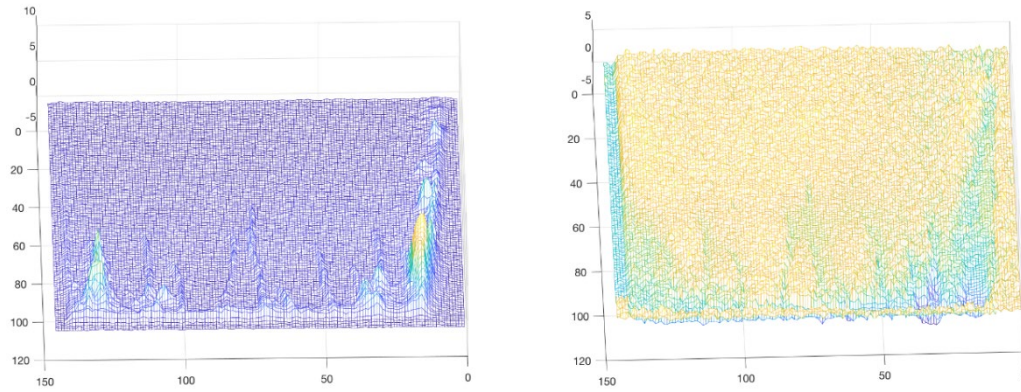


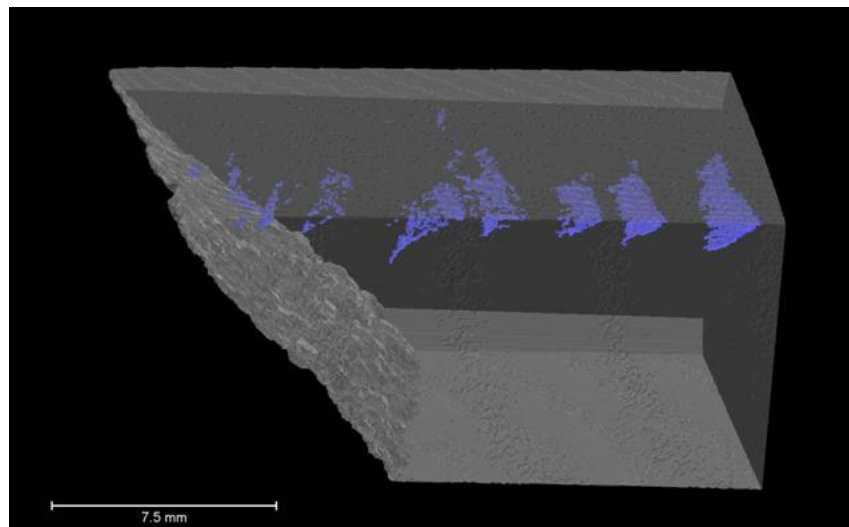
Figure 4-16 Snare, B. (1970), “How Reliable Are Bearings?” *The Ball Bearing Journal*, 162, pp 3–7.

Figure 4-16 shows a typical RCF, where the greatest depth is in the centre of the crack, and the crack narrows on the left and right sides. However, because of the skin effect, the eddy current tends to gather at the edges. The left and right sides have a higher temperature compared to the centre area. Considering this issue, the feature should be more robust to the effect of eddy current density.

Skewness is a ‘shape feature’ that analyses the data distribution. As discussed in Section 4.4, the skewness feature is independent of the skin effect and positions to the excitation which is of significant importance to the RCF crack deflection and quantification. Figure 4-15 (a) shows the maximum temperature frame in the crack area. The maximum temperature strongly depends on the spatial position (crack position and distance to the coil). Figure 4-15 (b) is the skewness distribution in all stages in ECPT experiment. When this was analysed together with Figure 4-15 (a), it was found that the skewness feature shows little dependence on the crack spatial position and the maximum temperature. The valley area shows the crack position. Figure 4-15 (c), and (d) show the skewness values in the heating stage, and cooling stage respectively. In the heating stage, the peak skewness shows the crack location, whereas in the cooling stage, the valley skewness shows the crack location. From the three skewness images it can be found that in each stage (heating and cooling), the skewness feature distributions are identical to each other in terms of the crack position.



(a) Maximum temperature feature visualization (b) Skew feature visualization differential to enhance the contrast and mind the color bar for features



(c) X-ray 3D tomography

Figure 4-17 Skewness of RCF slides and X-ray 3D tomography

Finally, the skewness sample is validated through a nature RCF sample and compared with X-ray tomography. The induction heater used was the EASYHEAT 224 from Cheltenham Induction Heating. A planner rectangle coil was used. The thermal IR camera used was the FLIR A655sc. A maximum frame rate of 200 Hz was used for thermal image capturing. The recording time was 1000 ms with a heating pulse of 200ms. To obtain the appropriate ROI of the RCF sample, a $2.9\times$ close-up lens was mounted on the standard lens. The root mean square (RMS) current density used in the induction heater was 300A, and the current frequency is 262

kHz. The sample used was a rail track with an RCF. This specimen was removed from a PD3 (60km/m) rail track. The sample had the same material property, with its carbon level slightly different but within the range of 0.7% to 0.8%. Figure 4-17 (a) shows the maximum temperature frame; Figure 4-17 (b) illustrates the skewness feature of all stages. Finally, Figure 4-17 (c) is the X-ray 3D tomography on the RCF cut-off sample. The X-ray 3D tomography depth and position are consistent with the skewness mesh plot, which validates that skewness can be well used in natural cracks.

4.3 Thermal 3D gradient features and augmented reality for 3D visualization

4.3.1 The 3D thermal gradient feature

After 3D thermal mapping, quantitative defect evaluation and localization can be conducted based on the 3D heat flow. Time and the spatial thermal gradient in 3D are used for defect detection and localization. Local gradient features are used for localization of defects on a 3D geometry. The thermal gradient is a physical quantification that describes in which direction and rate of heat propagate. The heat gradient in the space domain indicates the heat discontinuity, which suggests a crack or defect presents. It gives a more accurate measurement gradient both in time and space in compared with a 2D gradient.

To validate the point made above, a man-made sample with an angular crack is investigated. Figures 4-18 (a) and (g) show the thermal image of the crack at the heating and cooling stages, respectively. As can be seen, both in the heat pattern and cooling stage, the thermal pattern is blurred, and the line slot shape is barely visible. The time differential of heat is governed by

$$\Delta T = \frac{\lambda}{\rho c_p} \left(\frac{\partial^2 T}{\partial x^2} + \frac{\partial^2 T}{\partial y^2} + \frac{\partial^2 T}{\partial z^2} \right) + \frac{1}{\rho c_p} (q(x, y, z)) \quad 4-17$$

where ΔT is the temperature change. ρ , C_p and λ are the material density, heat capacity and thermal conductivity, respectively; $q(x, y, z, t)$ is the unit internal heat generation caused by the eddy current; T is the heat diffusion; and (x, y, z) are the Euclidean coordinates. During the cooling stage, the term $q(x, y, z, t)$ does not exist. Figures 4-18 (b) and (h) show the first time-differential image of a man-made crack, where the line slot shape is still not preserved. However, the experimental study reveals that only using $\frac{\partial^2 T}{\partial x^2} + \frac{\partial^2 T}{\partial y^2}$ instead of the whole $\frac{\lambda}{\rho C_p} \left(\frac{\partial^2 T}{\partial x^2} + \frac{\partial^2 T}{\partial y^2} + \frac{\partial^2 T}{\partial z^2} \right) + \frac{1}{\rho C_p} q(x, y, z)$ better preserves of defect line, as shown in Figures 4-18 (c) and (i). Here, the time interval $\Delta T = 10ms$.

Finally, Figures 4-18 (d) and (j) show the rail track thermal image in the heating and cooling stages. The time differential images are shown in Figures 4-18 (e) and (k), and the rail track sample images in the second differential gradient are shown in Figures 4-18 (f) and (l). The study on natural cracks also reveals that the surface thermal gradient is better than the time gradient.

Man-made slot sample (heating stage)			Rail track rolling contact fatigue (heating stage)		
Thermal image (man-made sample heating stage)	$\frac{\Delta T}{\rho C_p} \left(\frac{\lambda}{\rho C_p} \left(\frac{\partial^2 T}{\partial x^2} + \frac{\partial^2 T}{\partial y^2} + \frac{\partial^2 T}{\partial z^2} \right) + \frac{1}{\rho C_p} q(x, y, z) \right) \quad (10)$	$G(x, y) = \frac{\partial^2 T}{\partial x^2} + \frac{\partial^2 T}{\partial y^2} \quad (11)$	Thermal image (rail track sample heating stage)	$\frac{\Delta T}{\rho C_p} \left(\frac{\lambda}{\rho C_p} \left(\frac{\partial^2 T}{\partial x^2} + \frac{\partial^2 T}{\partial y^2} + \frac{\partial^2 T}{\partial z^2} \right) + \frac{1}{\rho C_p} q(x, y, z) \right) \quad (10)$	$G(x, y) = \frac{\partial^2 T}{\partial x^2} + \frac{\partial^2 T}{\partial y^2} \quad (11)$
(a)	(b)	(c)	(d)	(e)	(f)
Artificial slot sample (cooling stage)			Rail track rolling contact fatigue (cooling stage)		

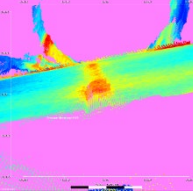
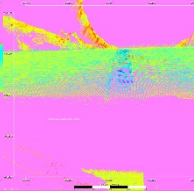
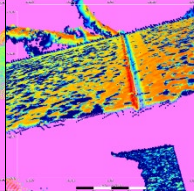
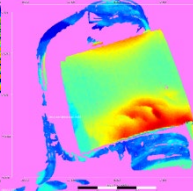
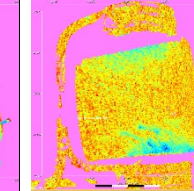
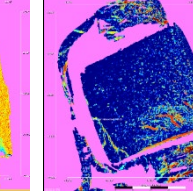
Thermal image (man-made sample cooling stage)	$\Delta T = \frac{\lambda}{\rho C_p} \left(\frac{\partial^2 T}{\partial x^2} + \frac{\partial^2 T}{\partial y^2} + \frac{\partial^2 T}{\partial z^2} \right)$ (12)	$G(x, y) = \frac{\partial^2 T}{\partial x^2} + \frac{\partial^2 T}{\partial y^2}$ (11)	Thermal image (rail track sample heating stage)	$\Delta T = \frac{\lambda}{\rho C_p} \left(\frac{\partial^2 T}{\partial x^2} + \frac{\partial^2 T}{\partial y^2} + \frac{\partial^2 T}{\partial z^2} \right)$ (10)	$G(x, y) = \frac{\partial^2 T}{\partial x^2} + \frac{\partial^2 T}{\partial y^2}$ (12)
					
(g)	(h)	(i)	(j)	(k)	(l)

Figure 4-18 Three-dimensional gradient and defects

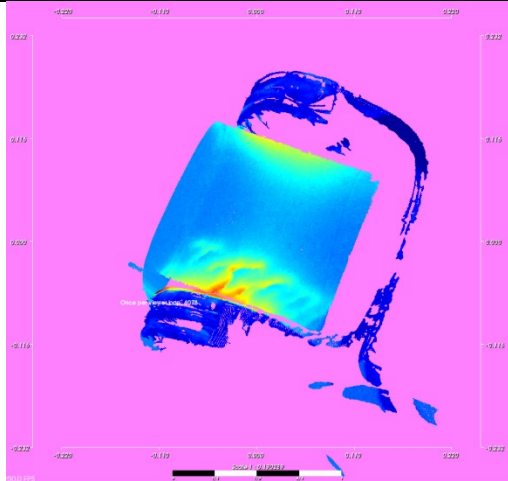
4.3.2 Magnetic field and thermal point cloud fusion.

In the ECPT experiment, the uneven magnetic excitation causes an uneven heating effect on the sample, which brings difficulties in localization and quantification of defects. With 3D thermography, the distance to the excitation coil can be calculated from the point cloud, which brings the possibility of calculating the magnetic field.

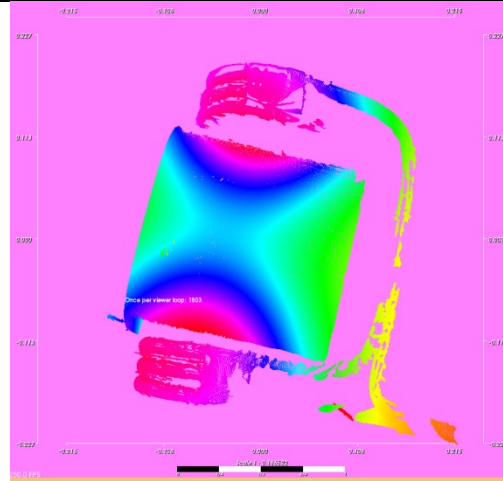
In this case study, the magnetic field was roughly estimated via the Biot–Savart Law with a Helmholtz coil:

$$B(z) = \frac{\mu_0 I R^2 N}{2(R^2 + Z^2)^{3/2}} \quad (4-18)$$

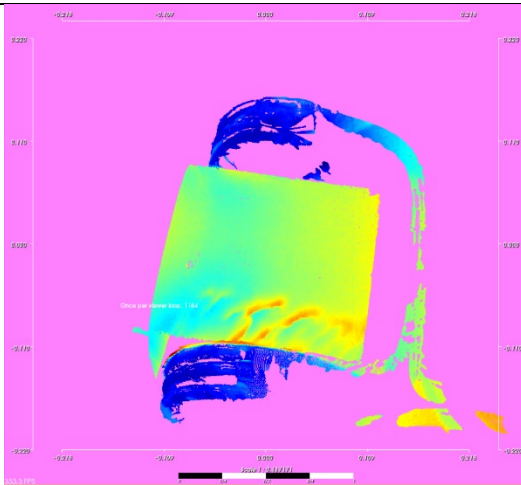
Here, B is the induced magnetic field, R is the radius of the coil, N is the number of coils and Z is the distance to the coil.



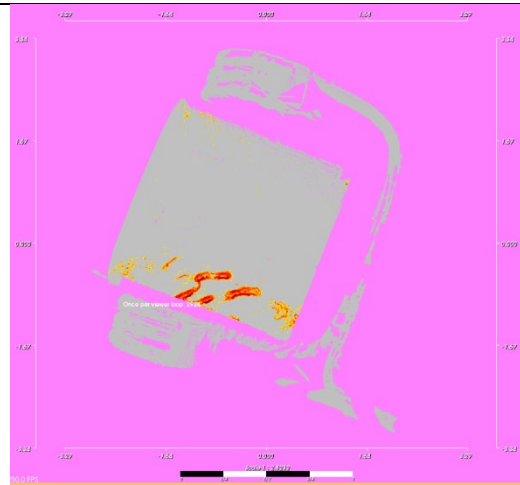
(a) Original thermal point cloud on maximum temperature frame (David)



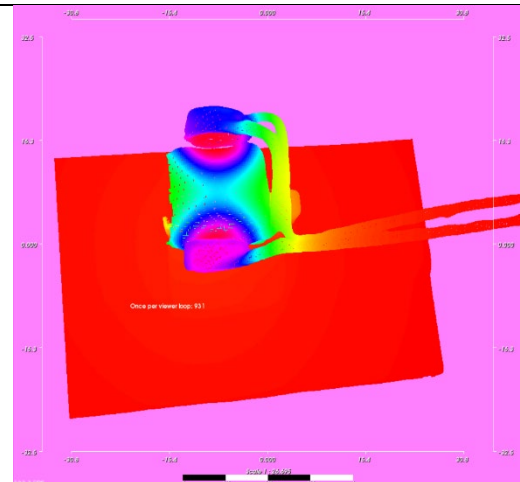
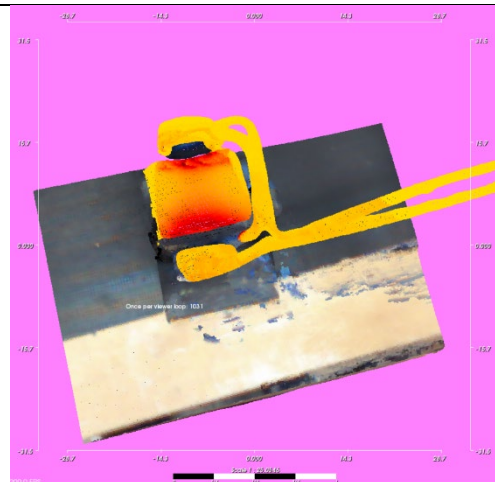
(b) Magnetic field mask (David)



(c) Fusion image (David)



(d) Separated defects (David)



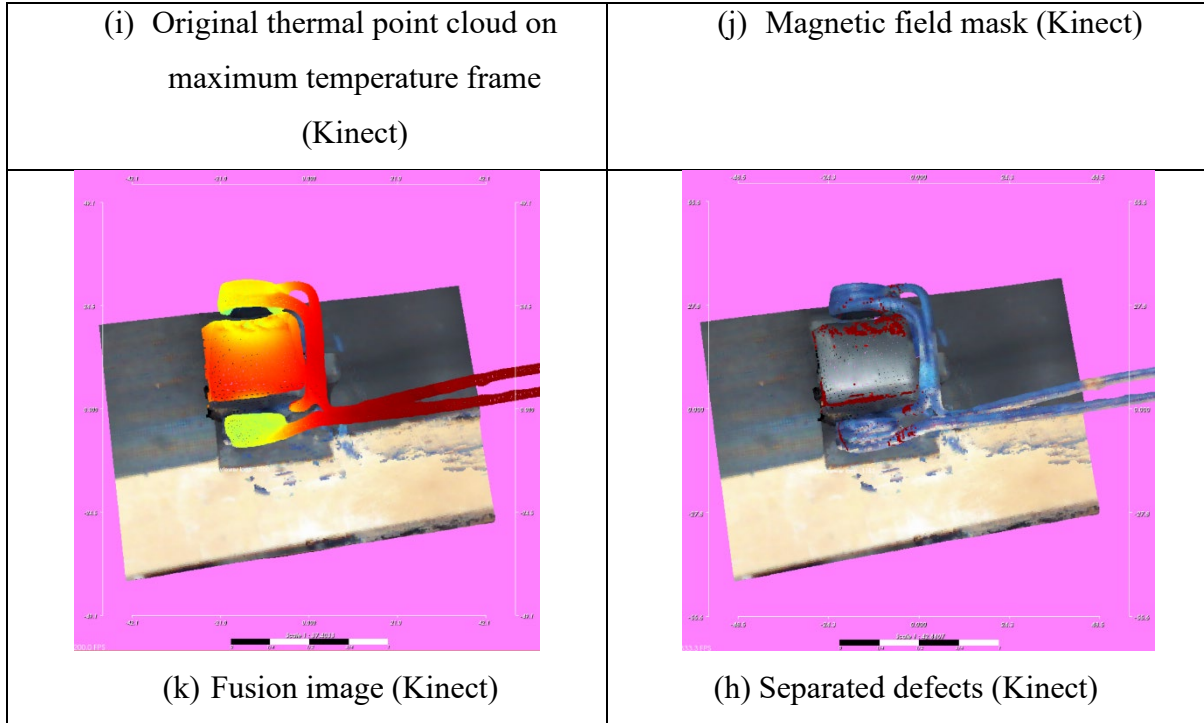


Figure 4-19 Defect location and enhancement using fusion with magnetic field

Two 3D scanners, the Kinect system and David system, were used. Figures 4-19 (a-d) depicts the thermal point clouds acquired by David 3D system, whereas Figures 4-19 (e-h) illustrates the thermal point clouds acquired by the Kinect system.

Comparing Figure 4-19 (b) with (a) and (f) with (h), it is found that the general heat distribution is identical to the estimated magnetic field. Thus, the estimated magnetic field can be used as background removal coefficients as follows:

$$Magnetic\ field\ mask = \frac{magnetic\ field - \min(magnetic\ field)}{\max(magnetic\ field) - \min(magnetic\ field)} \quad (4-19)$$

$$Fusion\ image = \frac{Thermal\ temperature}{1 + Magnetic\ field\ mask} \quad (4-20)$$

The fusion images are shown in Figure 4-19 (c) and (g). Comparing Figure 4-19 (c) with (a) and Figure 4-19 (g) with (e), the fusion image has a much more uniform heat distribution. The defect is also enhanced. Figures 4-19 (d) and 4-19 (h) show the localized defects by using edge extraction from Figure 4-19 (c) and (g).

4.4 Summary

In this chapter, case studies on 3D ECPT were presented based on the three following aspects:

- Geometry level: This included the curvature information, whereby the normal vectors were extracted. The normal vectors were then used for the point cloud segmentation. The RCF only appeared at the shoulder of the testing sample, and the ROI was automatically located using normal vectors.
- Local area feature: The 3D thermal gradient was calculated. One man-made sample and one natural crack were tested. The experimental results revealed that the magnitude of the second-order contains the depth information and can localize defects. Thus, the 3D thermal gradient is a significant parameter for analyzing the defect characteristics in the thermal transient response and evaluating the defect depth.
- Pattern area feature: This presented skewness feature. In this study, the skewness feature was proposed to measure the asymmetry of the thermal temperature response data in the cooling and heating stages. The key idea was that the defect area causes an abnormal thermal transient response in the defect and surrounding area. The aim was to find a feature that could describe and quantify the abnormal transient thermal response caused by the crack. Thus, the skewness feature was proposed in this study to measure the transient thermal response data's asymmetry. The skewness feature on the man-made sample was first investigated to assess the relationship between the skewness feature and the depth of the crack. The artificial cracks of 3 mm, 2.5 mm, 2 mm, 1.5 mm, 1 mm, and 0.5 mm were tested. The experimental results showed that the skewness feature has a monotonic relationship with defect depth. In addition, the skewness was discussed and compared in terms of three stages—heating, cooling and all stages. Finally, a natural crack experiment is conducted and validated via the X-ray scanning.

5 THERMAL TOMOGRAPHIC RECONSTRUCTION FOR 3D EDDY CURRENT PULSED THERMOGRAPHY

In the previous chapter, the skewness feature of the ECPT thermal response is proofed as a linear feature related to the crack depth. The depth estimation and visualization based on the skewness feature are studied in Chapter 4. This chapter firstly proposes the thermal tomographic reconstruction using the 3D ECPT system. The tomographic reconstruction gives a much higher standard of defect characterization in allowing slicing the material in several layers where the skewness depth visualization can be treated as the deepest defect layer (or main defect layer) to some extent. Defects in different layers are estimated and visualized in 3D point cloud. Section 5.1 gives an introduction of thermal tomography as well as other tomography research such as X-ray tomography; 5.2 gives the concept of time-spatial images which is firstly proposed in the work. The time-spatial image is the basis of the tomographic reconstruction. In addition, a tomographic reconstruction based on the differential time square root of temperature drop (DTSTD) signal is presented in 5.2; Section 5.3 applies the thermographic signal reconstruction (TSR) technique for our ECPT's tomography. The time-of-flight model is added to the original log-log polynomial equation in order to form the slices of the tomographic image; Section 5.4 gives a comparison of the DTSTD based thermal tomography, the TSR based thermal tomography and the skewness feature for QNDE with summary.

5.1 Introduction

The eddy current pulsed thermography (ECPT) is well used for defects detection, especially surface crack or corrosion detection and evaluation in conductive material. The infrared image sequence indicates the thermal distribution and heat diffusion process [84]. In the ECPT experiment, the transient thermal response of ECPT contains rich information on the crack characteristics. Previous work has well studied the features for cracks detection

and characterization from the pixel level features [86], local area features [85] to the pattern level features such as Principal Component Analysis (PCA) and Independent Component Analysis (ICA) [83]. These works provide qualitative evaluation of the characteristics of the defect. Based on these works, a recent study [164] discussed feature-based quantitative relationships of defect size (depth and length) and their thermal responses.

Alternative to feature-based QNDE for ECPT images, in Ref. [165] electrical and thermal conductivities are estimated by the early experimental transient response of the first layer having a visible fibre orientation. Then, an iterative inverse procedure minimizes the discrepancy between measured and simulated data to reconstruct orientations of each layer using the estimated conductivity. However, no work up until now has discussed geometry of under surface cracks. This work proposes a novel approach to reconstruct 3D images and to evaluate the morphological localization of subsurface cracks based on 2D thermal slices. The differential time square root (sqrt) of the temperature drop (DTSTD) is extracted to characterize the shape of the subsurface crack along with the crack sizing and depths, and validated.

With the recent advancement of NDT in 3D reconstruction based tomographic approaches for internal and sub-surface defects, the qualitative and quantitative analysis of RCF types and shapes becomes a crucial and urgent task. In contrast to conventional approaches, the X-ray based CT shows better resolution results and defect depth estimations. The different case studies of the use of X-ray CT for NDT have been proposed in [166]. The X-ray based CT has good results for depth estimation in NDT problems. However, the equipment is expensive and bulky along with the risk of radiation effects if continuously used. Also, the x-ray is hard to penetrate the entire rail, which makes it hard to use X-ray CT for online inspection of RCF cracks. The high-energy industrial CT (above 4 MeV) could penetrate the entire rail track head. However, the higher the energy of the X-ray, the lower the resolution (for 4MeV, the resolution is 1 mm), which makes it impossible to identify the RCF cracks in the rails. For the ultrasonic approach, Daigle et al. [167] use an ultrasound-based 3D tomography approach for NDE of concrete structures.

Computed tomography is a well-established approach used to reconstruct cross-sectional slices through an object from the transmitted projection images taken as a function of angle around a single axis of rotation. In [168], the authors carry out different experiments

using single view cone beam x-ray computed tomography to generate different datasets that can be used for supervised learning. A complete data reconstruction model is also presented. In [169], the single view based computed tomography has been proposed. This approach has high-speed inspection but a limited data acquisition time. Also, the generated tomographic sequences suffer from poor image quality and noise. So, to improve the reconstruction quality, different types of reconstruction algorithms are proposed such as AI-based algorithms [170], total variation decomposition algorithm [169], truncated singular value decomposition algorithm [171], and wavelet-based algorithm [168]. The single-side view tomography is a recent and newly developed technique with the help of computing models and AI [170]. These slices can be stacked to produce a 3D image of the object, which can then be visualized by one of several methods, including volume rendering or digital slicing through the sample along any arbitrary plane [168,169]. These tomography techniques also boosted the development of the thermal tomographic reconstruction and motivated the tomographic reconstruction of the 3D ECPT system.

5.2 Thermal behaviours of 3D ECPT, time-spatial image and DTSTD signal

The tomographic reconstruction is based on emitting signals that can penetrate the material and go through or fold back to the receiver. These signals include X-ray, ultrasonic, magnetic field and thermal wave, which are called X-ray computed tomography (XCT), ultrasonic tomography, magnetic resonance imaging (MRI) or nuclear magnetic resonance (NMI) and thermal tomography respectively. The research and applications on X-ray tomography are diverse and extensive. However, there are few applications on thermal tomography because the heat propagates not only vertically, but also horizontally. This thermal property not only gives harsh challenges in backward reconstructing tomography layers, but also make the thermal images blurred in nature. For this reason, a proper exciting heat source has to be selected that can maximize the thermal image contrast between defective region and non-defective region, while minimize the thermal flux propagation in the vertical direction. The ECPT has the advantage that the most thermal energy gathers in the crack region, which maximizes the thermal contrast. In this work, the Helmholtz coil is used because of its relative uniform magnetic field and relative uniform thermal wave in the

horizontal direction. Thus, the ECPT system with Helmholtz coil is selected for the thermal tomography study.

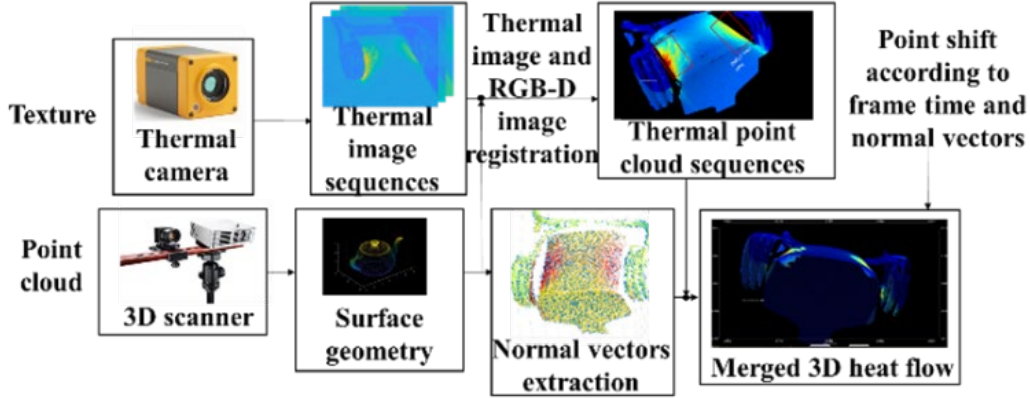


Figure 5-1 Procedures for the reconstruction and validation of the DTSTD based thermal tomography for artificial and natural defects

Figure 5-1 shows the visualization pipeline. The 3D thermal fusion has already been provided in section 3.1. The normal vector needs to be extracted from the surface in order to show the temperature response in different time slots and reconstruct the time-spatial image. The normal vector extraction is provided in section 4.1.

After the pulsed induction heating, only the heat conduction in steel is considered for heat flux propagation in the cooling stage because the thermal conductivity in air gap ($0.023 \text{ W/m} \cdot \text{K}$) is far less than it is in the steel ($\sim 47 \text{ W/m} \cdot \text{K}$). The speed of heat penetration is given as

$$d_{heat} = 2\sqrt{kt} \quad (5-1)$$

where k is the thermal diffusivity and t is the elapsed time. For the steel material, the heat penetrates up to 5~7 mm in one second.

The normal vector of the 3D surface at (x_0, y_0, z_0) is denoted as $\vec{N}_P = (n_{x_0}, n_{y_0}, n_{z_0})$. The 3D thermal image sequences provide both time information and temperature information as $(x, y, z, \text{temperature}, \text{time})$. The time-spatial image is reconstructed with the normal vectors adding the the 3D thermal image sequences where

$$P_{T=a^\circ\text{C}} = \begin{bmatrix} x(x_0, t) \\ y(y_0, t) \\ z(z_0, t) \end{bmatrix} = \begin{bmatrix} x_0 \\ y_0 \\ z_0 \end{bmatrix} + 2\sqrt{kt_{(x_0, y_0, z_0, T=a^\circ\text{C})}} \begin{bmatrix} n_{x_0} \\ n_{y_0} \\ n_{z_0} \end{bmatrix} \quad (5-2)$$

In Eq. (5-1), (x_0, y_0, z_0) is the 3D thermal points location in the surface layer. The surface layer cloud is denoted in vector form $\vec{T}_0 = (x_0, y_0, z_0, t_0)$ where t_0 is the start time of the heat flux propagation. $t_{(x_0, y_0, z_0, T=a^\circ\text{C})}$ is the elapsed time reaching to cut-off temperature level $a^\circ\text{C}$ at the location (x_0, y_0, z_0) . $n_{x_0}, n_{y_0}, n_{z_0}$ is the surface normal vector position at surface point (x_0, y_0, z_0) . $(x_{(x_0, t)}, y_{(y_0, t)}, z_{(z_0, t)})$ is the new point location at time t shifted on the surface location (x_0, y_0, z_0) . k is the thermal diffusivity.

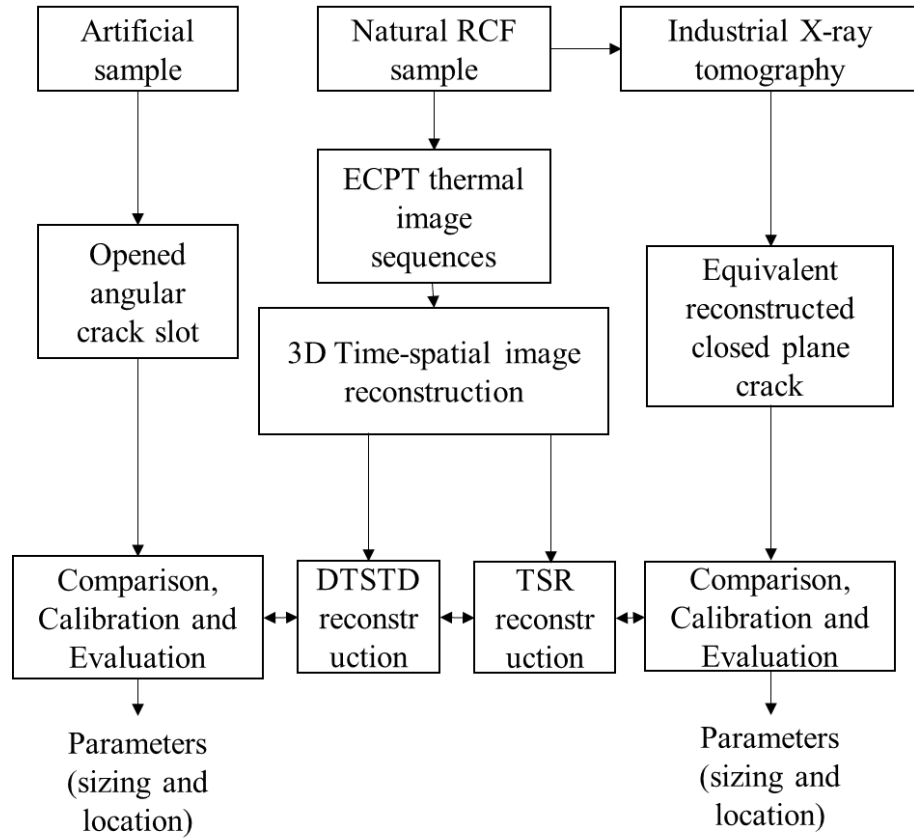


Figure 5-2 Sketch diagram of tomography study on 3D ECPT

Figure 5-2 shows the sketch diagram of the tomography study. In this study, both the artificial sample and natural crack sample (rail track head with rolling contact fatigue) are used. The natural RCF sample are tested and compared using X-ray computed tomography.

In the heating stage. The induced eddy current decays exponentially and penetrates to a certain depth. The penetration depth is given as

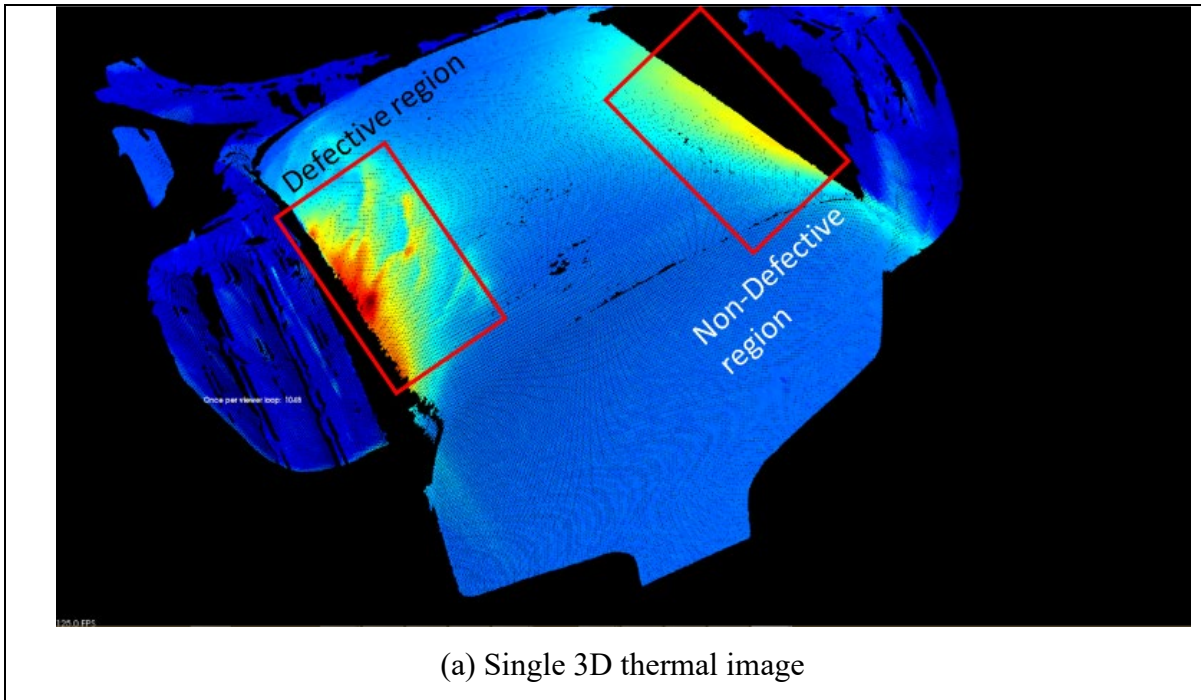
$$\delta = \sqrt{\frac{1}{\pi \sigma \mu \mu_0 \nu}} \quad (5-3)$$

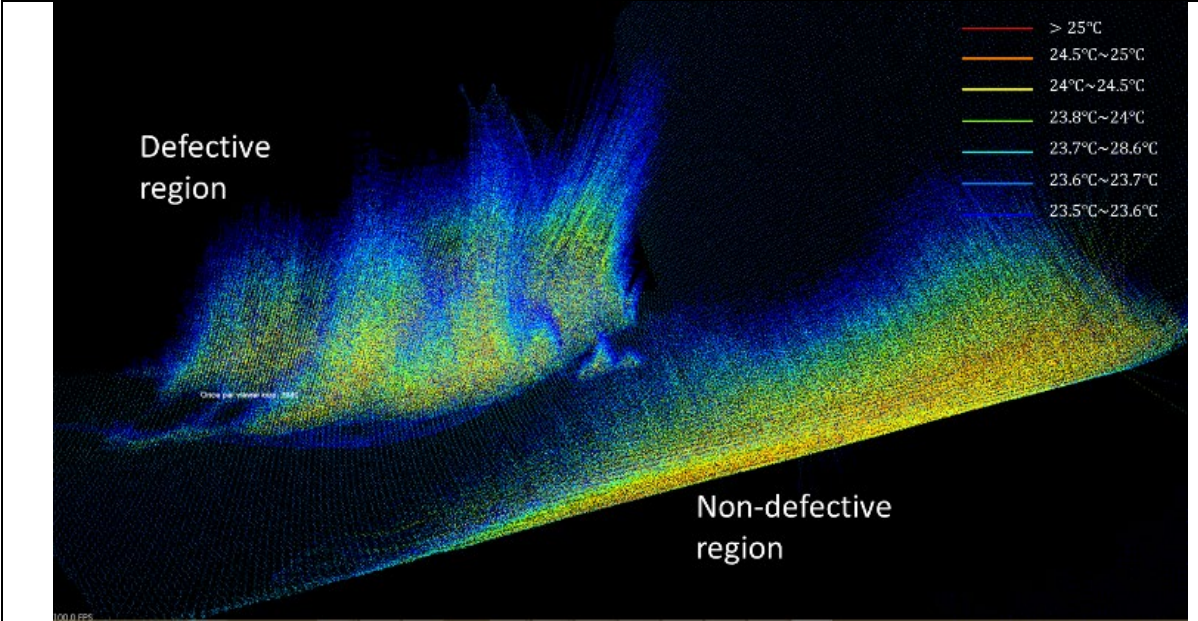
where ν is the frequency of the eddy current, μ and μ_0 are the relative permeability and the permeability of vacuum respectively, σ is the material conductivity. In the heating stage, the current penetration depth is very small. In our experiment, the steel material with an excitation frequency of 200 kHz has a skin depth of only 0.03 mm. Thus the heat energy is only distributed at the surface region. Figure 5-3 (a) is the image taken at the end of the heating stage. The surface cracks are the major factors that cause the thermal discontinuities in this stage.

Figure 5-3 (a) shows the 3D heat distribution at the beginning of the cooling stage. Eq. (5-2) builds the relationship of time and heat penetration depth and shows that the heat penetration depth is proportional to the root square of time and the material thermal diffusivity. For a specimen like a rail track which is constructed of steel, the thermal diffusivity can be treated as constant. Similar to the x-ray computed tomography, Eq. (5-2) shows that the penetration depth is proportional to the square root (sqrt) of elapsed cooling time. Thus this work examines using the sqrt time of temperature drop for depth estimation.

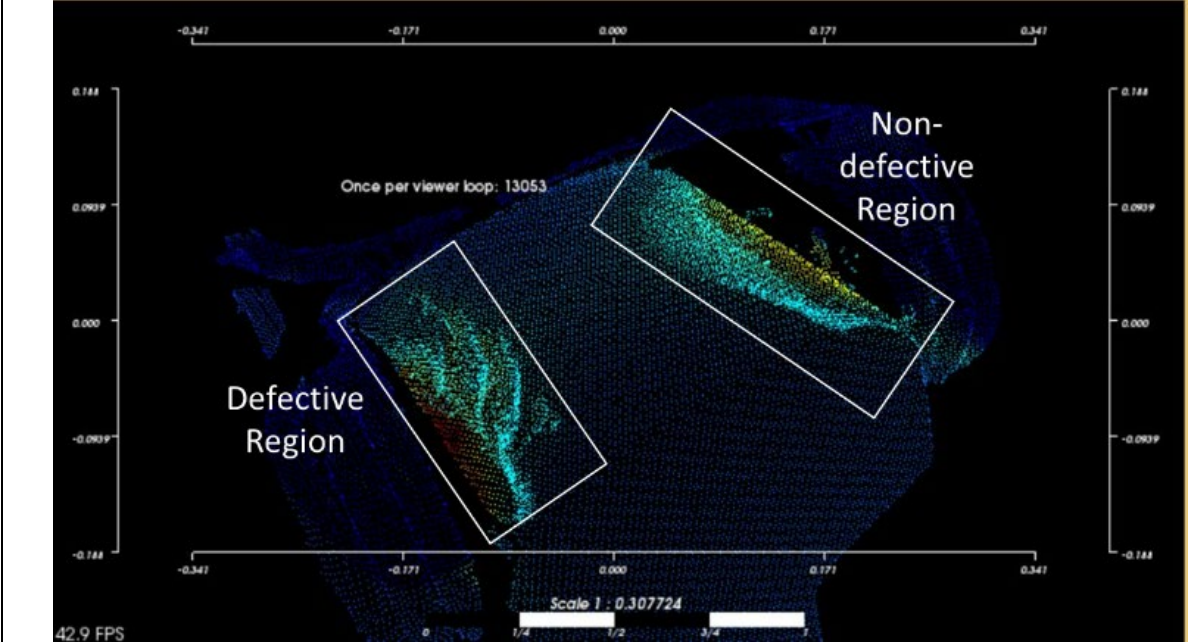
Figures 5-3 (c) and (d) show the visualization of sqrt time drop to the a °C, a=60% temperature drop (mean temperature of the heat flow). In Figures 5-3 (c) and (d), the height of the point cloud leaves the surface is proportional to the square root time of temperature drop, which is also the position where the heat penetrates. Figure 5-3 (c) shows the top view of the 3D sqrt time of the temperature drop image while Figure. 5-3 (d) gives the bottom view. Considering these time images together with Figure 5-3 (a), the 3D thermal distribution in Figure 5-3 (a) shows the thermal patterns of the surface defect distribution since the heat has not penetrated into depth at the beginning of the cooling stage. The major cause of the thermal discontinuity in Figure 5-3 (a) is the high current density in the crack area during the heating stage. Figure 5-3 (b) shows the temperature layers in different colors and the time arrival to this layer is the height to the surface. Figure 5-3 (c) and (d) are the 3D visualization of the time images in a later frame with a cut-off temperature of 70% maximum temperature drop. The cut-off temperature stand for all pixels are in the same temperature level which is 70% of maximum temperature drop. These images use the information in later image sequences where the heat has penetrated into the material at a certain depth. The discontinuity (different time arrival to this temperature level) is mostly caused by the subsurface cracks. The heat penetration depth is calculated using Eq. (5-1).

Figure 5-3 (a) shows the 3D heat flow at the maximum temperature frame (time slot right after the heating stage). The experiment setup is the same illustrated in section 3-1. The Easyheat 224 from Cheltenham Induction Heating is implemented for the coil excitation. The Helmholtz coil with water cooling is selected. The water is pumped through the coil copper tube during the experiment. The excitation frequency is 200 kHz in 300 A. The heat flow is recorded by the FLIR SC7500 which has an In Sb detector of infrared range between 1.5~5 μm . The camera has a pixel resolution of 320×256 and a maximum speed of 383 Hz. The thermal camera utilizes a maximum speed rate of 383Hz. The heating time is 200 ms and the cooling time is 800 ms. The testing sample is a rail track sample with rolling contact fatigues on one side of the rail track shoulder.





(b) 3D Heat flow



(c) 3D sqrt time of temperature drop image (top view)

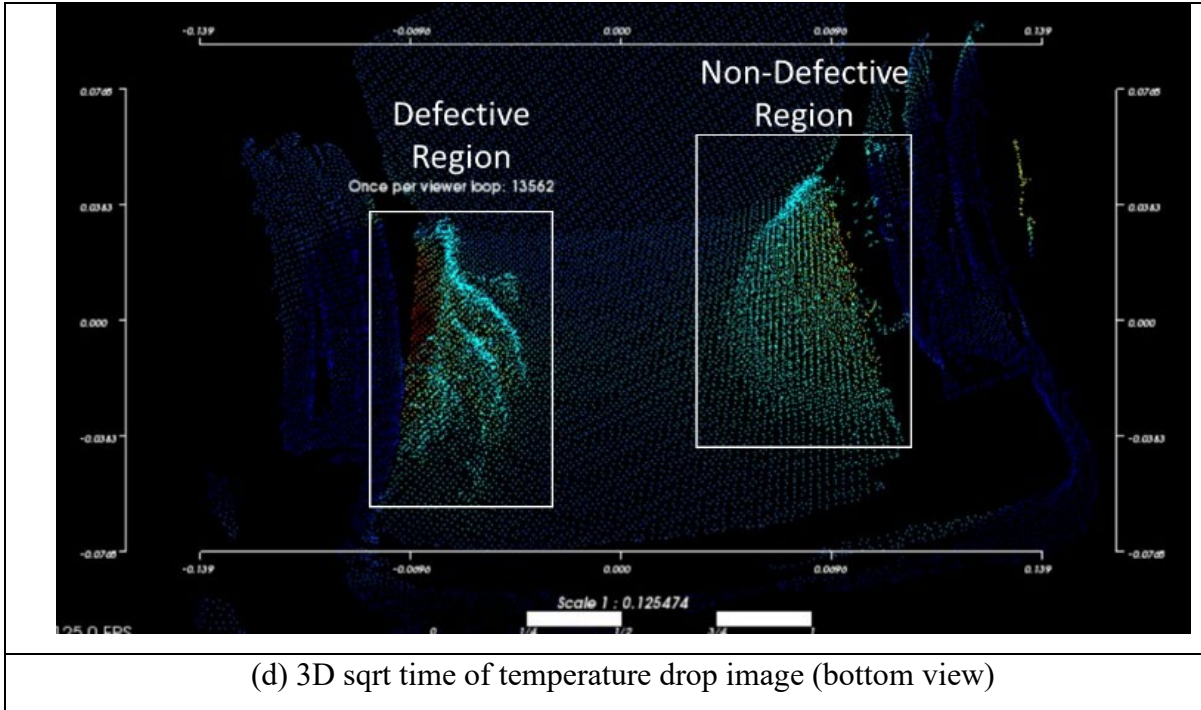


Figure 5-3 Visualization of the 3D heat flow. (a) Single 3D thermal image; (b) 3D Heat flow; (c) 3D sqrt time of temperature drop image (top view); (d) 3D sqrt time of temperature drop image (bottom view)

To enhance the contrast between the defective region and the non-defective region, the point cloud is down-sampled. Using the 3D thermal fusion provided in Figure. 5-1, the fused 3D heat flow is generated and shown in Figure 5-3 (b). This figure merges the 3D heat flow into one single image frame. The fused 3D heat flow in Figure 5-3 (b) presents the following information: (1) The surface temperature distribution at the maximum temperature frame is given at the surface of the rail track; (2) the thermal images in later time slots are placed as plane layers overlay the previous time slots; (3) the images taken at different time slots is visualized in one single 3D image. In this figure, different temperature layers from 10% maximum temperature drop to 80% are marked with a different color, while the height of the layer indicates the time arrival to this temperature (top 10% temperature range and bottom 20% temperature range are ignored due to too much noise information). It could be seen that the defect-free area has a very uniform time arrival shape while the defect area is clustered into several scattered regions.

In addition, the time cost from each layer to the next layer is visualized as the width of

the temperature zoom. A higher time cost of the temperature layer indicates a defect exists in this layer. Using such a system as a base, a thermal tomography system is proposed using the differential square root of temperature drop as pictured in Figure 5-4

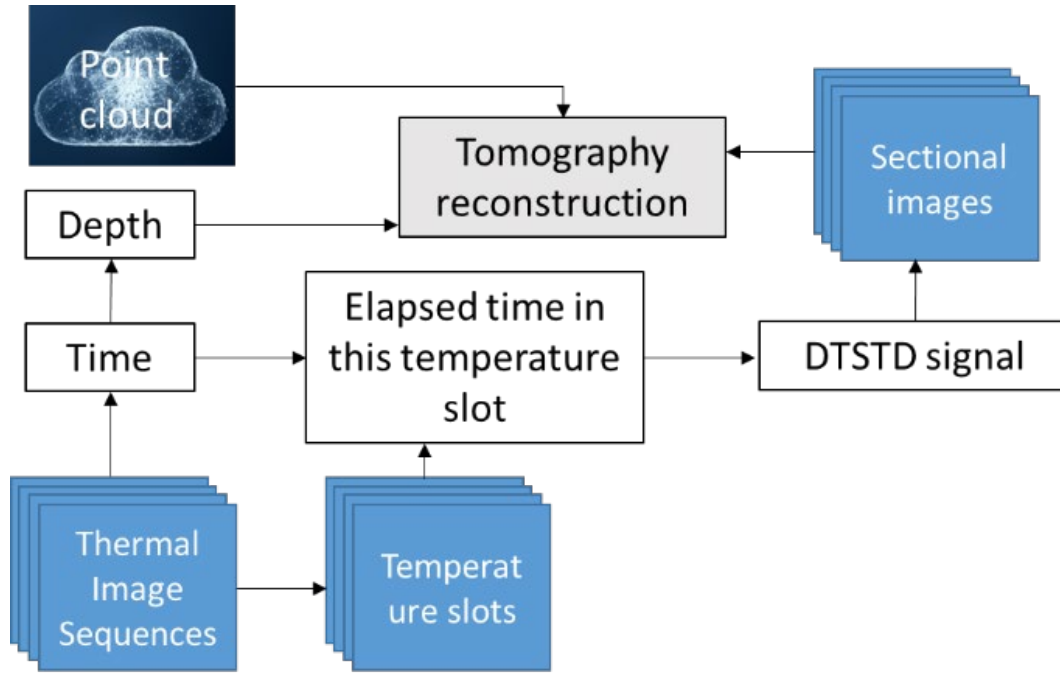


Figure 5-4 Proposed DTSTD algorithm

As for the penetration depth, we found the time relationship and the penetration depth. Theoretically, the more time it cost to reach the temperature level, the higher thermal diffusivity, which reveals one or several cracks exists under the surface. For different temperature layers, a higher time cost to the next temperature level indicates that there exists a discontinuity which blocks the heat transfer. The elapsed time in each temperature layer is used as the response signal for the reconstruction of the sectional images. Figure. 5-5 shows the differential sqrt time of temperature drop images, where

$$R(u,v)_d = \sqrt{T_{a\%^\circ\text{C}}} - \sqrt{T_{b\%^\circ\text{C}}} \quad (5-4)$$

In Eq. (5-4), the $R(u,v)$ is the response signal at a pixel location (u,v) . The subscript d denotes the penetration depth where the heat penetrates to the cut-off temperature $a\%^\circ\text{C}$ temperature drop. The term $T_{a\%^\circ\text{C}}$ is the sqrt temperature drop reaching cut-off temperature $a\%^\circ\text{C}$ and $T_{b\%^\circ\text{C}}$ is the sqrt temperature drop reaching cut-off temperature $b\%^\circ\text{C}$. Figures 5-5 a~g shows the differential sqrt time of temperature drop from the range of 10%

temperature drop to 80%. These time images contain both depth and intensity information of the cracks. For Figure 5-5 (a), firstly, the sqrt of time cost to reach 80% temperature drop is calculated to estimate the heat penetration depth. Secondly, a strong pixel in Figure 5-5 (a) indicates a high time cost from heat level 70% to 80%, which indicates a crack under the current penetration depth.

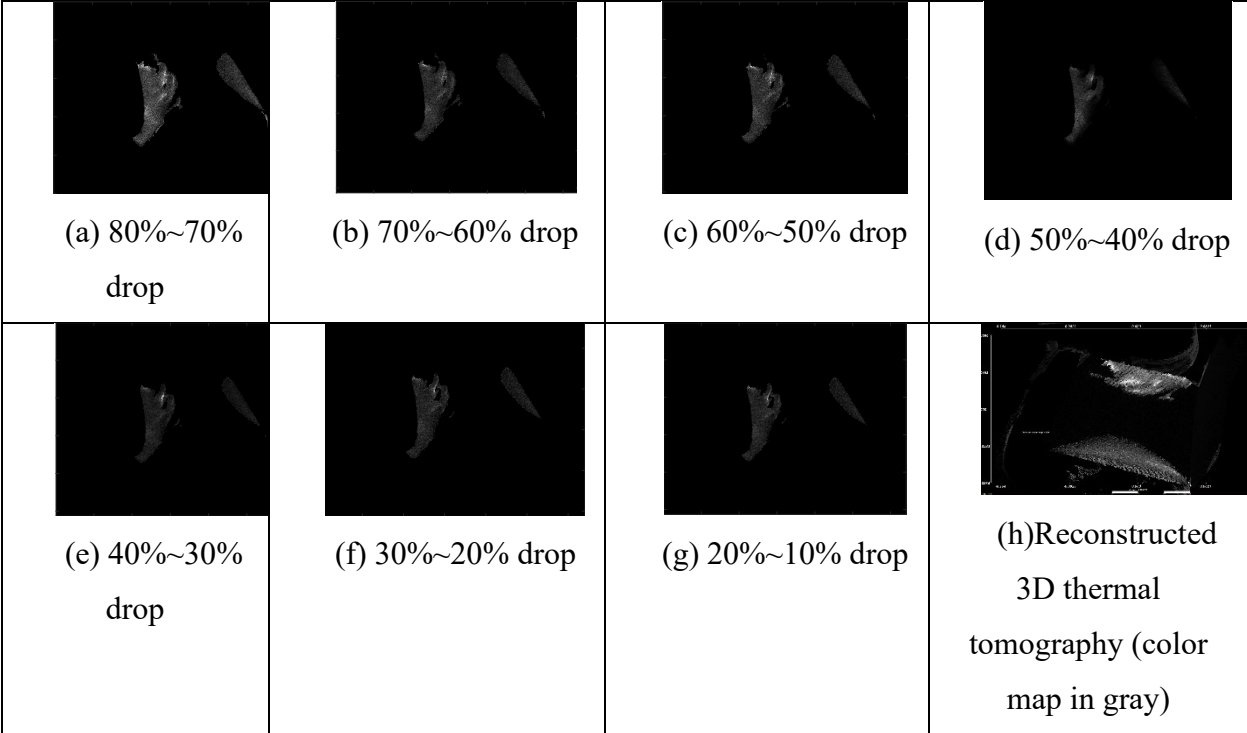


Figure 5-5 Sectional images and the reconstructed 3D thermal tomographic image (top view).

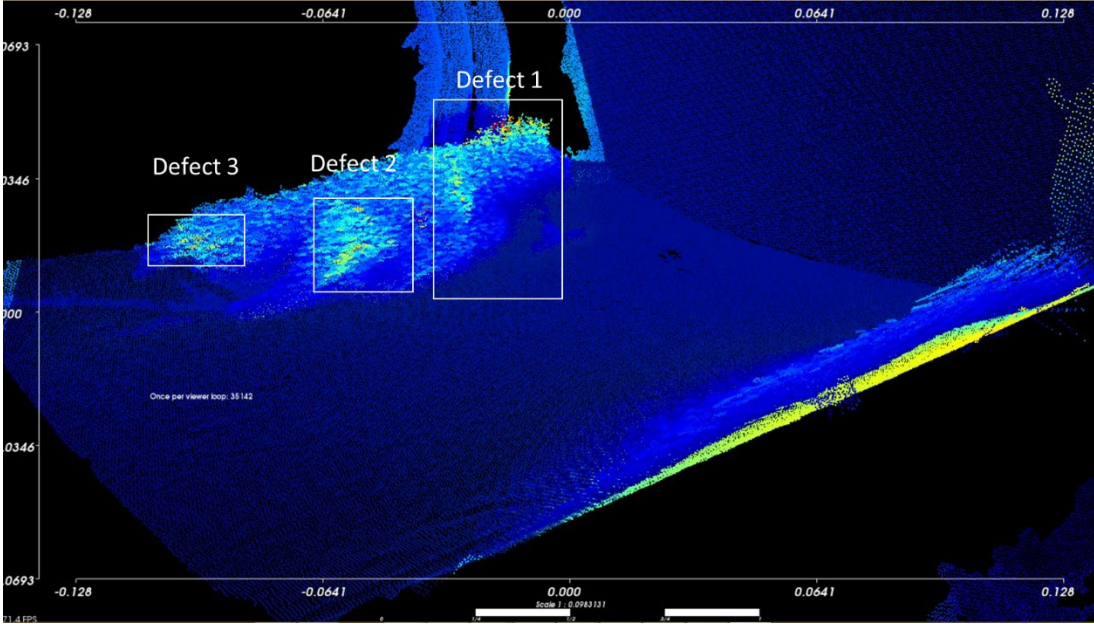


Figure 5-6 Reconstructed 3D thermal tomographic image (color map in jet)

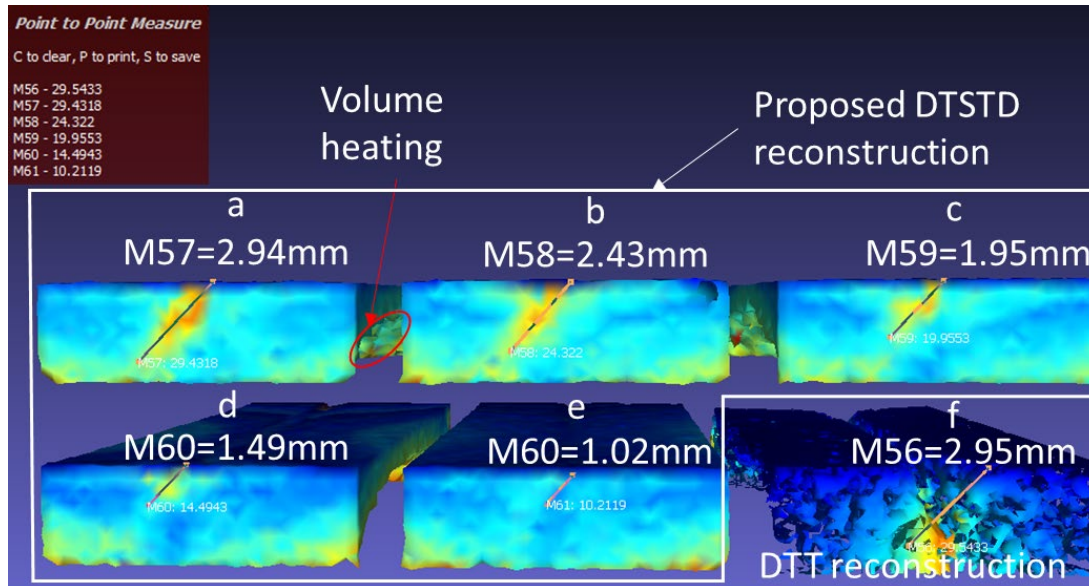


Figure 5-7 Reconstructed artificial angular crack slots under different methods

Same principles as Figure. 5-5 (a) Figures 5-5 (b) to (g) are the differential square root time images at different temperature layers from 80% temperature drop to 10%. Figure 5-5 (a) has the deepest thermal penetration depth since the time to reach the 80% temperature drop is the longest in all image sequences, whereas Figure 5.5 (g) has the least penetration depth for the same reason. From the time-image sequences, it can be seen that the deeper the penetration depth, the more detail and contrast the image has. This observation is opposite to the obtained ECPT thermal image sequences as these thermal images have the highest contrast in early cooling time and become blurred in the later cooling stage. The reason is due to the fact that at the beginning of the cooling stage, the thermal image has the maximum temperature divergence caused by the uneven heating and the higher current density in the defective area. However, the large temperature divergence also results in a quick temperature drop which eventually leads to a small-time interval between each temperature layer. The small-time interval will result in a low resolution of the differential square root time images in Figure 5-5. Thus, the DTSTD sectional images have higher contrast in the later cooling stage and ECPT thermal image sequences have higher contrast at the early cooling stage. Given the intensity images with different time slots (Figures 5.5 (a~g)), the 3D positions with intensities (x, y, z, i) are calculated using Eq. (5-4), where i is the intensity of images Figures 5-5 (a~g) and t is the elapsed time to each temperature level from 10% temperature drop to 70% temperature drop. The reconstructed 3D tomography image is shown in Figure. 5-6.

The dynamic thermal tomography (DDT) technique is the most widespread method for flash thermal tomography in the reconstruction of the defect structure [173]. The DDT reconstruction is also presented for comparison study. In the evident form the thermal effusivity given by $e = \sqrt{\lambda\rho C_p}$ where λ is the thermal conductivity, ρ is the material density and C_p is the material thermal conductivity. The thermal effusivity is to measure the ability of the heat propagation with its surroundings. For a semi-infinite body, the solution of thermal effusivity is given by:

$$e = \frac{W}{T\sqrt{\pi\tau}} \quad (5-5)$$

where W is the absorbed power, T is the surface temperature, τ is the elapsed time. Obviously, the crack region has a much lower thermal effusivity compared with defect-free region. Thus the thermal effusivity is used for the reconstruction of the slice images. Since the absorbed energy is hard to measure in the experiment accurately, the normalized effusivity is used given as:

$$\frac{e}{W} = \frac{1}{T\sqrt{\pi\tau}} \quad (5-6)$$

In this work, the artificial angular crack slot is used with angular cracks from 1mm to 3mm and angle of 45°. The reconstructed tomography image is shown in Figure 5-7. Images A to E are cracks of 1mm to 3mm reconstructed by the proposed DTSTD method. The high intensity voxels (shown as red color) indicate a high DTSTD value. Image F is the 3mm crack reconstructed with reciprocal of the normalized thermal effusivity $\frac{W}{e}$. The stronger the intensity, the lower the effusivity where indicates the defect region. From images A to E, they show a 1.7% measurement error of defect depth and angle where $error = \frac{mean(measured\ depth - real\ depth)}{mean(measured\ depth)}$. The arched structure of the reconstructed image is caused by the even heating and not enough time response in these temperature regions. Comparing with images A and F. The image reconstructed with normalized thermal effusivity also shows the depth and position of the defect. However, the boundary effect is particularly critical as ECPT system is unevenly heated and most energy gathers in the defect region and the area near the excitation coil. The result obtained from artificial cracks shows the proposed method shows better performance in ECPT thermal tomography.

This section validates and reports the comparison of the result from x-ray CT and the proposed thermal tomography approach. As is illustrated previously, the x-ray is hard to penetrate the entire rail track head. In this experiment, the rail track head with RCF is cut with a depth of

9mm. Figure 5-8 (a) is the tomography image of an RCF cut-off sample reconstructed from X-ray CT. Figure 5-8 (b) is the proposed thermal tomography image. From the two images, D5 has the longest length and depth. The defects of D2 to D6 are well-matched with each other. However, For Figure. 5-8 (b), the D1 and D7 are not well reconstructed and show large noise around due to the boundary effect of heat conduction, which shows that the edge effect and thermal propagation at borders should be reconsidered.

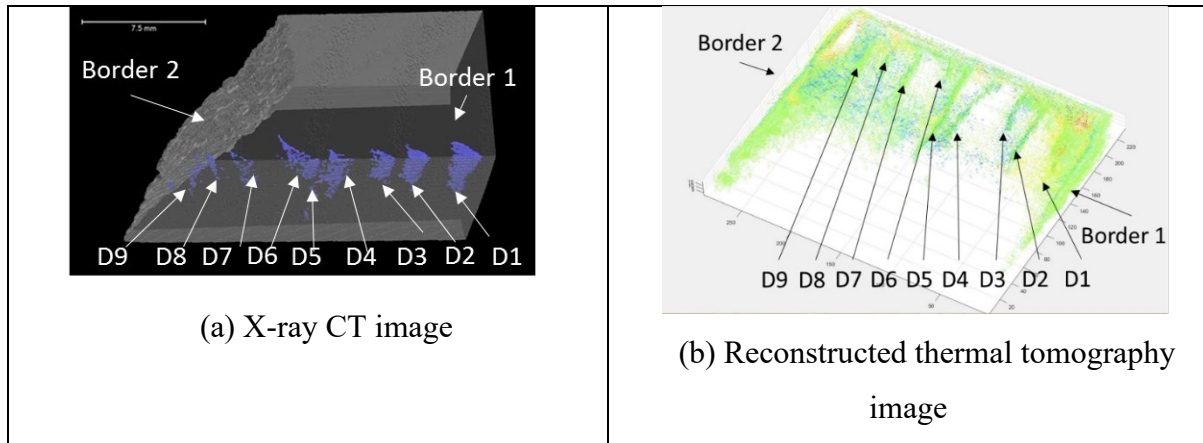
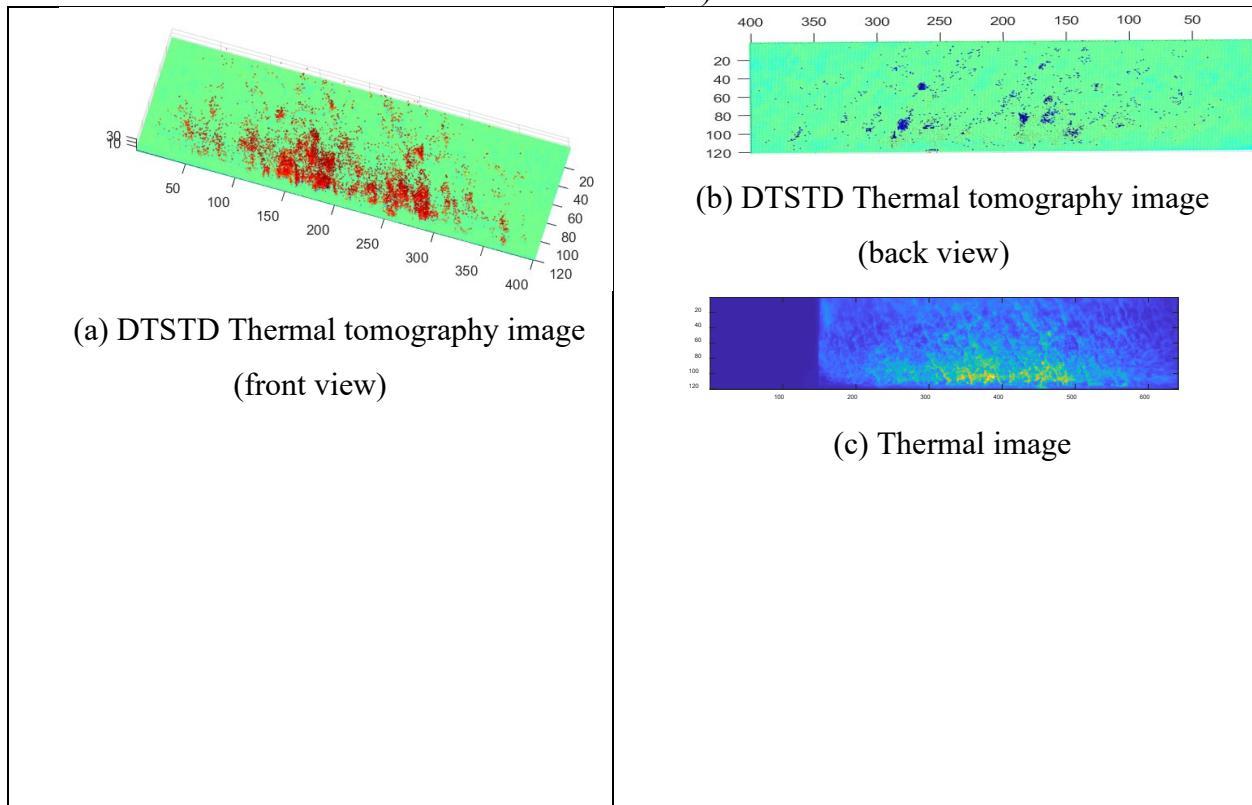


Figure 5-8 X-ray CT image and the proposed thermal tomography image (160 kV microfocus)



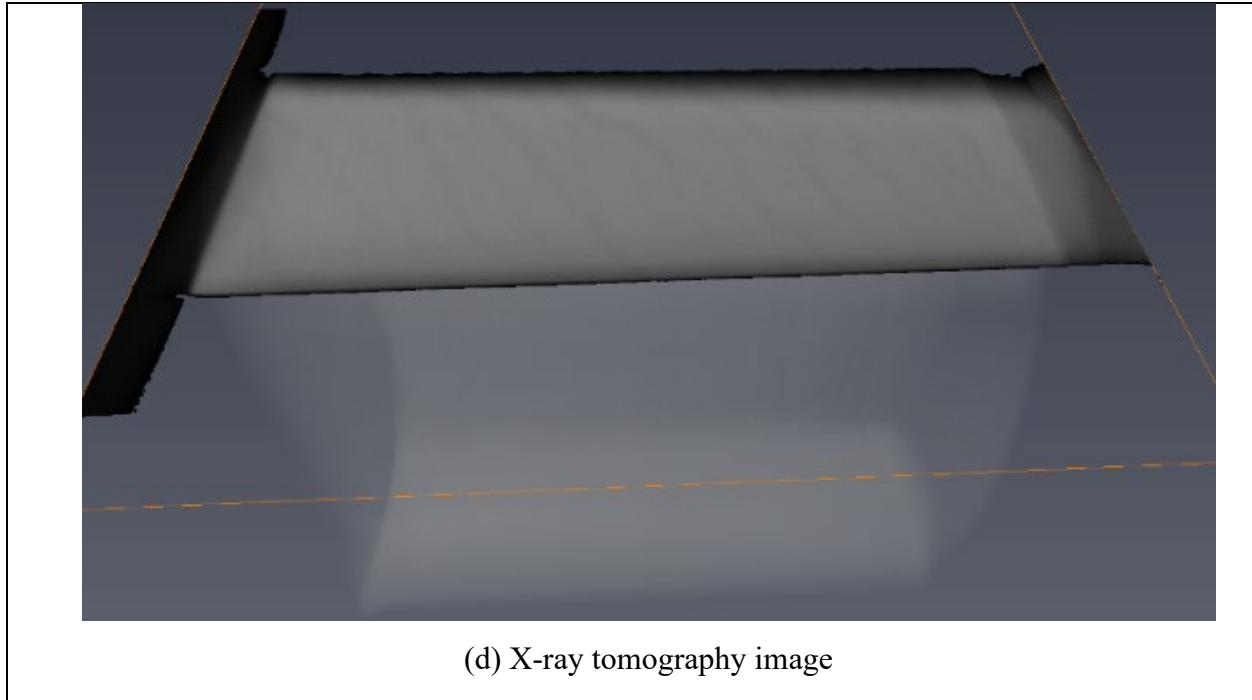


Figure 5-9 X-ray CT image and the proposed thermal tomography image (160 kV microfocus industrial CT)

Figure 5-9 shows another rail track sample with tiny RCF cracks. The Proposed DTSTD thermal tomography image is given in Figures 5-9 (a) and (b). Figure 5-9 (c) is the thermal image and the corresponding X-ray tomography image is shown in Figure 5-9 (d). The excitation coil used is the Helmholtz coil located on the top and bottom side of the sample. The heating time is 200ms with current density of 230A. From the thermal image, uneven heating happens where the bottom side near the coil has larger mean temperature. The effect is also shown in the thermal tomography image as the bottom side has more defect points. Limited by the resolution of the thermal camera, the point cloud of the RCF defect is not very clear. The defect shape and the position from the X-ray tomography have well-matched with the DTSTD thermal tomography, which proves that the DTSTD feature could be used as a domination factor for the thermal tomography reconstruction.

5.3 Thermographic signal reconstruction on ECPT's thermal tomography

The thermographic signal reconstruction (TSR) is considered as one of the most practical and useful technique in active thermography in recent few years. Several studies [175~177] raises the TSR algorithm as a milestone that put the infrared thermography to the level as the most

established NDE technique among other techniques including ultrasonic, magnetic particles, eddy current and X-rays. TSR is originally designed for pulsed thermography. Recent studies [178] also investigated using TSR in long pulsed thermography.

The TSR technique emerges in the early 2000s which is designed to reduce the noise for the detection of smaller and deeper defects. The TSR belongs the category of the curve-fit based analysis. It transforms the thermal response from original time-temperature space to the log-log space. The curve fitting of the log-log curve is then applied and the coefficients of the curve is used as the TSR signal to reconstruct the defect.

The TSR algorithm starts from form of heat conduction as:

$$\frac{\partial T}{\partial t} = \alpha_x(x) \frac{\partial^2 T}{\partial x^2} + \alpha_y(y) \frac{\partial^2 T}{\partial y^2} + \alpha_z(z) \frac{\partial^2 T}{\partial z^2} \quad (5-7)$$

The thermal distribution in any position of a body can be calculated if given the structure of the body, its boundary condition and its initial states. The boundary condition in thermal conduction is a differential equation that describes the thermal conduction between the body with other materials. The initial states describe the temperature distribution at the time $t = 0$. The $\alpha_x, \alpha_y, \alpha_z$ are the thermal diffusivity at the x, y, z direction and the thermal diffusivity describes the ability to pass the temperature to its surroundings. The thermal diffusivity $\alpha(m^2/s)$ is already stated in previous section 3.1. which is

$$\alpha = \frac{k}{\rho c} \quad (5-8)$$

where $k(W/m \cdot k)$ is the thermal conductivity that describes the ability of heat energy transportation. The thermal conductivity k is also used to evaluate the depth of heat propagation in Eq 5-1 $d_{heat} = 2\sqrt{kt}$. The $\rho(kg/m^3)$ is the material density and $c(\frac{J}{kg} \cdot k)$ is the material's heat capacity which describes the amount of heat absorbed with a unit of temperature change. Currently only the numerical solution of Eq. (5-7) are provided using the finite element method (FEM). The analytical solution only exists in few ideal cases. The TSR is based on one of the ideal cases where an ideal heat pulse is evenly spread on the structure surface. The structure of the body is a semi-infinite solid plate. The analytical solution of this ideal situation is given as:

$$T(z, t) = \frac{Q_0}{\sqrt{t\pi\zeta}} e^{\left(-\frac{z^2}{4\alpha_z t}\right)} + T_a \quad (5-9)$$

where ζ is the thermal effusivity stated in chapter 5.2 which is the measurement of its ability to change the thermal energy with its surroundings. Q_0 is the total energy of the pulsed

excitation. T_a is the ambient temperature. As stated in the previously, the ambient temperature is eliminated by the background subtraction. The active thermal image sequences is subtracted with ‘inactive states’ which is the state without heating. Since the thermal camera only captures the thermal responses in the surface layer, The recorded thermal depth $z = 0$. Substituting these parameters into Eq. (5-9) gives:

$$\Delta T(t) = \frac{Q_0}{\sqrt{t\pi\zeta}} \quad (5-10)$$

Take the log in both left and right side gives

$$\log(\Delta T(t)) = \log\left(\frac{Q_0}{\sqrt{t\pi\zeta}}\right) \quad (5-11)$$

$$\log(\Delta T(t)) = \log(Q_0) + \frac{1}{2}\log(t) - \log(\sqrt{\pi} \cdot \zeta) \quad (5-12), \text{ (TSR thermal response)}$$

$$\log(t) = 2(\log(Q_0) - \log(\sqrt{\pi} \cdot \zeta) - \log(\Delta T(t))) \quad (5-13), \text{ (TSR time response)}$$

The thermal effusivity ζ is directly related to the crack characteristic. The Eq. (5-12) shows that the log time response is related to the input energy Q_0 , thermal effusivity ζ and the differential thermal response $\ln(\Delta T(t))$. Eq. (5-12) is the TSR thermal response. Classical TSR uses Eq. (5-12). In this work, the time images are used, and the TSR time response form in Eq. (5.13) is selected. In the Eq. (5-12) and Eq. (5-13), the TSR thermal-time response in the log-log space is a direct line in ideal situation with no defect. The slope of the line is $\frac{1}{2}$ as the output $\log(\Delta T(t))$ is the function of $\frac{1}{2}\log(t)$.

In the classical TSR, the TSR response is modelled as:

$$\log(\Delta T) \approx \beta_0 + \beta_1 \log(t) + \beta_2 \log(t)^2 + \dots + \beta_n \log(t)^n \quad (5-14)$$

where the $\Delta T = T - T_a$ is the differential temperature with the subtraction of the thermal frame without excitation. β_0 to β_n are the coefficients of the polynomial calculated with the curve fitting in the log-log space. In some situation only part of the thermal curve is used for the polynomial fitting. The selected time is called the time window and a good time window can significantly improve the signal to noise ratio (SNR) and the defect contract.

In this work, defects in different depth layers and the time delays are added to the classical TSR and only the first differential β_1 and constant β_0 are taken into consideration and gives the following equation:

$$\log(\Delta T) \approx \beta_0 + \beta_{11} \log(t - t_{11}) + \beta_{12} \log(t - t_{12}) + \dots + \beta_{1n} \log(t - t_{1n}) \quad (5-15)$$

The first differential coefficients with time delays $1 - \beta_{11}$ to $1 - \beta_{1n}$ are used for the reconstruction of different layer images with the layer depth of $2\sqrt{kl_1}$ to $2\sqrt{kl_n}$ respectively, k is the thermal diffusivity.

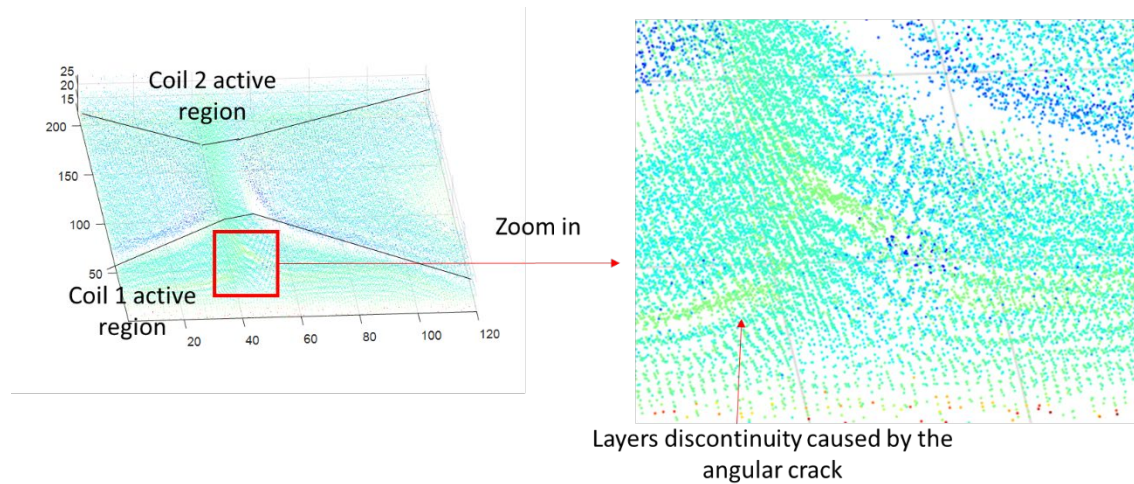


Figure 5-10 TSR based thermal tomographic reconstruction on artificial angular crack

The TSR based thermal tomographic reconstruction is shown in Figure 5-10. The angular crack is 3.5mm with inclination angle of 45° . The Helmholtz coil is used and placed at the top and bottom side of the specimen where the crack locates in the middle of the two coils. The excitation current is 300A with frequency of 260 kHz. For the purpose of comparison study, the experimental data is totally the same as it is in section 4.2 and section 5.2. The image above shows two active zone which is the coil 1 active region and coil 2 active region. The pixel intensity in these two area are generally uniform. The surface crack has an apparent higher intensity value than other area. The zoom in image in the right part of Figure 5-10 further shows the layer discontinuity caused by the surface and sub-surface crack. The reconstructed the angle direction from the surface towards material depth is also well shown.

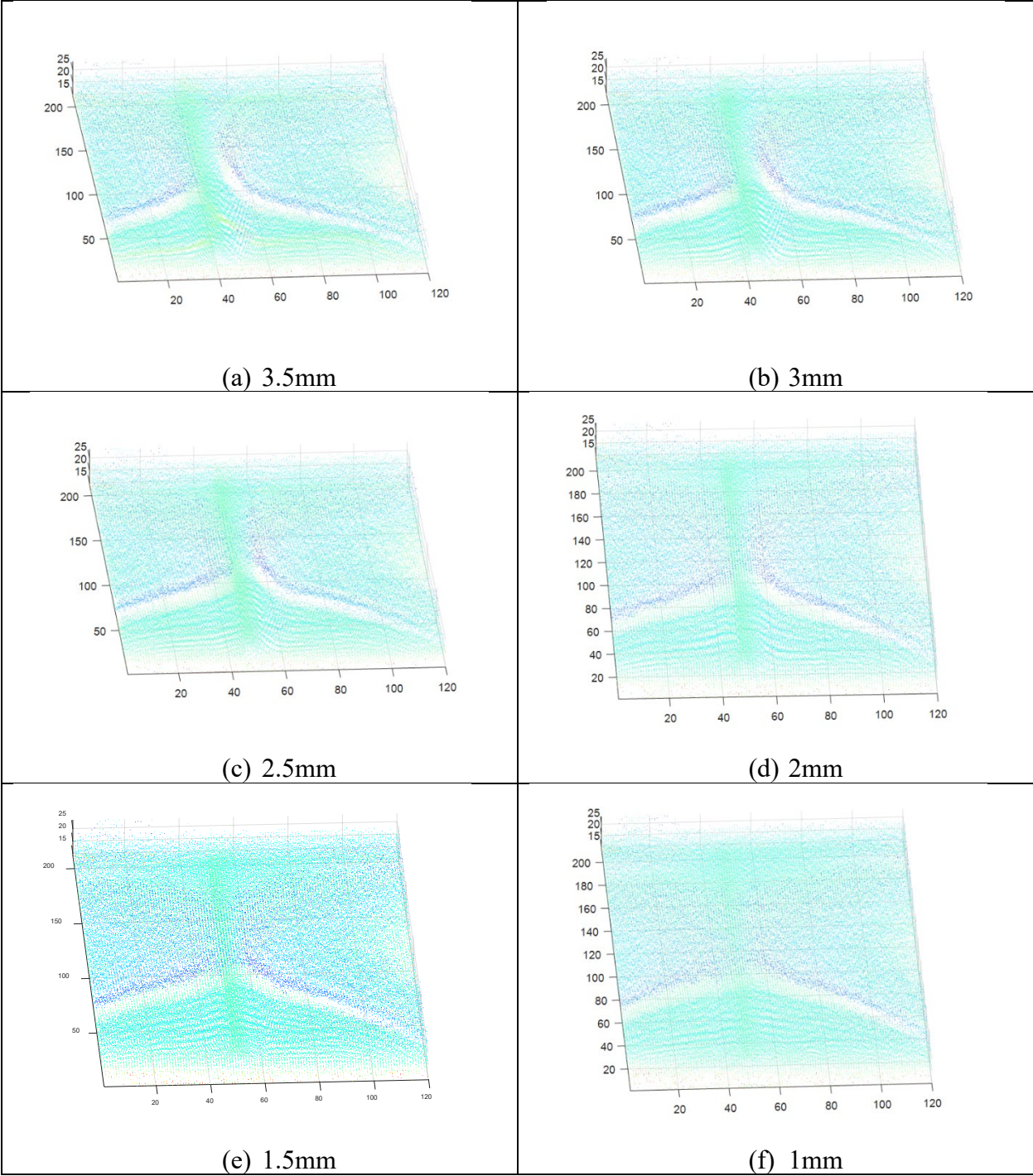


Figure 5-11 TSR based thermal tomography of angular cracks with different depths.

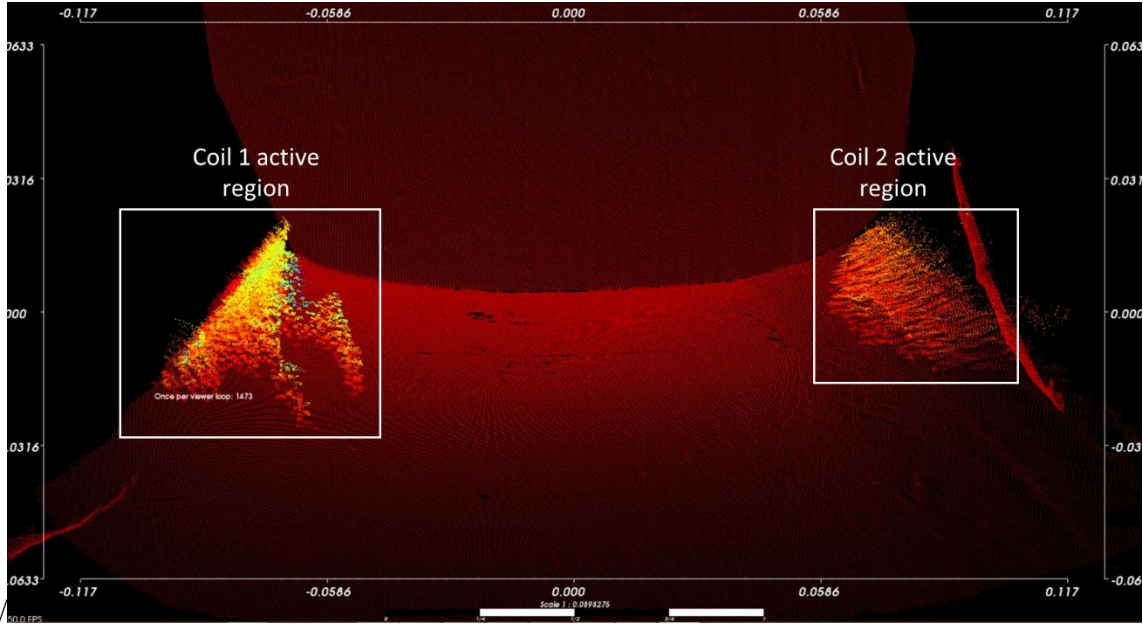


Figure 5-12 TSR based thermal tomography of rail track head with RCF crack (defect in left side)

Figure 5-11 shows the angular cracks of 45° with different depths from 3.5mm to 1mm reconstructed using TSR based thermal tomography. The crack position can be easily found either from the intensity or from the layers discontinuity. However, they have different physical meaning and principles. The intensity is related to the first differential TSR β_{1k} signal in the polynomial fitting where k is the k_{th} time layer which is related the depth in the tomography image. The strong intensity region is the position with low β values as $p(x, y, z) = 1 - \beta_{1k}$. In the TSR thermal response

$$\log(\Delta T(t)) = \log(Q_0) + \frac{1}{2} \log(t) - \log(\sqrt{\pi} \cdot \zeta) \approx \beta_0 + \beta_1 \log(t) + err \quad (5-16)$$

The evaluated $1 - \beta_{1k}$ is directive related to the thermal effusivity. A strong intensity region indicates a low thermal effusivity in the current time-spatial zone which may be caused by the cracks.

The layers continuity is linked to the TSR time response form in Equation. (5-13). The process of the slice layer reconstruction is the same as the DTSTD slice layer reconstruction illustrated in section 5.2. The DTSTD slice uses the time reaching each temperature layers to form the slice images. TSR layer uses the same principle as the DTSTD slice reconstruction. Recall

Equation. (5-13) which is $\log(t) = 2(\log(Q_0) - \log(\sqrt{\pi} \cdot \zeta) - \log(\Delta T(t)))$. In each temperature layer, the total energy $\log(Q_0)$ is a constant. The temperature $\log(\Delta T(t))$ is the same in each temperature layer. The thermal diffusivity has the linear relationship towards the time arrival which is visualized as the layer abruption if the defect exists. From the Figures 5-11. Image a shows the highest abruption in surface crack region with a 45° inclination slope from top left to bottom right. In Image f the layers are almost in the plane and the crack region has a slight hump which shows the heat flux is slightly blocked in this region.

Lastly, the Figure 5-12 shows the TSR reconstruction of the rail track with rolling contact fatigue (RCF). The RCF crack exists in the left part and right part is the non-crack part. The color intensity and layers continuity in the right part are uniform while the RCF cracks are clearly seen both via the color intensity and the layers abruption.

5.4 Comparison and summary

The classical heat conduction theory gives several analytical solution in simple geometry bodies with ideal cracks. Real case infrared thermography problems are usually solved with the finite element method with simulation software such as COMSOL. Currently there is no accurate analytical solution for the real infrared thermography problem. Either the DTSTD tomographic reconstruction or TSR based tomographic reconstruction are the estimation of the crack geometry. Thus multiple features character should be taken into consideration for the evaluation of the crack characteristics. In this chapter, the skewness feature, DTSTD tomographic reconstruction and the TSR tomographic reconstruction on a 3.5mm angular man-made crack are compared with a conclusion of the above three features.

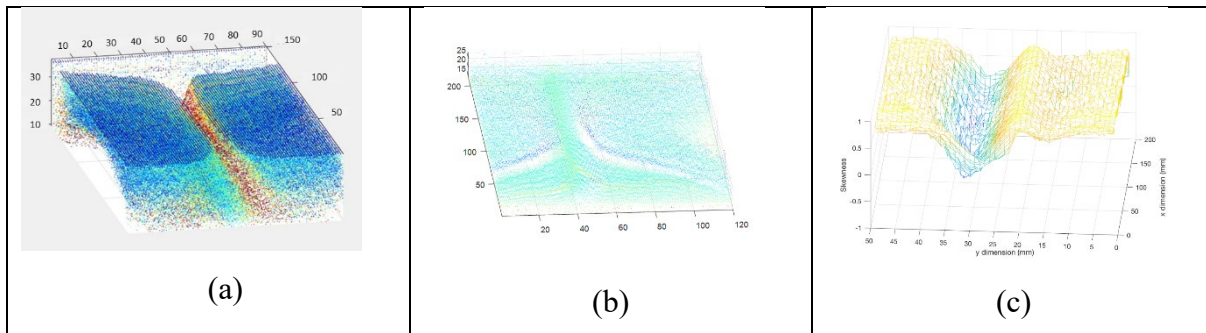


Figure 5-13 TSR based thermal tomography of rail track head with RCF crack (defect in left side) (a) DTSTD thermal tomographic reconstruction on 3.5 mm angular crack; (b) TSR thermal tomographic reconstruction on 3.5 mm angular crack; (c) Mesh plot of the skewness feature on 3.5 mm angular crack

Figure 5-13 shows the 3.5mm angular crack using thermal tomography reconstruction method of DTSTD, TSR based and the mesh plot of skewness feature respectively. It is clear that the DTSTD image and TSR image do not have a linear relationship in the reconstructed volume intensity. The DTSTD is more sensitive to the thermal discontinuity (context value) while TSR is more sensitive in the layer discontinuity and the excitation lift-off.

The TSR reconstruction is originated from an ideal solution of heat conduction. The uneven heating and the structure geometry needs to be seriously considered as the uneven heating causes the horizontal thermal propagation while the analytical model is based on the heat flux evenly spread on the sample surface. Also, the TSR time-delay format only uses the first differential coefficient for tomography extraction. The second and third differential is neglected in this study. It could also be seen that the time-delay is well visualized as the layer discontinuity of the crack region. The DTSTD is extracted from the original thermal response compared to the TSR signal which is constructed from log-log space. Thus the DTSTD signal has higher context contrast. The time layers is not obvious compared the TSR time-delay formatted reconstruction. Skewness feature can be treated as the deepest layer (or main defect layer) of the tomography image. The skewness uses the curvature information of entire thermal response. It is proofed as the statistical quantification of the defect severity and directive related to the depth of the defect. The skewness feature has very low computation cost with a relative robust depth estimation. Thus it can be used for quick and rough defect characterization and inspection.

	TSR thermal tomography	DTSTD thermal tomography	Skewness feature
Physical principle	Estimation of thermal effusivity using TSR first polynomial coefficient	Time delay caused by crack in different time slots	Statistical analysis of thermal response curvature information

Physical feature	First differential of the TSR polynomial in time delay format	Differential time sqrt of temperature drop	Skewness of modified thermal response
Mathematical model	$\log(\Delta T(t))$ $= \log(Q_0) + \frac{1}{2} \log(t)$ $-\log(\sqrt{\pi} \cdot \zeta)$ $\approx \beta_0 + \beta_1 \log(t)$ $+ err$	$R(u, v)_d$ $= \sqrt{T_{a\%^\circ C}}$ $-\sqrt{T_{b\%^\circ C}}$	$S(x, y)$ $= \frac{\frac{1}{n} \sum_{i=1}^n (x_i - \bar{x})^3}{\left(\sqrt{\frac{1}{n} \sum_{i=1}^n (x_i - \bar{x})^2} \right)^3}$
Volume intensity contrast	Low	High	N/A
Layers information	High	Low	One layer
Error and influence factor	Very sensitive to excitation power; sensitive to excitation lift off; very sensitive to testing object structure geometry	Sensitive to excitation power and excitation lift off; sensitive to object structure geometry	Very Robust to excitation power and lift off; less sensitive to object structure geometry
Robustness to excitation	Low	Medium	High
Computational complexity	Higher	High	Low

Table 7 Comparison table of TSR thermal tomography, DTSTD thermal tomography and the proposed skewness feature

Since these features are analysis from different physical angles, it is possible to merge these features in order to increase the signal to noise ratio (SNR) and decrease the errors and the influence factors such as the excitation lift-off and geometry of the structure.

However, there are two challenges in the feature fusion of these two tomography features. Firstly, they have different feature coordinates. Unlike the 2D features, the tomography feature have different depths. Merging the nearest points from DTSTD and TSR is a possible solution.

However, it lowers the resolution because of the merging of the nearest points. For example, it is likely that the TSR layer contrast is decreased if the DTSTD signal is merged in. Also, there is a higher computation complexity in finding the nearest neighbourhood. The second challenge lies in these two features have different characteristics. The DTSTD has higher volume contrast while the TSR has higher layer contrast. A proper balance needs to be found. Overall, a good 3D feature fusion algorithm should be studied that can increase the robustness and SNR.

6 CONCLUSION AND FUTURE WORK

This work established the first 3D ECPT system for the purpose of quantitative measurement and evaluation of the defect characteristics. The uncertainties in previous ECPT systems, such as the distance to the excitation, sample geometry shape and relative defect position in 3D space were solved with the temperature mapped to the 3D point cloud. To realize quick and reliable 3D temperature mapping, a feature based multi-spectrum image registration algorithm was introduced in section 3.1. For the quantitative evaluation of defect depth, in section 4.2, the skewness feature extraction was presented. To proceed with the study on depth evaluation, the thermal tomography work was presented in chapter 5. In this chapter, the conclusion and contribution are summarized in section 6.1, and the future works and potential research proposals are listed in section 6.2.

6.1 Conclusion and major contributions

In this thesis, a 3D ECPT system was built with a multi-spectrum registration algorithm. A fast 3D visualization platform was generated to support point cloud processing and defect quantification research. Various studies have been carried out on the 3D defect localization and quantification, including such approaches as PCA, point cloud segmentation and 3D defect enhancement. The conclusions and outcomes are listed in detail below.

6.1.1 Three-dimensional ECPT system set-up and camera registration.

In the first part, the thesis presented the procedure for building up the 3D ECPT system. The major issue involved projecting the thermal information to the point cloud or mapping each point cloud in the cloud to corresponding temperature information. Three dimensional thermography consists of a thermal camera and a 3D ranger. Two cameras record the two sources of information at the same time in different locations. To project the thermal temperature to the

point cloud, a projection matrix needs to be estimated. Currently, most works are based on checkerboard calibration. However, working conditions require an auto-registration method using common features without a checkerboard. Therefore, the projection matrix was estimated via the matched common features.

The procedure of matching features from the two modalities of the images consists of feature extraction, feature description and feature matching. Feature extraction extracts interest points from the two images. Feature description generates the feature descriptor vector that describes the features. Finally, feature matching is based on the feature descriptor vector that has the minimum vector distance. However, because of the two different modalities of the image, the existing feature descriptor cannot correctly describe the feature to be used for feature matching. This thesis proposed a new feature descriptor that would successfully match the features from a thermal image and visible image.

6.1.2 Three-dimensional scanning and visualization

Two 3D rangars were selected for the 3D profile rendering—the David 3D ranger and the Kinect structure light (SL) camera. The two 3D scanners have advantages and disadvantages, and they are used for different purposes. The Kinect camera has a very fast scanning speed of 30 frames per second. Thus, it is used for real-time 3D-thermal reconstruction and 3D profile rendering in motion. However the scanning quality is low in terms of both resolution and precision. Moreover, there are many holes within one scan. The low quality not only brings limited quantified information but also brings difficulties in the fusion of point cloud and thermal IR image. To address this issue, the Kinect fusion algorithm can be used, which uses the iterative closest point to merge several scans into one scan. In contrast, the David 3D ranger has a very precise scanning with a quality with the resolution up to 0.05 mm. However, in this study, it took around 2 minutes to complete one scan. The David 3D ranger is used for precise point cloud capturing, and it was the primary 3D scanner used in our lab for the experimental study.

Finally, a 3D visualization platform was built written in C++. The visualization platform can rotate the point cloud in three dimensions, and the temperature curve is auto-generated by

shift+left clicking the mouse. The 3D ECPT also enables precise thermal texture and visible texture alignment and fusion. The result was presented in chapter 3 with a comparison of the COMSOL simulation.

6.1.3 Defect detection and validation using 3D ECPT system

This section describes the studies on defect detection using the 3D ECPT system. The 3D ECPT system enables the quantified measurement and analysis of defect properties. Previous studies have used three levels of features for defect detection—the pixel level, local area level and pattern feature level. For pixel level features, the features are based on the single pixel transient thermal response, which does not show an advantage in 3D ECPT. This thesis proposed two new features—the 3D thermal gradient as a local area feature and skewness as a pattern-level feature. The two features were validated on artificial and natural cracks. The experimental study not only validated the two features for defect detection but also revealed that the two features are related to defect depth.

6.1.4 Thermal tomography reconstruction of natural and artificial cracks using 3D ECPT

This work proposed and investigated the first thermal tomographic approach using the 3D ECPT system. The thermal tomographic approach realizes a much higher standard in that it ‘slices’ the testing object into layers. Two thermal tomographic approaches, DTSTD thermal tomographic construction and TSR-based thermal tomographic reconstruction, were presented and compared in the thesis. These thermal tomographic approaches were also compared with X-ray tomography. The result showed the outlook of replacing X-ray tomography with thermal tomography, which is a totally non-invasive and much more convenient approach for obtaining object tomography structures. Furthermore, the result showed that thermal tomography has a unique advantage over X-ray tomography in terms of the potential for recognizing tiny cracks like RCF cracks, which are hardly to identify in X-ray tomography.

6.2 Future work

Based on the 3D ECPT system, several directions can be suggested in terms of the quantification of nondestructive testing.

6.2.1 Directional emissivity correction

Previously most research on the ECPT system was based on a flat testing sample. However, in recent years, research has increasingly focused on more general cases with non-flat structures such as wind turbines and railway tracks. The emissivity of an object is influenced by multiple parameters, such as the roughness of the material surface, the material type, the spectrum wave range of the camera and the angle between the camera and the testing object (directional emissivity). For a sample with a complex structure, directional emissivity has a strong influence on the measured radiation, and thus, it influences the measured temperature. With 3D thermography, the angles from the camera to each heat point on the testing sample can be calculated. The directional emissivity thus should be calculated and corrected.

6.2.2 Defect depth estimation based on the analysis of 3D heat flow

Previous studies have already shown that the transient thermal response of an ECPT system contains depth information of the defect. However, for the quantification of defects, many parameters need to be quantified during the experiment. The newly developed 3D ECPT system enables the quantification of the following components:

- a) The lift-off distance from the excitation coil and the testing sample. In the ECPT experiment, the different lift-offs to the excitation coil lead to an uneven-excited magnetic field and causes the uneven-heating.
- b) The geometry relationship of the cracks (the crack distance to other cracks and where in the testing sample the crack is located). The crack locations on the testing sample

sometimes give the different influences of the transient thermal responses. For example, a crack lying on the edge or corner of a testing sample has different thermal response characteristics compared with a crack lying on a flat area. In addition, multiple cracks behave differently compared with a single crack. The cracks influence each other in terms of transient thermal response when multiple cracks stand close to each other.

- c) Heat transfer in the cooling stage. In the cooling stage of the ECPT system, the thermal response is only related to the heat propagation, and the defect and non-defect areas will cause different thermal responses. In this study, with the quantified 3D heat flow, the 3D thermal gradient was calculated for defect pattern characterization.

6.2.3 Thermal tomographic reconstruction

This thesis represents the first attempt at thermal tomographic reconstruction using a 3D ECPT system. Two thermal tomographic reconstruction, the DTSTD and TSR-based tomography, were proposed and compared. These approaches involve estimations of defects' 3D shape based on different physical parameters and principles. More investigation should be conducted via a comparison study on X-ray CT and artificial cracks with different shapes and depths. In addition, more quantitative analysis, such as analysis of coil types, the influence of different lift-offs and other physical factors, should be conducted.

Based on the newly developed 3D ECPT system, future research work on the quantitative analysis of cracks characteristics is suggested that focuses on the three points mentioned above. In addition to feature-based 3D QNDE from transient responses, complementary approaches to tomography can be developed for further comparison and evaluation.

Reference:

- [1] A. Alahi, R. Ortiz, and P. Vandergheynst, "Freak: Fast retina keypoint," in Computer vision and pattern recognition (CVPR), 2012 IEEE conference on, 2012, pp. 510-517.
- [2] Y. He, G. Tian, M. Pan, and D. Chen, "Impact evaluation in carbon fiber reinforced plastic (CFRP) laminates using eddy current pulsed thermography," *Composite Structures*, vol. 109, pp. 1-7, 2014/03/01/ 2014.
- [3] L. Cheng and G. Y. Tian, "Surface crack detection for carbon fiber reinforced plastic (CFRP) materials using pulsed eddy current thermography," *IEEE Sensors Journal*, vol. 11, pp. 3261-3268, 2011.
- [4] J. Wilson, G. Tian, I. Mukriz, and D. Almond, "PEC thermography for imaging multiple cracks from rolling contact fatigue," *NDT & E International*, vol. 44, pp. 505-512, 2011.
- [5] M. R. Clark, D. M. McCann, and M. C. Forde, "Application of infrared thermography to the non-destructive testing of concrete and masonry bridges," *Ndt & E International*, vol. 36, pp. 265-275, 2003.
- [6] J. Kerr, Review of the effectiveness of infrared thermal imaging (thermography) for population screening and diagnostic testing of breast cancer: New Zealand Health Technology Assessment, Department of Public Health and General Practic, Christchurch School of Medicine and Health Sciences, 2004.
- [7] X. Maldague and S. Marinetti, "Pulse phase infrared thermography," *Journal of applied physics*, vol. 79, pp. 2694-2698, 1996.
- [8] S. M. Shepard, T. Ahmed, B. A. Rubadeux, D. Wang, and J. R. Lhota, "Synthetic processing of pulsed thermographic data for inspection of turbine components," *Insight*, vol. 43, pp. 587-589, 2001.
- [9] C. Ibarra Castanedo, "Quantitative subsurface defect evaluation by pulsed phase thermography: depth retrieval with the phase," 2005.
- [10] B. Oswald-Tranta, "Time and frequency behaviour in TSR and PPT evaluation for flash thermography," *Quantitative InfraRed Thermography Journal*, vol. 14, pp. 164-184, 2017.

- [11] M. A. Omar and Y. Zhou, "A quantitative review of three flash thermography processing routines," *Infrared Physics & Technology*, vol. 51, pp. 300-306, 2008.
- [12] E. G. Henneke, K. L. Reifsnider, and W. W. Stinchcomb, "Thermography—an NDI method for damage detection," *JOM*, vol. 31, pp. 11-15, 1979.
- [13] A. Gleiter, G. Riegert, T. Zweschper, and G. Busse, "Ultrasound lock-in thermography for advanced depth resolved defect selective imaging," *Insight-Non-Destructive Testing and Condition Monitoring*, vol. 49, p. 272, 2007.
- [14] K. L. Reifsnider, E. G. Henneke, and W. W. Stinchcomb, "The mechanics of vibrothermography," in *Mechanics of nondestructive testing*, ed: Springer, 1980, pp. 249-276.
- [15] R. B. Mignogna, R. E. Green Jr, J. C. Duke Jr, E. G. Henneke II, and K. L. Reifsnider, "Thermographic investigation of high-power ultrasonic heating in materials," *Ultrasonics*, vol. 19, pp. 159-163, 1981.
- [16] M. Z. Umar, V. Vavilov, H. Abdullah, and A. K. Ariffin, "Ultrasonic infrared thermography in non-destructive testing: A review," *Russian Journal of Nondestructive Testing*, vol. 52, pp. 212-219, 2016.
- [17] X. Han, Z. Zeng, W. Li, M. S. Islam, J. Lu, V. Loggins, et al., "Acoustic chaos for enhanced detectability of cracks by sonic infrared imaging," *Journal of applied physics*, vol. 95, pp. 3792-3797, 2004.
- [18] L. Maio, V. Memmolo, S. Boccardi, C. Meola, F. Ricci, N. D. Boffa, et al., "Ultrasonic and IR thermographic detection of a defect in a multilayered composite plate," *Procedia engineering*, vol. 167, pp. 71-79, 2016.
- [19] P. Myrach, "In-line Laser Thermography for Crack Detection: A Numerical Approach," 2015.
- [20] J. Qiu, C. Pei, H. Liu, Z. Chen, and K. Demachi, "Remote inspection of surface cracks in metallic structures with fiber-guided laser array spots thermography," *NDT & E International*, vol. 92, pp. 213-220, 2017.
- [21] J. Qiu, C. Pei, H. Liu, and Z. Chen, "Quantitative evaluation of surface crack depth with laser spot thermography," *International Journal of Fatigue*, vol. 101, pp. 80-85, 2017.

- [22] E. Kuhn, E. Valot, and P. Herve, "A comparison between thermosonics and thermography for delamination detection in polymer matrix laminates," *Composite Structures*, vol. 94, pp. 1155-1164, 2012.
- [23] M. Noethen, K.-J. Wolter, and N. Meyendorf, "Surface crack detection in ferritic and austenitic steel components using inductive heated thermography," in *Electronics Technology (ISSE), 2010 33rd International Spring Seminar on*, 2010, pp. 249-254.
- [24] T. Liang, W. Ren, G. Y. Tian, M. Elradi, and Y. Gao, "Low energy impact damage detection in CFRP using eddy current pulsed thermography," *Composite Structures*, vol. 143, pp. 352-361, 2016.
- [25] Y. He, M. Pan, and F. Luo, "Defect characterisation based on heat diffusion using induction thermography testing," *Review of scientific instruments*, vol. 83, p. 104702, 2012.
- [26] Li, Kongjing, et al. "State detection of bond wires in IGBT modules using eddy current pulsed thermography." *IEEE Transactions on Power Electronics* 29.9 (2013): 5000-5009.
- [27] Muzika, Lukáš, et al. "Application of flash-pulse thermography methods for quantitative thickness inspection of coatings made by different thermal spraying technologies." *Surface and Coatings Technology* 406 (2021): 126748.
- [28] Poelman, Gaétan, et al. "Adaptive spectral band integration in flash thermography: Enhanced defect detectability and quantification in composites." *Composites Part B: Engineering* 202 (2020): 108305.
- [29] Maierhofer, Christiane, et al. "Characterizing damage in CFRP structures using flash thermography in reflection and transmission configurations." *Composites Part B: Engineering* 57 (2014): 35-46.
- [30] Wu S, Gao B, Yang Y, et al. "Halogen optical referred pulse-compression thermography for defect detection of CFRP." *Infrared Physics & Technology*, 2019, 102: 103006.
- [31] Schlichting, Joachim, Ch Maierhofer, and Marc Kreutzbruck. "Crack sizing by laser excited thermography." *NDT & E International* 45.1 (2012): 133-140.
- [32] Cerniglia, Donatella, and Nicola Montinaro. "Defect detection in additively manufactured components: laser ultrasound and laser thermography comparison." *Procedia Structural Integrity* 8 (2018): 154-162.
- [33] He, Zhiyi, et al. "Joint scanning laser thermography defect detection method for carbon fiber reinforced polymer." *IEEE Sensors Journal* 20.1 (2019): 328-336.

- [34] Lu, Xiaolong, et al. "Pulsed Air-Flow Thermography for Natural Crack Detection and Evaluation." *IEEE Sensors Journal* 20.14 (2020): 8091-8097.
- [35] Lahiri, B B et al. "Medical applications of infrared thermography: A review. " *Infrared physics & technology* vol. 55,4 (2012): 221-235. doi:10.1016/j.infrared.2012.03.007
- [36] Tsoi, Kelly A., and Nik Rajic. "Non-destructive evaluation of aircraft structural components and composite materials at DSTO using sonic thermography. " *Defence Science and Technology Organisation Victoria (Australia) Air Vehicles Div*, 2011.
- [37] Montanini, R., and F. Freni. "Investigation of heat generation sources in sonic infrared thermography using laser Doppler vibrometry." *Proceedings of Quantitative Infrared Thermography QIRT* (2012).
- [38] Solodov, Igor, and Gerd Busse. "Resonance ultrasonic thermography: Highly efficient contact and air-coupled remote modes." *Applied Physics Letters* 102.6 (2013): 061905.
- [39] Yang, Bo, Yaoda Huang, and Long Cheng. "Defect detection and evaluation of ultrasonic infrared thermography for aerospace CFRP composites." *Infrared Physics & Technology* 60 (2013): 166-173.
- [40] Fierro, Gian Piero Malfense, et al. "Nonlinear ultrasonic stimulated thermography for damage assessment in isotropic fatigued structures." *Journal of Sound and Vibration* 404 (2017): 102-115.
- [41] Dong, Lihong, et al. "Effects of crack surface roughness on crack heat generation characteristics of ultrasonic infrared thermography." *Infrared Physics & Technology* 106 (2020): 103262.
- [42] Vrana, Johannes, et al. "Mechanisms and models for crack detection with induction thermography." *AIP conference Proceedings*. Vol. 975. No. 1. American Institute of Physics, 2008.
- [43] Netzelmann, Udo, and Günter Walle. "Induction thermography as a tool for reliable detection of surface defects in forged components." *17th World conference on nondestructive testing*. Vol. 8. 2008.
- [44] Wang, Fei, et al. "Blind image separation for the debonding defects recognition of the solid propellant rocket motor cladding layer using pulse thermography." *Measurement* 174 (2021): 108997.

- [45] Erazo-Aux, Jorge, et al. "Thermal imaging dataset from composite material academic samples inspected by pulsed thermography." *Data in brief* 32 (2020): 106313.
- [46] Guo, Xingwang, and Peiqi Jiang. "A differential temperature contour map to characterize the detection limit of pulsed thermography of materials." *Infrared Physics & Technology* 111 (2020): 103555.
- [47] Liu, Haochen, et al. "Detectability evaluation of attributes anomaly for electronic components using pulsed thermography." *Infrared Physics & Technology* 111 (2020): 103513.
- [48] Jena, Priyanka, and Rajesh Gupta. "Simultaneous estimation of multiple thermal properties using single-sided step heating thermography." *Infrared Physics & Technology* 115 (2021): 103726.
- [49] Daryabor, P., and M. S. Safizadeh. "Investigation of defect characteristics and heat transfer in step heating thermography of metal plates repaired with composite patches." *Infrared Physics & Technology* 76 (2016): 608-620.
- [50] Wang, Zijun, et al. "Comparative analysis of eddy current pulsed thermography and long pulse thermography for damage detection in metals and composites." *NDT & E International* 107 (2019): 102155.
- [51] Wang, Dong, et al. "Enhanced pre-processing of thermal data in long pulse thermography using the Levenberg-Marquardt algorithm." *Infrared Physics & Technology* 99 (2019): 158-166.
- [52] Ishizaki, T., and H. Nagano. "Measurement of 3D thermal diffusivity distribution with lock-in thermography and application for high thermal conductivity CFRPs." *Infrared Physics & Technology* 99 (2019): 248-256.
- [53] Ekanayake, Sarah, Sumit Gurram, and Robert H. Schmitt. "Depth determination of defects in CFRP-structures using lock-in thermography." *Composites Part B: Engineering* 147 (2018): 128-134.
- [54] Breitenstein, O., H. Straube, and K. Iwig. "Lock-in thermography with depth resolution on silicon solar cells." *Solar Energy Materials and Solar Cells* 185 (2018): 66-74.
- [55] E. Sousa, R. Vardasca, S. Teixeira, A. Seixas, J. Mendes, and A. Costa-Ferreira, "A review on the application of medical infrared thermal imaging in hands," *Infrared Physics & Technology*, vol. 85, pp. 315-323, 2017/09/01/ 2017.

- [56] A. Lozano and F. Hassanipour, "Infrared imaging for breast cancer detection: An objective review of foundational studies and its proper role in breast cancer screening," *Infrared Physics & Technology*, 2018/12/17/ 2018.
- [57] B. Yu, T. Qiao, H. Zhang, and G. Yan, "Dual band infrared detection method based on mid-infrared and long infrared vision for conveyor belts longitudinal tear," *Measurement*, vol. 120, pp. 140-149, 2018/05/01/ 2018.
- [58] A. Fernández-Caballero, J. C. Castillo, J. Martínez-Cantos, and R. Martínez-Tomás, "Optical flow or image subtraction in human detection from infrared camera on mobile robot," *Robotics and Autonomous Systems*, vol. 58, pp. 1273-1281, 2010/12/31/ 2010.
- [59] T. Li, C. Liu, Y. Liu, T. Wang, and D. Yang, "Binocular stereo vision calibration based on alternate adjustment algorithm," *Optik*, vol. 173, pp. 13-20, 2018/11/01/ 2018.
- [60] A. Valsaraj, A. Barik, P. V. Vishak, and K. M. Midhun, "Stereo Vision System Implemented on FPGA," *Procedia Technology*, vol. 24, pp. 1105-1112, 2016/01/01/ 2016.
- [61] X. Zhang, Y. Song, Y. Yang, and H. Pan, "Stereo vision based autonomous robot calibration," *Robotics and Autonomous Systems*, vol. 93, pp. 43-51, 2017/07/01/ 2017.
- [62] Y.-J. Lee and M.-W. Park, "3D tracking of multiple onsite workers based on stereo vision," *Automation in Construction*, vol. 98, pp. 146-159, 2019/02/01/ 2019.
- [63] K. Szelag, G. Maczkowski, R. Gierwialo, A. Gebarska, and R. Sitnik, "Robust geometric, phase and colour structured light projection system calibration," *Opto-Electronics Review*, vol. 25, pp. 326-336, 2017/12/01/ 2017.
- [64] I. Léandry, C. Brèque, and V. Valle, "Calibration of a structured-light projection system: Development to large dimension objects," *Optics and Lasers in Engineering*, vol. 50, pp. 373-379, 2012/03/01/ 2012.
- [65] W. Li, S. Fang, and S. Duan, "3D shape measurement based on structured light projection applying polynomial interpolation technique," *Optik*, vol. 124, pp. 20-27, 2013/01/01/ 2013.
- [66] M.-T. Le, L.-C. Chen, and C.-J. Lin, "Reconstruction of accurate 3-D surfaces with sharp edges using digital structured light projection and multi-dimensional image fusion," *Optics and Lasers in Engineering*, vol. 96, pp. 17-34, 2017/09/01/ 2017.

- [67] A. Asvadi, L. Garrote, C. Premebida, P. Peixoto, and U. J. Nunes, "Multimodal vehicle detection: fusing 3D-LIDAR and color camera data," *Pattern Recognition Letters*, vol. 115, pp. 20-29, 2018/11/01/ 2018.
- [68] Q. Wu, H. Yang, M. Wei, O. Remil, B. Wang, and J. Wang, "Automatic 3D reconstruction of electrical substation scene from LiDAR point cloud," *ISPRS Journal of Photogrammetry and Remote Sensing*, vol. 143, pp. 57-71, 2018/09/01/ 2018.
- [69] W. Luo and L. Li, "Automatic geometry measurement for curved ramps using inertial measurement unit and 3D LiDAR system," *Automation in Construction*, vol. 94, pp. 214-232, 2018/10/01/ 2018.
- [70] M. Pierzchała, P. Giguère, and R. Astrup, "Mapping forests using an unmanned ground vehicle with 3D LiDAR and graph-SLAM," *Computers and Electronics in Agriculture*, vol. 145, pp. 217-225, 2018/02/01/ 2018.
- [71] C. Jun, J. Y. Lee, B. H. Kim, and S. D. Noh, "Automatized modeling of a human engineering simulation using Kinect," *Robotics and Computer-Integrated Manufacturing*, vol. 55, pp. 259-264, 2019/02/01/ 2019.
- [72] C. Netramai, O. Melnychuk, C. Joochim, and H. Roth, "Combining PMD and stereo camera for motion estimation of a mobile robot," *IFAC Proceedings Volumes*, vol. 41, pp. 5417-5422, 2008.
- [73] O. Hall-Holt and S. Rusinkiewicz, "Stripe boundary codes for real-time structured-light range scanning of moving objects," in *Computer Vision, 2001. ICCV 2001. Proceedings. Eighth IEEE International Conference on*, 2001, pp. 359-366.
- [74] P. Fechteler, P. Eisert, and J. Rurainsky, "Fast and High Resolution 3D Face Scanning," in *ICIP (3)*, 2007, pp. 81-84.
- [75] Y. Lao, O. Ait-Aider, and H. Araujo, "Robustified Structure from Motion with rolling-shutter camera using straightness constraint," *Pattern Recognition Letters*, vol. 111, pp. 1-8, 2018/08/01/ 2018.
- [76] P. Gay, C. Rubino, M. Crocco, and A. Del Bue, "Factorization based structure from motion with object priors," *Computer Vision and Image Understanding*, vol. 172, pp. 124-137, 2018/07/01/ 2018.
- [77] J. H. Brito, "Autocalibration for Structure from Motion," *Computer Vision and Image Understanding*, vol. 157, pp. 240-254, 2017/04/01/ 2017.

- [78] L. Seitz, C. Haas, M. Noack, and S. Wieprecht, "From picture to porosity of river bed material using Structure-from-Motion with Multi-View-Stereo," *Geomorphology*, vol. 306, pp. 80-89, 2018/04/01/ 2018.
- [79] H. Sarbolandi, D. Lefloch, and A. Kolb, "Kinect range sensing: Structured-light versus Time-of-Flight Kinect," *Computer vision and image understanding*, vol. 139, pp. 1-20, 2015.
- [80] C. D. Mutto, P. Zanuttigh, and G. M. Cortelazzo, *Time-of-flight cameras and microsoft kinect (TM)*: Springer Publishing Company, Incorporated, 2012.
- [81] P. D. Pastuszak, A. Muc, and M. Barski, "Methods of infrared non-destructive techniques: review and experimental studies," in *Key Engineering Materials*, 2013, pp. 131-141.
- [82] B. Oswald-Tranta, "Thermoinductive investigations of magnetic materials for surface cracks," *Quantitative InfraRed Thermography Journal*, vol. 1, pp. 33-46, 2004.
- [83] L. Cheng, B. Gao, G. Y. Tian, W. L. Woo, and G. Berthiau, "Impact damage detection and identification using eddy current pulsed thermography through integration of PCA and ICA," *IEEE Sensors Journal*, vol. 14, pp. 1655-1663, 2014.
- [84] L. Bai, B. Gao, G. Y. Tian, W. L. Woo, and Y. Cheng, "Spatial and time patterns extraction of eddy current pulsed thermography using blind source separation," *IEEE Sensors Journal*, vol. 13, pp. 2094-2101, 2013.
- [85] Y. He, G. Tian, M. Pan, and D. Chen, "Eddy current pulsed phase thermography and feature extraction," *Applied Physics Letters*, vol. 103, p. 084104, 2013.
- [86] J. Liu, W. Ren, G. Y. Tian, B. Gao, J. S. Meng, and Y. Wang, "Early contact fatigue evaluation of gear using eddy current pulsed thermography," in *2014 IEEE Far East Forum on Nondestructive Evaluation/Testing*, 2014, pp. 208-212.
- [87] Z. Shi, X. Xu, J. Ma, D. Zhen, and H. Zhang, "Quantitative Detection of Cracks in Steel Using Eddy Current Pulsed Thermography," *Sensors*, vol. 18, p. 1070, 2018.
- [88] A. Yin, B. Gao, G. Yun Tian, W. L. Woo, and K. Li, "Physical interpretation and separation of eddy current pulsed thermography," *Journal of Applied Physics*, vol. 113, p. 064101, 2013.
- [89] G. Y. Tian, Y. Gao, K. Li, Y. Wang, B. Gao, and Y. He, "Eddy current pulsed thermography with different excitation configurations for metallic material and defect characterization," *Sensors*, vol. 16, p. 843, 2016.

- [90] B. Gao, L. Bai, W. L. Woo, and G. Tian, "Thermography pattern analysis and separation," *Applied Physics Letters*, vol. 104, p. 251902, 2014.
- [91] P. Peyre, P. Aubry, R. Fabbro, R. Neveu, and A. Longuet, "Analytical and numerical modelling of the direct metal deposition laser process," *Journal of Physics D: Applied Physics*, vol. 41, p. 025403, 2008.
- [92] T. Chady, R. Sikora, P. Lopato, G. Psuj, B. Szymanik, K. Balasubramaniam, et al., "Wind turbine blades inspection techniques," *Organ*, vol. 5, p. 16, 2016.
- [93] T. T. Wilheit, "A model for the microwave emissivity of the ocean's surface as a function of wind speed," *IEEE Transactions on Geoscience Electronics*, vol. 17, pp. 244-249, 1979.
- [94] X. P. Maldague, *Advances in signal processing for nondestructive evaluation of materials vol. 262*: Springer Science & Business Media, 2012.
- [95] P. Hellstein and M. Szvedo, "3D thermography in non-destructive testing of composite structures," *Measurement Science and Technology*, vol. 27, p. 124006, 2016.
- [96] S. Barone, A. Paoli, and A. V. Razionale, "A biomedical application combining visible and thermal 3D imaging," in *XVIII Congreso internacional de Ingenieria Grafica, Barcelona, 2006*, pp. 1-9.
- [97] I. Grubišić, "Medical 3D thermography system," *Periodicum biologorum*, vol. 113, pp. 401-406, 2011.
- [98] M. A. Akhloufi, Y. Guyon, C.-I. Castanedo, and A. Bendada, "Three-dimensional thermography for non-destructive testing and evaluation," *Quantitative InfraRed Thermography Journal*, vol. 14, pp. 79-106, 2017.
- [99] M. A. Akhloufi, Y. Guyon, A. Bendada, and C.-I. Castanedo, "Three-dimensional non-destructive testing (NDT) in the infrared spectrum," in *Thermosense: Thermal Infrared Applications XXXVII, 2015*, p. 948519.
- [100] M. A. Akhloufi and B. Verney, "Multimodal registration and fusion for 3d thermal imaging," *Mathematical Problems in Engineering*, vol. 2015, 2015.
- [101] S. Lagüela, J. Armesto, P. Arias, and J. Herráez, "Automation of thermographic 3D modelling through image fusion and image matching techniques," *Automation in Construction*, vol. 27, pp. 24-31, 2012.

- [102] C. Tang, G. Y. Tian, X. Chen, J. Wu, K. Li, and H. Meng, "Infrared and visible images registration with adaptable local-global feature integration for rail inspection," *Infrared Physics & Technology*, vol. 87, pp. 31-39, 2017.
- [103] Y. LeCun, Y. Bengio, and G. Hinton, "Deep learning," *nature*, vol. 521, p. 436, 2015.
- [104] Y. LeCun, B. E. Boser, J. S. Denker, D. Henderson, R. E. Howard, W. E. Hubbard, et al., "Handwritten digit recognition with a back-propagation network," in *Advances in neural information processing systems*, 1990, pp. 396-404.
- [105] A. Krizhevsky, I. Sutskever, and G. E. Hinton, "Imagenet classification with deep convolutional neural networks," in *Advances in neural information processing systems*, 2012, pp. 1097-1105.
- [106] Y. LeCun, L. Bottou, Y. Bengio, and P. Haffner, "Gradient-based learning applied to document recognition," *Proceedings of the IEEE*, vol. 86, pp. 2278-2324, 1998.
- [107] O. Russakovsky, J. Deng, H. Su, J. Krause, S. Satheesh, S. Ma, et al., "Imagenet large scale visual recognition challenge," *International Journal of Computer Vision*, vol. 115, pp. 211-252, 2015.
- [108] J. Deng, W. Dong, R. Socher, L.-J. Li, K. Li, and L. Fei-Fei, "Imagenet: A large-scale hierarchical image database," in *Computer Vision and Pattern Recognition, 2009. CVPR 2009. IEEE Conference on*, 2009, pp. 248-255.
- [109] S. Hoo-Chang, H. R. Roth, M. Gao, L. Lu, Z. Xu, I. Nogues, et al., "Deep convolutional neural networks for computer-aided detection: CNN architectures, dataset characteristics and transfer learning," *IEEE transactions on medical imaging*, vol. 35, p. 1285, 2016.
- [110] E. Gundogdu, A. Koç, and A. A. Alatan, "Object classification in infrared images using deep representations," in *Image Processing (ICIP), 2016 IEEE International Conference on*, 2016, pp. 1066-1070.
- [111] I. Rodger, B. Connor, and N. M. Robertson, "Classifying objects in LWIR imagery via CNNs," in *Electro-Optical and Infrared Systems: Technology and Applications XIII*, 2016, p. 99870H.
- [112] A. Esteva, B. Kuprel, R. A. Novoa, J. Ko, S. M. Swetter, H. M. Blau, et al., "Dermatologist-level classification of skin cancer with deep neural networks," *Nature*, vol. 542, p. 115, 2017.

- [113] K. Simonyan and A. Zisserman, "Very deep convolutional networks for large-scale image recognition," arXiv preprint arXiv:1409.1556, 2014.
- [114] Xu, C., Zhou, N., Xie, J., Gong, X., Chen, G. and Song, G., 2016. "Investigation on eddy current pulsed thermography to detect hidden cracks on corroded metal surface." *NDT & E International*, 84, pp.27-35.
- [115] Yi, Q., Tian, G.Y., Malekmohammadi, H., Zhu, J., Laureti, S. and Ricci, M., 2019. "New features for delamination depth evaluation in carbon fiber reinforced plastic materials using eddy current pulse-compression thermography." *NDT & E International*, 102, pp.264-273.
- [116] Zhu, P., Yin, C., Cheng, Y., Huang, X., Cao, J., Vong, C.M. and Wong, P.K., 2018. "An improved feature extraction algorithm for automatic defect identification based on eddy current pulsed thermography." *Mechanical Systems and Signal Processing*, 113, pp.5-21.
- [117] Geetha, G.K. and Mahapatra, D.R., 2019. "Modeling and simulation of vibro-thermography including nonlinear contact dynamics of ultrasonic actuator." *Ultrasonics*, 93, pp.81-92.
- [118] Guo, X. and Mao, Y., 2015. "Defect identification based on parameter estimation of histogram in ultrasonic IR thermography. *Mechanical Systems and Signal Processing*," 58, pp.218-227.
- [119] Duan, Y., Zhang, H., Maldague, X.P., Ibarra-Castanedo, C., Servais, P., Genest, M., Sfarra, S. and Meng, J., 2019. "Reliability assessment of pulsed thermography and ultrasonic testing for impact damage of CFRP panels. *NDT & E International*," 102, pp.77-83. .
- [120] Xie, J., Xu, C., Chen, G. and Huang, W., 2018. "Improving visibility of rear surface cracks during inductive thermography of metal plates using Autoencoder." *Infrared Physics & Technology*, 91, pp.233-242.
- [121] J. Peng, G. Y. Tian, L. Wang, Y. Zhang, K. Li, and X. Gao, "Investigation into eddy current pulsed thermography for rolling contact fatigue detection and characterization," *NDT & E International*, vol. 74, pp. 72-80, 2015.
- [122] X. Li, B. Gao, W. L. Woo, G. Y. Tian, X. Qiu, and L. Gu, "Quantitative surface crack evaluation based on eddy current pulsed thermography," *IEEE Sensors Journal*, vol. 17, pp. 412-421, 2017.

- [123] P. Li, Z. Q. Lang, L. Zhao, G. Tian, J. A. Neasham, J. Zhang, et al., "System identification-based frequency domain feature extraction for defect detection and characterization," *NDT & E International*, vol. 98, pp. 70-79, 2018.
- [124] C. Szegedy, V. Vanhoucke, S. Ioffe, J. Shlens, and Z. Wojna, "Rethinking the inception architecture for computer vision," in *Proceedings of the IEEE conference on computer vision and pattern recognition*, 2016, pp. 2818-2826.
- [125] H.J. Im, M. Gai, C. Wang, Y. Cho, Hybrid approach to visualize building energy information model in geospatial application programs, *Construction Research Congress 2012* (2012) 1262–1270.
- [126] D. Borrmann, A. Nüchter, M. Đakulović, I. Maurović, I. Petrović, D. Osmanković, et al., "The project thermalmapper–thermal 3d mapping of indoor environments for saving energy," *IFAC Proceedings Volumes*, vol. 45, pp. 31-38, 2012.
- [127] Lin, Dong, et al. "Fusion of thermal imagery with point clouds for building façade thermal attribute mapping." *ISPRS journal of photogrammetry and remote sensing* 151 (2019): 162-175.
- [128] M. I. Alba, L. Barazzetti, M. Scaioni, E. Rosina, and M. Previtali, "Mapping infrared data on terrestrial laser scanning 3D models of buildings," *Remote Sensing*, vol. 3, pp. 1847-1870, 2011.
- [129] L. Hoegner and U. Stilla, "Texture extraction for building models from IR sequences of urban areas," in *Urban Remote Sensing Joint Event*, 2007, 2007, pp. 1-6.
- [130] Chen, Xiaotian, G. Tian, J. Wu, C. Tang and K. Li, "Feature-Based Registration for 3D Eddy Current Pulsed Thermography," in *IEEE Sensors Journal*, vol. 19, no. 16, pp. 6998-7004, 15 Aug.15, 2019, doi: 10.1109/JSEN.2019.2911699.
- [131] R. Tsai, "A versatile camera calibration technique for high-accuracy 3D machine vision metrology using off-the-shelf TV cameras and lenses," *IEEE Journal on Robotics and Automation*, vol. 3, pp. 323-344, 1987.
- [132] R. Y. Tsai and R. K. Lenz, "A new technique for fully autonomous and efficient 3D robotics hand/eye calibration," *IEEE Transactions on robotics and automation*, vol. 5, pp. 345-358, 1989.

- [133] L.-L. Wang and W.-H. Tsai, "Camera calibration by vanishing lines for 3-D computer vision," *IEEE Transactions on Pattern Analysis & Machine Intelligence*, pp. 370-376, 1991.
- [134] Z. Zhang, "A flexible new technique for camera calibration," *IEEE Transactions on pattern analysis and machine intelligence*, vol. 22, 2000.
- [135] Z. Zhang, "Flexible camera calibration by viewing a plane from unknown orientations," in *Computer Vision, 1999. The Proceedings of the Seventh IEEE International Conference on, 1999*, pp. 666-673.
- [136] Z. Zhang, "Camera calibration with one-dimensional objects," *IEEE transactions on pattern analysis and machine intelligence*, vol. 26, pp. 892-899, 2004.
- [137] A. Geiger, F. Moosmann, Ö. Car, and B. Schuster, "Automatic camera and range sensor calibration using a single shot," in *Robotics and Automation (ICRA), 2012 IEEE International Conference on, 2012*, pp. 3936-3943.
- [138] R. Cucchiara, C. Grana, A. Prati, and R. Vezzani, "A Hough transform-based method for radial lens distortion correction," in *Image Analysis and Processing, 2003. Proceedings. 12th International Conference on, 2003*, pp. 182-187.
- [139] D. G. Lowe, "Distinctive image features from scale-invariant keypoints," *International journal of computer vision*, vol. 60, pp. 91-110, 2004.
- [140] D. G. Lowe, "Object recognition from local scale-invariant features," in *Computer vision, 1999. The proceedings of the seventh IEEE international conference on, 1999*, pp. 1150-1157.
- [141] H. Bay, T. Tuytelaars, and L. Van Gool, "Surf: Speeded up robust features," *Computer vision–ECCV 2006*, pp. 404-417, 2006.
- [142] S.-e.-A. Raza, V. Sanchez, G. Prince, J. P. Clarkson, and N. M. Rajpoot, "Registration of thermal and visible light images of diseased plants using silhouette extraction in the wavelet domain," *Pattern Recognition*, vol. 48, pp. 2119-2128, 7// 2015.
- [143] Y. Gu, K. Ren, P. Wang, and G. Gu, "Polynomial fitting-based shape matching algorithm for multi-sensors remote sensing images," *Infrared Physics & Technology*, vol. 76, pp. 386-392, 5// 2016.

- [144] Y. Li, J. Zou, J. Jing, H. Jin, and H. Yu, "Establish keypoint matches on multispectral images utilizing descriptor and global information over entire image," *Infrared Physics & Technology*, vol. 76, pp. 1-10, 5// 2016.
- [145] C. Aguilera, F. Barrera, F. Lumbreras, A. D. Sappa, and R. Toledo, "Multispectral image feature points," *Sensors*, vol. 12, pp. 12661-12672, 2012.
- [146] D. Gronau, "The spiral of Theodorus," *American Mathematical Monthly*, pp. 230-237, 2004.
- [147] W. Gautschi, "The spiral of Theodorus, numerical analysis, and special functions," *Journal of Computational and Applied Mathematics*, vol. 235, pp. 1042-1052, 2010.
- [148] Y. Wang, Y. Yang, and T. Chen, "Spectral-spatial adaptive and well-balanced flow-based anisotropic diffusion for multispectral image denoising," *J. Vis. Commun. Image Represent.*, vol. 43, pp. 185–197, Feb. 2017.
- [149] J. Canny, "A computational approach to edge detection," *IEEE Trans. Pattern Anal. Mach. Intell.*, vol. PAMI-8, no. 6, pp. 679–698, Nov. 1986.
- [150] M. A. Fischler and R. C. Bolles, "Random sample consensus: a paradigm for model fitting with applications to image analysis and automated cartography," *Communications of the ACM*, vol. 24, pp. 381-395, 1981.
- [151] A. Nguyen and B. Le, "3D point cloud segmentation: A survey," in *RAM*, 2013, pp. 225-230.
- [152] P. J. Besl and R. C. Jain, "Segmentation through variable-order surface fitting," *IEEE Transactions on Pattern Analysis and Machine Intelligence*, vol. 10, pp. 167-192, 1988.
- [153] J. M. Biosca and J. L. Lerma, "Unsupervised robust planar segmentation of terrestrial laser scanner point clouds based on fuzzy clustering methods," *ISPRS Journal of Photogrammetry and Remote Sensing*, vol. 63, pp. 84-98, 2008.
- [154] R. A. Johnson and D. W. Wichern, "Multivariate analysis," *Encyclopedia of Statistical Sciences*, vol. 8, 2004.
- [155] I. T. Jolliffe, "Principal component analysis," *Technometrics*, vol. 45, p. 276, 2003.
- [156] R. B. Rusu, "Semantic 3D object maps for everyday manipulation in human living environments," *KI-Künstliche Intelligenz*, vol. 24, pp. 345-348, 2010.
- [157] M. Pauly, R. Keiser, and M. Gross, "Multi - scale Feature Extraction on Point - Sampled Surfaces," in *Computer graphics forum*, 2003, pp. 281-289.

- [158] K. Pearson, "Contributions to the mathematical theory of evolution," *Philosophical Transactions of the Royal Society of London. A*, vol. 185, pp. 71-110, 1894.
- [159] R. A. Groeneveld and G. Meeden, "Measuring skewness and kurtosis," *The Statistician*, pp. 391-399, 1984.
- [160] J. C. W. Rayner, D. J. Best, and K. L. Mathews, "Interpreting the skewness coefficient," *Communications in statistics-theory and methods*, vol. 24, pp. 593-600, 1995.
- [161] B. C. Arnold and R. A. Groeneveld, "Measuring skewness with respect to the mode," *The American Statistician*, vol. 49, pp. 34-38, 1995.
- [163] J. Tabor, "Investigating the Investigative Task: Testing for Skewness: An Investigation of Different Test Statistics and Their Power to Detect Skewness," *Journal of Statistics Education*, vol. 18, 2010.
- [164] J. Zhu, G. Tian, Q. Min, and J. Wu, "Comparison Study of Different Features for Pocket Length Quantification of Angular Defects Using Eddy Current Pulsed Thermography." *IEEE Transactions on Instrumentation and Measurement*, 68 (5), pp. 1373-1381, 2019.
- [165] Q. Yi, etc., "Inverse reconstruction of fiber orientation in multi-layer CFRP using forward FEM and eddy current pulsed thermography, " submitted to *NDT and E International*, subject to minor revision.
- [166] Malcolm, Andrew A., Tong Liu, and Joseph J. Lifton. "Case studies in the use of computed tomography for non-destructive testing, inspection and measurement." *Singapore International NDT Conference and Exhibition*. 2013.
- [167] M. Daigle, D. Fratta, and L. B. Wang. "Ultrasonic and X-ray tomographic imaging of highly contrasting inclusions in concrete specimens." *Site Characterization and Modeling*, pp. 1-12, 2005.
- [168] Liu, X., Wang, H., Xu, M., Nie, S., & Lu, H. "A wavelet-based single-view reconstruction approach for cone beam x-ray luminescence tomography imaging.", *Biomedical optics express*, 5(11), pp. 3848-3858, 2014.
- [169] Liu, T., Rong, J., Gao, P., Liang, Z., Zhang, W., Zhang, Y., & Lu, H. "Cone-beam x-ray luminescence computed tomography reconstruction from single-view based on total variance." In *Medical Imaging: Physics of Medical Imaging*, Vol. 10573, p. 1057336, 2018.
- [170] H. D. Sarkissian, et al. "A cone-beam X-ray computed tomography data collection designed for machine learning." *Scientific data* 6(1), pp. 1-8, 2019

- [171] Gao, P., Rong, J., Pu, H., Liu, T., Zhang, W., Zhang, X., & Lu, H. "Sparse view cone beam X-ray luminescence tomography based on truncated singular value decomposition." *Optics express*, 26(18), pp. 23233-23250, 2018.
- [172] Scopigno, Roberto, Paolo Cignoni, Marco Callieri, Fabio Ganovelli, Gaetano Impoco, Paolo Pingi, and Federico Ponchio. "Using optically scanned 3D data in the restoration of Michelangelo's David." In *Optical metrology for arts and multimedia*, vol. 5146, pp. 44-53. International Society for Optics and Photonics, 2003.
- [173] Chen, Xiaotian, et al. "Investigation of Skewness Feature for Evaluation of Defects Using Eddy Current Pulsed Thermography." *IEEE Sensors Journal*, 19(24), pp. 12118-12125, 2019.
- [174] Chen, Xiaotian, G. Y. Tian, S. Ding, J. Ahmed and W. L. Woo, "Tomographic Reconstruction of Rolling Contact Fatigues in Rails using 3D Eddy Current Pulsed Thermography," in *IEEE Sensors Journal*, doi: 10.1109/JSEN.2021.3086307.
- [175] Holland, Stephen D. "Thermographic signal reconstruction for vibrothermography." *Infrared Physics & Technology* 54.6 (2011): 503-511.
- [176] Oswald-Tranta, Beata, and Steven M. Shepard. "Comparison of pulse phase and thermographic signal reconstruction processing methods." *Thermosense: Thermal Infrared Applications XXXV*. Vol. 8705. International Society for Optics and Photonics, 2013.
- [177] Benitez, Hernan, et al. "Defect quantification with thermographic signal reconstruction and artificial neural networks." *Proceedings of 8th Conference on Quantitative Infrared Thermography*, Padova, Italy. Vol. 2. 2006.
- [178] Almond, Darryl P., Stefano L. Angioni, and Simon G. Pickering. "Long pulse excitation thermographic non-destructive evaluation." *NDT & E International* 87 (2017): 7-14.

Appendix

A1. The binary file format of temperature profile.

This program saves the data analysis from Matlab and visualized via the visualization software developed by sensor group, Newcastle University.

The full Matlab coding is shown below:

```
fileID = fopen(Data.bin,'w');

% first number: number of Frames of temperature curve

fwrite(fileID,num1,'double');

% second number: number of Frames of RotatedCurve curve

fwrite(fileID,num,'double');

% thrid number: number of Point cloud points

fwrite(fileID,601601,'double');

%*****end of parameters*****

%first data block: Full Temperature Curve

fwrite(fileID,MappedTemperatureFlow','double');

%second data block: RotatedCurve Curveture

fwrite(fileID,Rotated_PointCloud','double');

%thrid data block: Skewness value

fwrite(fileID,Skewness,'double');
```